NASA CONTRACTOR REPORT

NASA CR-2611

PREDICTION OF ROTATING-BLADE VORTEX NOISE FROM NOISE OF NONROTATING BLADES

Martin R. Fink, Robert H. Schlinker, and Roy K. Amiet

Prepared by
UNITED TECHNOLOGIES RESEARCH CENTER
East Hartford, Conn. 06108
for Langley Research Center

NATIONAL AERONAUTICS AND SPACE ADMINISTRATION • WASHINGTON, D. C. • MARCH 1976

1. Report No.	2. Government Accession No.	3. Recipient's Catalog No.
NASA CR-2611		

4. Title and Subtitle	5. Report Date
Prediction of Rotating-Blade Vortex Noise From Noise of Nonrotating Blades	March 1976
	6. Performing Organization Code

7. Author(s)	8. Performing Organization Report No.
Martin R. Fink, Robert H. Schlinker, Roy K. Amiet	

9. Performing Organization Name and Address	10. Work Unit No.
United Technologies Research Center 400 Main Street East Hartford, Conn. 06108	760-63-02-04
	11. Contract or Grant No.
	NAS1-13372
	13. Type of Report and Period Covered
12. Sponsoring Agency Name and Address	Contractor Report
National Aeronautics & Space Administration Washington, DC 20546	14. Sponsoring Agency Code

15. Supplementary Notes

Final report.

16. Abstract

Measurements were conducted in an acoustic wind tunnel to determine vortex noise of nonrotating circular cylinders and NACA 0012 airfoils. Both constant-width and spanwise tapered models were tested at a low turbulence level. The constant-diameter cylinder and constant-chord airfoil also were tested in the turbulent wake generated by an upstream cylinder or airfoil.

Vortex noise radiation from nonrotating circular cylinders at Reynolds numbers matching those of the rotating-blade tests were found to be strongly dependent on surface conditions and Reynolds number. Vortex noise of rotating circular cylinder blades, operating with and without the shed wake blown downstream, could be predicted using data for nonrotating circular cylinders as functions of Reynolds number. Vortex noise of nonrotating airfoils was found to be trailing-edge noise at a time frequence equal to that predicted for maximum-amplitude Tollmein-Schlichting instability waves at the trailing edge. This noise weakens and disappears as Reynolds number is increased sufficiently to eliminate laminar boundary layers near the trailing edge.

17. Key Words (Suggested by Author(s))	18. Distribution Statement
Noise, Vortex Noise, Broad Band Noise, Nonrotating Airfoil	Unclassified - Unlimited Subject Category 71

19. Security Classif. (of this report)	20. Security Classif. (of this page)	21. No. of Pages	22. Price*
Unclassified	Unclassified	119	$4.25

*For sale by the National Technical Information Service, Springfield, Virginia 22161

CONTENTS

PREDICTION OF ROTATING-BLADE VORTEX NOISE FROM NOISE OF NONROTATING BLADES

Martin R. Fink, Robert H. Schlinker, and Roy K. Amiet

United Technologies Research Center

SUMMARY

Measurements were conducted in an acoustic wind tunnel to determine vortex noise of nonrotating circular cylinder and NACA 0012 airfoils. Both constant-width and spanwise tapered models were tested at a low turbulence level. The constant-diameter cylinder and constant-chord airfoil also were tested in the turbulent wake generated by an upstream cylinder or airfoil. Available theories, surface pressure spectrum measurements, and surface pressure cross-correlations were utilized to predict far-field noise for comparison with far-field acoustic measurements. These calculation methods were then utilized to predict sound spectra on the rotational axis of rotating blades with circular cylinder and with NACA 0012 airfoil sections. The predictions were compared with available NASA data.

Vortex noise radiation from nonrotating circular cylinders at Reynolds numbers matching those of the rotating-blade tests was found to be strongly dependent on surface condition and Reynolds number. Vortex noise of rotating circular cylinder blades, operating with and without the shed wakes blown downstream, could be predicted using data for nonrotating circular cylinders as functions of Reynolds number. Vortex noise of nonrotating airfoils was found to be trailing-edge noise at a tone frequency equal to that predicted for maximum-amplitude Tollmien-Schlichting instability waves at the trailing edge. Vortex noise from rotating airfoil-shaped blades with rounded tips behaved in this manner, but square-tip blades were louder and produced bluff-body vortex shedding noise. Noise from airfoil-shaped blades rotating in their shed wakes was dominated by incidence-fluctuation noise caused by discrete turbulent eddies.

INTRODUCTION

One of the important but poorly understood types of noise generated by propellers and helicopter rotors is vortex noise. This broadband noise can dominate measured spectra at moderate and high frequencies that have large contributions to perceived noise levels. Other noise processes for propellers and helicopter rotors include tone noise caused by blade thickness and

periodically varying lift, plus both tone and broadband noise from convected turbulence. Stationary turbulent eddies sliced by the rotating blades would generate tones, and fluctuations of eddy position cause broadband noise with a spectrum similar to an envelope of the tones.

Measurements had been obtained by NASA (refs. 1 and 2) of vortex noise generated by rotating blades. Microphones were placed upstream along the rotation axis where tone noise caused by blade thickness and steady lift forces should not occur. Steady lift was set equal to zero by testing (1) blades with circular cross-section, (2) untwisted blades with NACA 0012 airfoil section at zero pitch angle and zero axial velocity, and (3) helically twisted blades with NACA 0012 airfoil section at an advance ratio that produced zero relative incidence at all radial positions. These data for two vastly different blade cross-section shapes, each operated both with and without its shed wake blown downstream, can be used as test cases for evaluating vortex noise prediction methods.

Aeolian tones radiated by two-dimensional bluff bodies with uniform geometry and uniform upstream flow have long been associated with lift force fluctuations caused by Karman vortex shedding. The standard aeroacoustics analysis for such noise (refs. 3 and 4, and Section 3.5.1.2 of ref. 5) assumes that lift force fluctuation per unit span is concentrated at one Strouhal number and has constant amplitude along the span. It is assumed to have either constant phase (precisely coherent) or randomly varying phase along the span as represented by a correlation length. Intensity of far-field sound radiation is then proportional to velocity to the sixth power, rms lift coefficient squared, and either span squared (for coherent spanwise phase) or the product of span and correlation length. Correlation length is usually taken proportional to maximum thickness, so the randomly phased configuration is predicted to radiate sound with intensity proportional to frontal area.

Now consider a bluff configuration which has uniform upstream flow but spanwise taper of maximum thickness, or constant thickness but spanwise variation of relative velocity as produced by a shear flow. Modifications to the highly rigorous analysis developed in reference 5 to include such variations are given in Appendix A of this report. Experimentally, it was shown from near-wake studies given in reference 5 for tapered geometry and reference 7 for shear flows that each spanwise region sheds vortices at roughly the frequency expected for a two-dimensional flow with the same local conditions. Lift force fluctuation no longer has the same frequency at all spanwise positions. Acoustic radiation at a given frequency should depend not on the product of local correlation length and total span but on the product of local correlation length and that portion of the span for which significant force fluctuations occur at the selected frequency. Thus an additional length scale occurs for problems with spanwise nonuniformity.

This length may be proportional to correlation length or acoustic wavelength. It must approach the model span as nonuniformity becomes negligible and presumably approaches the correlation length as spanwise variations become large.

It is usually assumed that amplitude and spectrum shape of vortex noise from rotating blades could be computed from standard acoustic theory if values for local lift force fluctuation spectrum and correlation length were known at all radial positions. These quantities are evaluated for a constant-chord airfoil in uniform nonrotating flow at the same relative Mach number and Reynolds number. Previous analyses of overall acoustic intensity from rotating cylindrical rods (refs. 8 and 9) have regarded the rms lift coefficient and the ratio of phase correlation length to rod diameter as constant along the radius. When contributions of all segments to overall vortex noise were summed, the resulting sum of length scales was taken equal to the rotational radius. However, spectrum shape cannot be predicted until a method for estimating this length is developed. Some analyses have assumed that the phase is precisely coherent along each segment which radiates at a given frequency. Correlation length is then taken to be the length of such a segment. Two unevaluated assumptions are made within this analysis. Quantities evaluated for spatially uniform geometry and flow are assumed to apply for a nonrotating but spanwise varying flow or geometry, and quantities associated with vortex shedding in a rotating flow are assumed equal to those for nonrotating flow. Neither of these assumptions had been examined by actual comparisons with data. The rotating-blade vortex noise data of references 1 and 2 provided a good starting place for such a study. Acoustic radiation data and surface correlation lengths for constant-chord and tapered-chord nonrotating blades tested in a uniform flow would also be needed. Such data could be obtained in an acoustic wind tunnel and utilized to check the assumptions in going from a constant to a spanwise-varying expected vortex tone frequency. The analysis which predicts acoustic radiation for spanwise-varying geometry in a uniform flow could then be utilized to predict vortex spectra for untapered rotating blades, for comparison with the data of references 1 and 2.

SYMBOLS

Values are given in both SI and U.S. Customary Units. The measurements were made in U.S. Customary Units.

A	Proportionality constant, m^{-2} (ft^{-2})
b	Cylinder or airfoil model span, m (ft)
B	Number of rotor blades
c	Airfoil chord, m (ft)
c_o	Speed of sound, m/sec (ft/sec)
D	Cylinder diameter, m (ft)
E	Spectral density of mean square velocity fluctuation, m^2/sec (ft^2/sec)
f	Frequency, Hz
f,g	Sharply peaked and broadly peaked arbitrary functions of frequency
F,G	Fourier transforms of frequency functions
I	Acoustic intensity, Watts/m^2 (lb/ft^4sec)
k	Wave number, $2\pi/\lambda$, m^{-1} (ft^{-1})
K	Root mean square lift coefficient per unit span
ℓ	Phase correlation length, m (ft)
L	Lift per unit span, N/m (lb/ft)
ℓ_y	Lift force correlation length, m (ft)
M	Mach number, V/c_o
n	Arbitrary integer
p	Static pressure, N/m^2 (lb/ft^2)

p_{ref}	Reference pressure for sound and surface pressure levels, $2 \times 10^{-5} N/m^2$ (4.18×10^{-7} lb/ft^2)
p_∞	Free stream static pressure, N/m^2 (lb/ft^2)
p_{ff}	Far field acoustic pressure, N/m^2 (lb/ft^2)
p_{max}	Maximum fluctuating pressure at airfoil trailing edge, N/m^2 (lb/ft^2)
p_S	Fluctuating pressure on airfoil surface, N/m^2 (lb/ft^2)
p_{te}	Fluctuating pressure on airfoil trailing edge, N/m^2 (lb/ft^2)
q	Dynamic pressure, $(\frac{1}{2})\rho V^2$, N/m^2 (lb/ft^2)
r	Radial distance, m (ft)
R	Far-field distance, m (ft)
R_{LL}	Autocorrelation of lift force spectrum
R_{pp}	Autocorrelation of far-field acoustic pressure spectrum
S_E	Amplitude of effective Sears function for lift force in turbulence
S_{LL}	Power spectral density of lift force, $N^2 sec^2$ (lb^{2}sec^2)
S_{pp}	Power spectral density of far-field acoustic pressure, $N^2 sec^2/m^2$ (lb^{2}sec^2/ft^2)
S_{QQ}	Maximum power spectral density of pressure on airfoil trailing edge, $N^2 sec^2/m^2$ (lb^{2}sec^2/ft^2)
St	Strouhal number, fD/V
t	Time, sec
$\overline{v^2}$	Mean square transverse velocity fluctuation, m^2/sec^2 (ft^2/sec^2)
V	Free stream velocity, m/sec (ft/sec)
V_t	Tip rotational velocity, $\Omega D/2$, m/sec (ft/sec)
V_θ	Velocity component in angular direction, m/sec (ft/sec)

x	Chordwise distance, m (ft)
y	Spanwise distance, m (ft)
α	Angle of attack, deg, also arbitrary constant
β	Angular reduced frequency, rad/sec
Γ	Circulation, m^2/sec (ft^2/sec)
δ^*	Laminar boundary layer displacement thickness, m (ft)
Δf	Frequency bandwidth, Hz
Δp	Cylinder surface static pressure fluctuation, N/m^2 (lb/ft^2)
$\zeta_{1, 2, 3}$	Rectangular coordinates downstream, upward, and spanwise, m (ft)
θ	Direction angle from upstream, deg
λ	Acoustic wavelength, c_o/f, m (ft)
Λ	Turbulence integral scale length, m (ft)
ν	Kinematic viscosity, m^2/sec (ft^2/sec)
ξ	Spanwise distance, m (ft)
ρ	Density, N sec^2/m^4 (lb sec^2/ft^4)
τ	Time delay, sec
φ	Sideline angle, sec, also velocity potential function m^2/sec (ft^2/sec)
Φ	Phase angle, rad
ω	Angular frequency, rad/sec
ω_o	Normalizing angular frequency, rad/sec
Ω	Blade rotation angular frequency, rad/sec

APPARATUS AND PROCEDURE

Acoustic Research Tunnel

The UTRC acoustic wind tunnel permits the concurrent measurement of both near- and far-field aerodynamic noise and the unsteady static pressures on surfaces of airfoil models. A detailed description of this tunnel was given in reference 10. The acoustic research tunnel, shown in figure 1, is of the open-circuit open-test-section type. Use of an open circuit and a muffling section with two right-angle bends and parallel baffles downstream of the diffuser greatly reduces the contribution of the tunnel fan to the test section ambient noise level. The free-jet test section has a two-stage nozzle that provides nominal maximum velocities of 120 m/sec (400 fps) and 205 m/sec (670 fps) at flow cross section areas of 0.93 and 0.42 sq m (10 and 4.5 sq ft), respectively. For these tests the smaller cross section area, 0.79 m (31 in.) wide and 0.53 m (21 in.) high, was used with a 2.75 m (9 ft) open jet length. In this position the nozzle was rotated 90° from its usual position, so that larger model spans could be installed. The inlet contraction ratio was 16.5 for this nozzle. By locating the free jet within a 5.5 m (18 ft) long, 4.9 m (16 ft) high, and 6.7 m (22 ft) wide anechoic chamber, reflection-free conditions are obtained above the 250 Hz free-field cutoff frequency (99% absorption at normal incidence) determined by the acoustic wedge dimensions. The chamber has been found to be anechoic within a 200 Hz to 20,000 Hz range of calibration frequencies for broadband noise. Measurements can be taken in the acoustic far-field within the chamber but outside the high-velocity airstream.

The upstream inlet section is equipped with five removable screens and a large length-to-diameter honeycomb section. These provide controlled turbulence levels with a minimum value less than 0.2% in the test section. Grids and turbulence-generating airfoils can be inserted at the junction of the two nozzle contractions to provide a range of turbulence levels and wake profiles. The test section airflow is brought into the diffuser by a collector that has anechoic treatment on its flow-impingement lip. Triangular tabs are attached to the nozzle exit to produce a spatially nonuniform shear layer. This nonuniformity prevents generation of feedback tones caused by impingement of the shear layer against the collector lip at moderate and high subsonic speeds. The test section collector and three-stage diffuser have been designed to avoid local flow separation. The 1500 hp electric induction motor and the acoustically lined muffling sections upstream of the centrifugal fan were selected to reduce noise radiated from the tunnel drive system.

Nonrotating Blade Models

Two circular cross section and three airfoil models were used in this investigation. All of these models had 78.7 cm (31 in.) span plus a rectangular portion of 6.35 cm (2.50 in.) span at each end that protruded through tunnel sidewalls and was bolted to a massive support frame. These models are sketched in figure 2. One circular cross-section model had 5.08 cm (2.00 in.) constant diameter and the other had linear 2:1 taper from 5.08 cm (2.00 in.) to 2.54 cm (1.00 in.) diameter. This 1.85° included angle cone frustum was intended to provide a doubling of expected vortex shedding frequency along the span in uniform flow. Data for this configuration were expected to simulate the spanwise variation of vortex shedding frequency along the outer half of the 1.525 m (5.0 ft) rotational radius of the constant-diameter rotating rod.

The three airfoil models, shown in figures 2 and 3, all had NACA 0012 airfoil sections in streamwise planes. One had constant 11.43 cm (4.50 in.) chord, another had linear 2:1 taper from 15.24 cm (6.00 in.) to 7.62 cm (3.00 in.) chord, and the third had linear 4:1 taper from 18.29 cm (7.20 in.) to 4.51 cm (1.80 in.) chord. The 50% chord lines were normal to the flow and were located 35.5 cm (14.0 in.) downstream of the nozzle exit plane. These models were intended to provide different spanwise gradients of expected vortex tone frequency, for comparison with vortex tone spectra for rotating constant-chord blades with NACA 0012 airfoil sections.

In addition to these airfoil models, three simple wake-generating models were used. These had 1.07 m (42 in.) span and were installed at the junction of the two nozzle stages, 1.89 m (48 in.) upstream of the nozzle exit plane. One model was a 5.08 cm (2.00 in.) diameter cylinder and another was an 11.4 cm (4.5 in.) chord NACA 0012 airfoil. Because the wake generated by this airfoil was relatively weak at the downstream airfoil location, a 44.5% thickness ratio airfoil with the same chord as the airfoil and the same maximum thickness as the cylinder was utilized instead. This airfoil was built by adding a sheet-metal fairing to a circular cylinder and did not have a standard airfoil section.

Instrumentation

Far-field acoustic spectra were measured with microphones located at five positions on an arc of 2.25 m (7.38 ft) radius in a vertical plane at midspan. The center of this arc was at midchord of the models. Microphones were placed at 50°, 70°, 90°, 110°, and 130° angular position relative to the upstream flow diameter. These commercially available 0.635 cm (1/4 in.) diameter condenser microphones were at grazing incidence and were used without

a protecting grid. Frequency response of these microphones is flat from 6 Hz to 20,000 Hz. Free-field directivity correction at grazing incidence of the microphone diaphragm is less than 0.2 dB at frequencies to 16,000 Hz and the signal is about 0.5 dB too large at 20,000 Hz without the protecting grid. Atmospheric attenuation of the far-field acoustic signals was calculated as increasing from about 0.1 dB at 10,000 Hz to about 0.4 dB at 20,000 Hz. Because this correction is approximately equal in magnitude and opposite in direction to that for free-field directivity of the microphones, corrections were not applied to the measured data. All far-field microphones and surface pressure transducers were calibrated daily with a 250 Hz pistonphone.

Surface pressure spectra were measured with two types of pressure transducers. One type consisted of a commercially-available pressure-sensitive semiconductor and integrated-circuit Wheatstone bridge, attached to a thin metal foil. These gages were 0.076 cm (0.030 in.) thick, had an active area with 0.22 cm (0.085 in.) diameter, and were cemented to the surface of the NACA 0012 airfoil models. A photograph of six gages mounted near the trailing edge of the constant-chord NACA 0012 airfoil is presented as figure 4. Wires from these gages were cemented along the airfoil trailing edge and brought out through holes in circular endplates flush with the sidewalls. The airfoil model shown in figure 3 has been pitched to a large incidence angle to provide a better view of the surface pressure gages. The triangular tabs on the nozzle upper and lower lips, needed to avoid edge tones, also are clearly visible.

These thin gages had been attached with a relatively weak cement so that they could be moved to other spanwise positions and other models without damaging the semiconductor active element. Some of these gages detached from the circular cylinder model at high test airspeeds, apparently because the airfoil lifted the forward edge of the bent metal foil. A 0.09 cm (0.035 in.) deep and 0.635 cm (0.25 in.) wide groove was therefore milled along the span of the constant-diameter cylinder and the tapered cylinder, centered at 135° from upstream, to contain another type of surface pressure transducer. These semiconductor integrated-circuit gages were mounted in a recessed steel baseplate 0.635 cm (0.25 in.) wide, 1.40 cm (0.55 in.) long, and 0.09 cm (0.035 in.) deep with the gage active surface flush with the baseplate upper surface. These gages could be cemented in place with a strong non-air-drying cement. Unoccupied portions of the slot were filled with putty. The steel baseplate could be pried away from the cement without damage to the gage, allowing the gages to be moved to different spanwise locations.

Test Conditions and Procedures

Tests conducted with each model and no upstream wake generator generally comprised initial runs at airspeeds from about 30 m/sec (100 ft/sec) to 180 m/sec (590 ft/sec), using the 90° far-field microphone to determine trends of noise radiation. For all data, a 100 Hz high-pass filter was utilized to remove tunnel fan drive noise at frequencies below the liner anechoic frequency. Narrowband spectra were measured on-line and velocity was varied in 3 to 6 m/sec (10 to 20 ft/sec) increments. The resulting measured variation of far-field OASPL with velocity was examined to choose velocities at which detailed investigations should be obtained. At those velocities, far-field spectra were measured on-line at all five microphone positions at both constant and 1/3 octave bandwidths. In some cases, the constant narrow bandwidth was varied so that tone amplitudes could be determined in the presence of narrowband-random peaks. Surface pressure transducers were then attached to the model. Far-field spectra were obtained on-line for the 90° microphone. If they matched those obtained without surface gages and wires, surface pressure spectra and surface-to-surface cross-correlation were obtained on-line. If not, new far-field data were also taken.

In preliminary tests conducted with the airfoils at zero incidence, tone noise was found to increase and then decrease into the tunnel background noise at relatively low velocities. This result had been expected from the tests described in reference 11 in which noise data were presented for NACA 0012 and 0018 airfoil models of larger chord. Tone noise was shown to be associated with the presence of a laminar boundary layer over nearly the entire chord of at least one side of an airfoil. At zero incidence, the NACA 0012 airfoil has an adverse pressure gradient downstream of 15% chord. Increasing the test velocity and therefore the test Reynolds number causes boundary layer transition in the region of adverse pressure gradient. Therefore the airfoil models also were tested at 4° incidence where minimum pressure is moved back to 30% chord on the pressure surface and the adverse pressure gradient remains mild to 50% chord. Tests at this incidence were conducted to velocities near 120 m/sec (400 ft/sec). The constant-chord airfoil in the wake of an upstream airfoil was tested at 15 m/sec (50 ft/sec) velocity increments to 137 m/sec (450 ft/sec) and narrowband spectra of 6.4 Hz bandwidth from 0 to 2000 Hz were taken on-line.

Noise generated in the open-jet test section is refracted as it passes through the shear layer on its way to the far-field microphones. The required correction to measured far-field amplitude and direction angle is a function of Mach number, measurement direction, and distance of the sound source from the shear layer. A derivation of the correction method had been presented in reference 12. Data measured at 90° direction have generally not been

corrected because the calculated change in amplitude is less than 0.2 dB. Cited directivity comparisons have been conducted at low velocities at which this correction is negligible. Tones radiated through the shear layer would be expected to be scattered through a range of frequency proportional to the ratio of turbulent eddy size to acoustic wavelength. This effect is believed to be unimportant for the tone frequencies and bandwidths studied in these tests.

Hot-wire surveys were taken at the center of the test section with the wake-generating cylinder and wake-generating airfoil located upstream. Streamwise rms turbulence levels in the cylinder wake were about 3.9%, 3.6%, and 3.2% at 40, 63, and 100 m/sec (131, 206, and 328 ft/sec) velocities. These levels are approximately given by the empirical equation $0.08\ U^{-1/5}$ where U is the velocity in meter per second. A decrease of intensity with velocity to the inverse 1/5 power was previously found in measurements of grid-generated turbulence within this wind tunnel. Turbulence spectra contained a weak spike at a Strouhal number of 0.2 referenced to cylinder diameters and axial velocity at the upstream cylinder location. This was superimposed on a spectrum which decayed smoothly in the manner expected for isotropic turbulence. The streamwise integral scale length at all velocities was about 4.5 cm (1.8 in.) which is about 0.9 diameters. In contrast, axial spacing between vortices of a Karman vortex street would be about 4 diameters. Wake properties at the test distance considerably downstream of the wake-generating cylinder were therefore typical of conventional turbulence rather than of a near-wake Karman vortex street.

During initial measurements with an 11.4 cm (4.5 in.) chord NACA 0012 airfoil located upstream, the wake was found to be only about 3 cm (1.2 in.) thick and to have maximum streamwise rms turbulence intensities near 0.4%. The resulting expected noise caused by incidence fluctuation was calculated to be less than the test section background noise. Therefore a 44.5% thickness ratio airfoil with the same 11.4 cm chord as that of the constant-chord airfoil and the same 5 cm diameter as that of the constant-diameter cylinder was tested. Measured rms streamwise turbulence levels in the wake of this airfoil were 4.8%, 4.2%, and 2.7% at 40, 63, and 100 m/sec (131, 206, and 328 ft/sec) velocities. These turbulence levels can be approximated by the empirical equation $0.30\ U^{-1/2}$ where U is the velocity in meters per second. The turbulence levels decayed more rapidly with increasing velocity than those for the cylinder wake but were generally about the same amplitude. Spectra contained a weaker spike than was measured for the cylinder wakes, at the same frequency. Streamwise integral scale lengths were about 4.1 cm (1.6 in.) or about 10% less than for the cylinder. These turbulence levels, and the ratio of turbulence scale length to airfoil chord, were believed large enough to produce measurable noise when convected past the downstream airfoil.

DISCUSSION OF NONROTATING BLADE DATA

Circular Cross Section Models

Available information. - Numerous experimental studies have been conducted of fluctuating forces on constant-diameter circular cylinders in uniform flow. A summary of these results for subcritical Reynolds numbers and discussion of their application to predicting noise from aircraft landing gear was given in pp 24-28 of reference 13. It was noted that the wake flow contains periodic disturbances of a Karman vortex sheet at subcritical Reynolds numbers between roughly 10^3 and 10^5 but becomes aperiodic at larger Reynolds numbers. A region of Reynolds number near 10^6 produces no dominant frequency within the wake (ref. 14) but periodic structure is established at larger Reynolds numbers. Current nomenclature describes the region of Reynolds numbers between roughly 5×10^4 and 5×10^5 as the lower critical regime. As the boundary layer separation point oscillates forward and aft during the vortex shedding process, the boundary layer entering the wake is laminar during part of the cycle and turbulent in the remainder. Mean drag coefficient, rms lift coefficient, and correlation length decrease with increasing Reynolds number in this regime. A transcritical or plateau regime occurs when the Reynolds number has become sufficiently large so that the cylinder boundary layer transition point is upstream of the separation point's most forward excursion. Aerodynamic coefficients are minimum in this region. This is followed by an upper critical regime and finally by the supercritical regime where aerodynamic coefficients are constant at levels somewhat larger than those of the plateau.

Variations of measured rms lift coefficient and correlation length in the lower critical and transcritical regimes are given in figures 5 and 6 for the data of references 15-21 for low-turbulence incident flow. A summary of measured rms lift coefficient data for smooth cylinders with low-turbulence upstream flow is given in figure 5. Regions representing the scatter of repeated measurements at constant Reynolds number are shown for references 15, 16, 17, and 20. Contrary to the data of reference 19, rms lift coefficient appears to decrease from approximately constant values near 0.5 at Reynolds numbers less than 4×10^4 to values between 0.05 and 0.15 at Reynolds numbers near 4×10^5. This region also exhibits a rapid decrease of mean drag coefficient with increasing Reynolds number. Power spectral densities of surface pressure (refs. 17 and 18) and lift force at Reynolds numbers from 2×10^5 to 4×10^5 (refs. 15 and 17) were sharply peaked at the critical Strouhal number near 0.2. Increasing the Reynolds number to the plateau region near 6×10^5 and the upper critical region near 1×10^6 caused the lift force spectra (ref. 17) to be relatively flat below the critical Strouhal number, to decay less rapidly with increasing Strouhal number from roughly

0.2 to 0.4, and to have a second peak at a Strouhal number of about 0.45 to 0.5. Further increase to supercritical Reynolds numbers restored the sharp peak at a Strouhal number near 0.2, although considerable intensity remained below that Strouhal number. The important result is that for Reynolds numbers from 1.85×10^5 to 4.15×10^5 corresponding to blade tip conditions for the cylinder blades of reference 1, rms lift coefficient along the blade decreased with increasing Reynolds number and the lift force spectrum remained sharply peaked at the critical Strouhal number. The lift coefficient behavior is shown in figure 5 to be approximated by constant values of 0.5 at subcritical Reynolds numbers to 3×10^4, 0.1 at plateau Reynolds numbers above 3×10^5, and exponential decay (a straight line on semilogarithmic graphs) between them.

Free-stream turbulence had been found (ref. 18) to reduce the rms lift coefficient at Reynolds numbers near 1×10^5 but to cause no reduction at 2.4×10^5. Using those data, three straight-line segments shown as dash lines in figure 5 were arbitrarily assumed for the variation of rms lift coefficient with Reynolds number for a cylinder in the turbulent wake of an upstream cylinder. Below a Reynolds number of 3×10^5, the amount by which rms lift coefficient exceeded 0.1 was arbitrarily halved from its value in smooth flow.

Measured ratios of spanwise correlation length to cylinder diameter are given in figure 6 for smooth cylinders with smooth upstream flow. Some of these data were obtained from surface pressure measurements at different spanwise positions (refs. 17 and 18) and others from spanwise traverses of hot wires in the near wakes (refs. 20 and 21). Correlation length decreased from about 4.5 diameters in subcritical flow to less than one diameter in the plateau regime and then increased to about one diameter at supercritical Reynolds numbers. As with the rms lift coefficient, this variation was arbitrarily approximated for later calculations by straight-line segments on semilogarithmic paper. Turbulent flow with a scale length much smaller than the diameter was shown in reference 18 to decrease the correlation length, and arbitrary straight-line segments were assumed as before for turbulent flow.

Acoustic energy radiated by fluctuating lift forces on a circular cylinder is proportional to the product of velocity to the sixth power, rms lift coefficient squared, and correlation length to the first power. Note that an increase of velocity that increased the Reynolds number from 3×10^4 to 3×10^5 at constant geometry would produce a 60 dB increase of acoustic energy from the velocity dependence but roughly a 20 dB decrease from the dependence on lift coefficient and correlation length. Thus the expected behavior of dipole sound radiation in this Reynolds number range could follow an apparent fourth power velocity dependence. Turbulence would be expected to reduce the sound radiation, with largest reductions at low Reynolds numbers.

Far-field acoustic measurements. - Strong tone-like peaks were observed to dominate over the broadband noise levels in the far field spectra by 10 to 20 dB. This is illustrated in figure 7 for the constant-diameter cylinder. These typical narrowband spectra, covering a range of velocities, were measured at 90° to the flow without an upstream turbulence generator.

Visually, the spectral peaks in each figure suggest a pure tone generating mechanism with unity bandwidth. However, this concept required verification to insure that the measured sound pressure levels were independent of the analysis bandwidth. A simple test, in which various bandwidths were selected to analyze the same spectra, showed that sound pressure level increased as analysis bandwidth was increased. Eventually a constant amplitude was reached, indicating that the analyzer bandwidth had become larger than the tone bandwidth. These results showed that the peaks were not pure tones but rather were narrowband-random with approximately a 22 Hz bandwidth. Qualitatively, this fact can be appreciated by comparing the data with the spectrum of an electronically generated pure tone at the same measurement bandwidth. As figure 7 shows, the tone-like peaks were broader than the pure tone. Based on these results, all measured levels were corrected by 10 log 22 to account for the finite tone bandwidth. Note that the spectra in figure 7 have already been corrected.

While testing the models with circular cross sections, it became evident that surface roughness was an important parameter influencing the far field narrowband spectra. Figure 8 illustrates the situation for the 2:1 tapered cylinder at 79 m/sec (260 ft/sec) (3×10^5 Reynolds number based on the maximum diameter) before and after machining the transducer groove. The transducer groove, located at 135° from the forward stagnation point, had been carefully filled with wax to produce a smooth contour. Despite extensive efforts to obtain a smooth surface, the surface roughness at this position was sufficient to alter the spectra. This is evident in the fact that altogether different tones dominated the two spectra. To further check this phenomenon the tapered cylinder was rotated to locate the groove at the rear stagnation point. Again the spectra changed, although the new spectrum more closely simulated the original clean-cylinder spectrum. These observations verified that the spanwise variation of the vortex shedding mechanism was sensitive to surface roughness in the Reynolds number regime investigated here.

The importance of surface roughness was dramatically demonstrated for the tapered cylinder on an extremely cold and humid day during this winter test program. After starting the tunnel, a test point from the previous day was selected for a check of data repeatability. Initially this provided good agreement with the previous day's results. When the spectrum for this velocity was analyzed somewhat later, the dominant tone had changed. As figure 9 shows, the far-field spectra at 90° to the flow continued to change

as time progressed. The tunnel was shutdown and an inspection of the cylinder showed that frost had formed on the cylinder surface. The time-dependent surface roughness had thus altered the far-field narrowband spectra. Based on these results, care was exercised to ensure that frost formation did not occur during testing.

There exists one study in the literature which substantiates the influence of surface roughness on vortex shedding. Using flow visualization, reference 17 showed that the separation point on a constant-diameter cylinder moved forward when surface roughness was applied. This occurred at Reynolds numbers from 2.6×10^5 to 6.5×10^6 with a surface roughness to cylinder diameter ratio as small as 0.025. The result suggests that transition to turbulence in the wake will occur sooner thereby changing the spanwise coherence of the vortex structure. This would, in turn, alter the spanwise coherence of fluctuating pressure on the cylinder surface which radiates acoustically to the far field.

The above examples stress the importance of surface roughness on the vortex shedding mechanism and the far-field acoustic spectra. Where applicable, this phenomenon will be emphasized in the following discussion of the data.

The constant-diameter cylinder was tested with low upstream turbulence flow and in the turbulent wake of an upstream cylinder. For the low turbulence condition the far field acoustic spectra displayed tone-like peaks at velocities below 46 m/sec (150 ft/sec). This is illustrated by the typical narrowband spectrum in figure 7, measured at 90° to the flow direction and 2.25 m (7.38 ft) above the center of the model. The data were obtained prior to machining the transducer groove in the cylinder surface. It should be noted that the amplitudes in figure 7 have been corrected for the finite tone bandwidth using the procedure discussed earlier.

As the velocity was increased to 50 m/sec (164 ft/sec) the tone bandwidth broadened and the amplitude decreased as shown in figure 7. Amplitudes strengthened again with a small increase of velocity as indicated by the 61 m/sec (200 ft/sec) spectrum. However, as velocity was increased above 67 m/sec (220 ft/sec) the tone sound pressure level decreased rapidly as indicated by the 81 m/sec (265 ft/sec) spectrum. Additional increases in velocity yielded spectra such as shown for 98 m/sec (320 ft/sec) in which the tone peak began to merge with the tunnel background noise level. However, when velocity was increased from 149 m/sec (490 ft/sec) to 155 m/sec (510 ft/sec) the sound pressure level abruptly increased by 40 dB. At these velocities the measured amplitudes were close to those predicted using a sixth-power velocity extrapolation from the low-velocity data.

The above described trends of the dominant tone sound pressure level are shown in figure 10 as a function of velocity. As before, the data have been corrected for the finite tone bandwidth. Variations of the overall sound pressure level (OASPL) measured between 200 Hz and 5,000 Hz are also given.

When the upstream turbulence generator was mounted within the tunnel nozzle, streamwise turbulence levels of about 3.9% and streamwise integral length scales of 0.89 diameters were measured at the test section location. These measurements were conducted with hot wires over the velocity range of 40 to 100 m/sec (131 to 328 ft/sec). Radiated noise from the constant-diameter cylinder located in the turbulent wake was approximately 15 dB lower in amplitude than that for the low-turbulence upstream flow condition, as shown in figure 10. Also, the previously observed tone-like peaks in the spectrum broadened consideraly. It should be noted that the amplitudes plotted in figure 10 have been corrected for the analyzer bandwidth rather than the narrowband-random tone bandwidth. This follows since the peaks now represent a broadband source mechanism. As the velocity increased beyond 100 m/sec (328 ft/sec) the far-field noise decreased into the tunnel background noise. However, the abrupt increase in sound pressure previously observed near 150 m/sec (500 ft/sec) occurred again.

The 2:1 tapered cylinder, when compared to the constant diameter cylinder, produced a number of tone-like peaks in the far-field acoustic spectra. As shown in figure 11, at 159 m/sec (520 ft/sec) the spectrum for this velocity contained six distinct narrowband-random peaks. Details of the frequency behavior will be discussed shortly. The measurements were made prior to machining the transducer groove using the same experimental setup as in the constant-diameter cylinder test. Amplitudes of the strongest far-field peak and the OASPL are plotted in figure 12 for the tapered cylinder over a range of velocities. Sound pressure levels have been corrected for the finite tone bandwidth. Strength of the dominant tone and OASPL varied roughly as velocity to the sixth power, as shown by the straight lines in figure 12.

Several interpretations of the far-field sound pressure levels can now be given. In the case of the constant-diameter cylinder without the upstream turbulence generator, the tone sound pressure level increased and decreased over the velocity range investigated rather than progressively increasing. This is explained in view of the results in references 13 and 14. These show that for a cylinder there exists a Reynolds number range 10^3 to 10^5 over which periodic wake disturbances occur followed by a Reynolds number regime near 10^6 which produces no vortex shedding. At even larger Reynolds numbers, the periodic wake structure is again established.

The present cylinder data span the Reynolds number range from 1×10^5 to 6.5×10^5. It is possible that the initial increases in tone sound pressure level over the range 1×10^5 to 2×10^5 occurred in the subcritical region in which vortex shedding is known to exist. In contrast, the region 2.5×10^5 to 5.5×10^5, in which the sound pressure level decreased by as much as 20 dB, might then correspond to the regime in which vortex shedding becomes nonexistent. Finally, the sudden increase in sound pressure level above Reynolds number 5.5×10^5 would correspond to the return of periodic structure in the wake. Admittedly, the various transition Reynolds numbers are lower than those suggested by references 13 and 14. However, there is presently insufficient data to indicate the effects of surface roughness on transition Reynolds number so that the above arguments may describe the situation correctly.

For the case of the 2:1 tapered cylinder several comments can be made. Due to its tapered geometry, the local diameter at any spanwise position is less than that of the constant-diameter cylinder. Thus all but one end of the tapered cylinder would reach the critical transition Reynolds numbers discussed earlier at higher velocities than observed for the constant-diameter cylinder. This suggests that the tone sound pressure level for the tapered cylinder should display transition similar to those observed for the constant-diameter cylinder but at higher velocities. Possibly this explains the absence of any sudden transition in the tone amplitudes plotted in figure 12. Recall that the constant-diameter cylinder displayed several such transitions, as shown in figure 10.

Figure 13 shows the variation of the far-field dominant tone frequency with velocity for the constant-diameter cylinder. The upstream turbulence generator was not installed. Over the velocity range of 30 to 50 m/sec (98 to 164 ft/sec) the frequency dependence was described by a Strouhal number of 0.18. Beyond this the Strouhal number increased slowly until it reached 0.20 at 76 m/sec (250 ft/sec). This Strouhal number range is indicated by the two straight lines in figure 13. Finally, when the velocity was increased from 80 m/sec (250 ft/sec) to 85 m/sec (278 ft/sec) an abrupt shift occurred in the dominant tone frequency. It should be noted that the frequency jump from 240 Hz to 400 Hz occurred near the transition velocity (or transition Reynolds number) at which the tone amplitude in figure 10 began to decrease and merge with the tunnel background noise. Beyond 100 m/sec (328 ft/sec) the frequency dependence was approximated by a Strouhal number of 0.20.

For the 2:1 tapered cylinder, the variation of tone frequency as a function of velocity is shown in figure 14. The strongest peak is represented by a solid symbol and the second strongest by a tailed symbol. The results indicate that the dominant tone frequency did not increase uniformly with

increasing velocity. Instead, the dominant frequency depended on which of three velocity regimes was being tested. For test velocities in the low range below 54 m/sec (210 ft/sec) or in the high range above 130 m/sec (430 ft/sec), the tone-like peak at the lowest frequency dominated and amplitude of successive peaks decreased as frequency increased. Only two to three distinct peaks occurred in the low velocity range. The lowest frequency corresponded to a Strouhal number near 0.18 referenced to maximum diameter. The highest frequency was somewhat less than would be given by that Strouhal number and the minimum diameter. The middle frequency was approximately their geometric mean. Within the intermediate velocity range of 54 to 113 m/sec (210 to 370 ft/sec) the peak at the next highest frequency dominated the frequency spacing became irregular and the number of peaks increased. At the highest velocity there were six peaks, spread between a Strouhal number of 0.20 referenced to the maximum and minimum diameters.

Surface pressure measurements. - For surface transducers mounted on the constant-diameter cylinder at 135° from the forward stagnation point, narrow-band spectra of the transducer outputs showed strong tone-like peaks. The frequencies of the tones coincided with those of the dominant tones observed in concurrently obtained far-field spectra. Figure 15 shows the amplitude of the surface pressure fluctuations at the tone frequencies as a function of spanwise position for various velocities. The zero spanwise location is referenced with respect to the center of the test section and model as illustrated by the small insert in each figure. The frequency of each tone is also shown in the figure. It should be noted that the far-field spectra were altered by the increased surface roughness due to the presence of the transducer and the wax filled groove. This resulted in a change of the dominant tone frequency on the cylinder surface and in the far-field when compared to the observed frequency for the clean cylinder in figure 13. In addition, measured sound pressure levels in the far field differed from the clean cylinder data as indicated in figure 10. For this reason, the prediction of the far field levels based on the surface measurements will be compared to the measured far field amplitudes in the presence of the transducer groove. It is felt that the surface pressure amplitudes are accurate to within ±1 dB, this being the estimated scatter in calibrating the surface transducers.

The data for the constant-diameter cylinder at 31 m/sec (101 ft/sec) displayed approximately a constant surface pressure level in the spanwise direction. At 40 m/sec (131 ft/sec) and 63 m/sec (206 ft/sec) the level decreased at stations close to the tunnel sideplates. Finally, the amplitudes measured at 76 m/sec (250 ft/sec) were scattered and fail to show any trend. This is attributed to the vortex shedding structure being essentially non-existent over the velocity range of 76 to 140 m/sec (250 to 459 ft/sec).

Figure 16 shows the surface pressure level as a function of spanwise position on the 2:1 tapered cylinder for various velocities. Again, the transducers were mounted at 135° from the forward stagnation point and the zero spanwise station is represented by the insert. Far-field narrowband spectra obtained simultaneously indicated that the change in surface roughness due to the transducer and wax-filled groove caused a change in acoustic spectrum when compared to the previous clean-cylinder far-field data, as shown in figure 8. However, the frequency of the surface tones coincided with the new far-field dominant tones. This should be kept in mind since, as with the constant-diameter cylinder, predictions of far-field levels are based on surface pressure measurements and compared to concurrently measured far-field spectra.

The data in figure 16 shows a decrease in surface pressure level in the direction of the large diameter end. This follows if the local Strouhal number is approximately constant, so that increasing the local cylinder diameter would decrease the vortex shedding frequencies. Thus a given tone amplitude will disappear as one proceeds from the small-diameter end at which the frequency of interest was generated.

The velocity dependence of the tone surface pressure level on the tapered cylinder at a fixed spanwise station is shown in figure 17. For positions close to the tone generation region at the small-diameter end, the levels displayed a fourth power velocity dependence as expected for constant force coefficients. At more distant stations this velocity dependence no longer held since the tone essentially disappeared and the transducer now measured the boundary layer pressure fluctuations.

In the case of the constant-diameter cylinder located in the wake of the upstream turbulence generator, the tone surface pressure level varied with spanwise position as shown in figure 18. The levels were within the range of 120 dB $\pm$5 dB. The small change over the range of velocities suggests that the surface pressure levels were dominated by the turbulence wake properties of the upstream generator. Notice that the dominant tone frequency has been altered by the turbulent wake flow.

In the present study, filtered surface pressure correlation measurements were made using transducers mounted on the constant-diameter and 2:1 tapered cylinder. The purpose of the measurements was to determine surface correlation lengths of the vortex shedding tones in the spanwise direction. These lengths in addition to the surface tone pressure levels are needed to predict the far field sound pressure levels.

Figure 19 shows the filtered surface cross correlation coefficient for the constant-diameter cylinder at various velocities with low upstream turbulence flow. The plotted data represent the coefficient at zero delay

time between the various transducers. Note that the spanwise transducer separation is illustrated by the small insert on each figure. The tone frequency passed by the bandpass filters is also given. A Gaussian and exponential decay curve have been included to permit analytically modeling the correlation length. Knowledge of this is required to calculate the far field spectra. Gaussian decay had been assumed in the analyses developed in references 3 and 5 but exponential decay had been observed experimentally (ref. 17).

The one-sided correlation length ℓ_y was obtained by numerically integrating the area under the curves in figure 19. The resulting values normalized by the cylinder diameter are indicated on each figure.

Surface pressure correlation measurements were also carried out for the 2:1 tapered cylinder as shown in figure 20 for a range of velocities. In this study the transducers were moved as a group across the span of the cylinder. Thus the two separate curves in each figure represent the filtered correlation coefficient obtained from each configuration. A correlation value equal to unity identifies the reference transducer station. Note that the right-hand side of the two decay curves agree providing confidence in the experimental technique. For example, in figure 20(a) the shape of the dashed curve over the spanwise range 1.5 to 4.5 matches the decay of the solid line curve between 4.5 and 8. Similar comparisons can be made at each of the other velocities. The tone frequency investigated in each case is also shown.

One interesting observation was the existence of phase shifts across the span. These appear as negative values in the cross correlation coefficients at the zero delay time. This was accounted for in evaluating the correlation length by integrating numerically the area under the solid-line decay curve. Note that the result represents the two-sided correlation length and for that reason is represented by $2\ell_y$ normalized by the maximum cylinder diameter.

Measurements of the surface pressure correlations were also made with the constant-diameter cylinder in the wake of the upstream turbulence generator. The results are shown in figure 21 for several velocities. The one-sided integral length scales were obtained using the previously discussed approach. The tone frequency and correlation length are shown in each case. One important result is that the correlation lengths were smaller than those for the constant-diameter cylinder without the upstream generator. It is inferred that the turbulent wake destroys the spanwise coherence of the vortex shedding thereby reducing ℓ_y.

Constant chord. - Typical narrowband spectra measured in the far field at 90° to the flow for the constant-chord airfoil at -4° angle of attack, without an upstream turbulence generator, are shown in figure 22 for 37, 52, and 64 m/sec (120, 170, and 210 ft/sec) velocities. The measurement bandwidth for each spectrum is noted in each figure. At the lowest of these velocities there was one clearly dominant peak, a second peak roughly 10 dB weaker, and a third peak roughly 10 dB weaker than the second. Frequencies of these peaks were several hundred Hz apart. This type of narrowband spectrum had been previously observed (ref. 11) in tests of a constant-chord airfoil having a span to chord ratio of 2.33 as compared with the 6.89 ratio for this test. As with the relatively sharp peaks measured in tests of the cylinder models, these tone-like peaks were broader than those measured for electronically generated pure tones at the measurement bandwidth. At times, bandwidth was varied to determine whether these spikes were tones whose maximum amplitude would be independent of bandwidth or narrowband-random peaks whose intensity was proportional to 10 times the logarithm of bandwidth. All peaks proved not to be pure tones.

As velocity was increased to 52 and 64 m/sec (170 and 210 ft/sec), the number of strong peaks increased. It is likely that for this large ratio of model span to chord, small spanwise nonuniformities of airfoil contour and surface condition caused a greater spanwise variation in boundary layer properties as velocity and therefore Reynolds number was increased. Peaks also occurred at twice the frequency of the strongest peaks, with amplitudes about 25 dB below those of the fundamental frequencies. Tone frequencies predicted from calculated spanwise-uniform laminar boundary layer properties are shown by arrows and are discussed in a subsequent section, "DISCUSSION OF NOISE PREDICTIONS".

Narrowband spectra for this airfoil model at higher velocities of 79, 98, and 116 m/sec (260, 320, and 380 ft/sec) are shown in figure 23. As velocity was increased, there continued to be a multitude of peaks but their amplitudes reached a maximum and then decreased. Broadband background noise of the wind tunnel continued to increase, and the strongest peak was about equal to background noise at the highest velocity shown.

The variation of peak or tone frequency with velocity is shown in figure 24 for the strongest and second strongest peak generated by this constant-chord airfoil model. As with similar data presented in reference 11, the frequency of the strongest tone (solid circles) did not increase uniformly with increasing velocity. Instead, the next strongest tone (open triangles) at a higher frequency increased smoothly in frequency and amplitude until it was strongest. Arrows on the frequency axis denote the frequencies at which an integer number of acoustic half-wavelengths was equal to the airfoil

chord. Jumps in frequency of the strongest tone generally occurred across these frequencies. For a sound-generating process that includes flow oscillation at the airfoil trailing edge, sound radiation at these discrete frequencies would have caused flow oscillations at the leading edge and would significantly affect the airfoil pressure distribution. The calculated curve shown in this figure is discussed later.

Variations of overall sound pressure level and sound pressure level of the strongest tone with velocity are shown in figure 25 for this airfoil model and incidence. Tone strength was defined as the pressure-squared spectral density (1 Hz bandwidth) that corresponded to the measured peaks at the measurement bandwidth. OASPL was measured between 200 Hz and 20,000 Hz frequencies. The trend of tone strength was an increase with velocity to the fifth power at velocities less than about 60 m/sec (about 200 ft/sec) corresponding to a Reynolds number near 5×10^5 based on airfoil chord. Further increase of velocity caused this tone strength to remain approximately constant and then decay. This build-up followed by constant amplitude is typical of an acoustic feedback process. OASPL increased approximately with velocity to the eighth power, became approximately constant, and then increased as it became dominated by tunnel background noise.

Spanwise variations of tone surface pressure levels at 90% chord, and of normalized cross correlation coefficient between different spanwise positions as evaluated at zero delay time, are shown in figures 26 and 27 for 31 and 54 m/sec (100 and 178 ft/sec) velocities. Matched high-pass and low-pass filters were used with both correlation channels.

Tapered chord. - Narrowband spectra directly above the 2:1 tapered chord airfoil at -4° angle of attack are shown in figure 28 for 27, 34, 88, 98, and 107 m/sec (90, 110, 290, 320, and 350 ft/sec) velocities. Spectra for the lower velocities contain five and six closely spaced peaks having amplitudes within 15 dB of maximum. At the higher velocities the number of peaks was smaller and all but the strongest peaks disappeared into tunnel background noise. Narrowband spectra for 40, 52, 67, and 79 m/sec (130, 170, 220, and 260 ft/sec) velocities at -4° angle of attack are given in figure 29. These contain a multitude of peaks spread over a wider frequency range than those for the constant-chord airfoil at about the same velocities (figs. 22 and 23).

The variation of tone frequencies with velocity for this 2:1 tapered chord airfoil at 0° and -4° angle of attack are shown in figures 30 and 31. As with the constant-chord airfoil, the strongest tone at each velocity is represented by a solid circle. Tones having amplitudes within 5 dB of that tone, and within 10 dB where needed to represent the typical frequency range of prominent tones, are represented by open triangles. Except for the lowest frequency shown for the lowest velocity and zero angle of attack, all of these

frequencies have half-wavelengths equal to an integer fraction of the chord at some spanwise position on this tapered model. Jumps in frequency of the strongest tone occurred over about the same frequency ranges for both angles of attack, at frequencies near an integer number of kHz corresponding to an integer number of acoustic half-wavelengths approximately equal to the tapered airfoil's wide chord. Velocities and frequencies for these jumps differed from those for the constant-chord airfoil (fig. 24), which demonstrates that the frequency jumps were not resonances between the airfoil models, tunnel shear layers, and tunnel sidewalls. Strong tones measured at 0° angle of attack shifted to higher frequencies, and disappeared into tunnel background at lower velocities, than those at -4° angle of attack. However, strong tone frequencies at 0° approximately corresponded to frequencies at which weaker tones occurred at the other angle. For -4° angle of attack the strongest tone generally was at a lower frequency than those of other tones, as would be expected if amplitude is related to airfoil chord.

Variations of OASPL and dominant tone SPL with velocity for the 2:1 tapered chord airfoil at 0° and -4° angle of attack are shown in figures 32 and 33. For 0° angle of attack, these levels were approximately constant at low velocities and then decayed into the tunnel background. For -4° angle of attack, both levels increased approximately with velocity to the fifth power for velocities to about 50 m/sec (about 160 ft/sec). This velocity corresponds to a Reynolds number of about 5×10^5 based on the tapered airfoil's wide chord. This was the Reynolds number at which SPL of the constant-chord airfoil changed its velocity dependence at this same angle of attack. As with that model, tone SPL became approximately constant and then decreased with increasing velocity while OASPL became approximately constant and then increased.

Tone surface pressure levels and cross correlation coefficients for the 2:1 tapered chord airfoil at -4° angle of attack and 48 m/sec (157 ft/sec) velocity are shown in figure 34. The two selected frequencies corresponded to relatively strong tones in the far field. Surface pressure fluctuations and cross correlation coefficients for the higher frequency were strongest near the narrow end of the airfoil.

Far-field narrowband spectra at 90° direction for the 4:1 tapered chord airfoil at 0° angle of attack are given in figure 35 for 30, 43, and 55 m/sec (100, 140, and 180 ft/sec) velocities. The number of peaks was considerably larger, and was spread over a larger range of frequency, than for the 2:1 tapered chord airfoil. Narrowband spectra for 61, 70, 79, and 88 m/sec (200, 230, 260, and 290 ft/sec) velocities are shown in figure 36. As velocity was increased, the number of peaks decreased and their amplitudes decreased. Variations of tone frequency with velocity for the strongest peak, and for peaks within 10 dB of that peak, are given in figure 37. The

first jump in frequency of the strongest peak was an approximate doubling of frequency. At higher velocities, boundary layer transition near the wide-chord end of the model probably weakened and eliminated tones at the lower frequencies. Variations of OASPL and dominant tone SPL for this model are given in figure 38. There was a limited range of velocity in which OASPL varied with velocity to the fifth power before becoming approximately constant and then merging with background noise near 100 m/sec (328 ft/sec) velocity. Tone surface pressure levels and spanwise cross correlation coefficients for this model at 2° angle of attack and 52 m/sec (170 ft/sec) velocity are given in figure 39.

Directivity of airfoil noise without the upstream turbulence generator was examined using overall sound pressure levels calculated by summing the amplitudes of measured narrowband peaks. These overall levels therefore exclude tunnel background noise and include only the tones generated by the airfoil. Far-field directivity of these overall levels is shown in figure 40(a) for the constant-chord airfoil at 37, 61, and 92 m/sec (120, 200, and 300 ft/sec) velocities. Amplitudes generally decrease with increasing angular direction from upstream. This decrease was approximately given by cosine squared of half the angle from upstream, shown as solid curves. Such directivity is expected (refs. 25 and 26) for trailing edge noise caused by fluid disturbances convected past a trailing edge that is sharp compared with the disturbance. Far-field directivity for the 2:1 tapered chord airfoil at 55 m/sec (180 ft/sec) velocity and -4° angle of attack, and for the 4:1 tapered chord airfoil at 37 and 55 m/sec (120 and 180 ft/sec) velocities and 0° angle of attack, are shown in figure 40(b). Directivities for these two tapered-chord airfoils also generally varied in the manner expected for trailing edge noise.

Narrowband spectra for the constant-chord airfoil at 0° angle of attack in the turbulent wake of an upstream airfoil are shown in figure 41 for 79, 107, and 137 m/sec (260, 350, and 450 ft/sec) velocities. These spectra were obtained with 6.4 Hz bandwidth and 0 to 2000 Hz frequency range. Data are not shown for frequencies below 200 Hz because the chamber is not precisely anechoic (ref. 11) at those low frequencies. All of these spectra contained a superimposed 120 Hz modulation, apparently from the electrical power supply. Background noise spectra taken with the upstream wake-generating thick airfoil in place but without the test airfoil were 10 to 15 dB below these spectra except for frequencies below 200 Hz and are not shown.

DISCUSSION OF NOISE PREDICTIONS

Nonrotating Blades

Circular cross section. - The prediction of the far-field tone sound pressure level used a model in which the unsteady loading on the cylinder was represented by a distribution of dipoles in the spanwise direction. This concept was then used to relate measurements of unsteady surface pressure and spanwise correlation length to the far-field sound.

The link between the surface measurements and far-field sound pressure levels is provided by equation (A5) of Appendix A describing dipole radiation from a constant-diameter cylinder in a flow having no spanwise variation of velocity. For a measurement position directly above midspan, the exponential term in the numerator and the Mach number convection term in the denominator are both equal to unity. Mean square lift coefficient was calculated from the surface pressure fluctuation based on the approach discussed in Appendix B. Conceptually, this approach used the unsteady Bernoulli equation in which the velocity potential contained two terms. One term represented the steady-state flow about the cylinder while the other represented an oscillating circulation about the cylinder. The measured surface pressure fluctuations then permitted calculating the circulation term from which the lift coefficient was obtained. Resulting lift coefficients generally agreed with those of other investigations at the same Reynolds numbers as shown in figure 5.

In the case of the constant-diameter cylinder without the upstream generator, the lift coefficient was calculated using the average surface pressure levels in figure 15. Surface correlation lengths were obtained from figure 19. The spanwise distance ℓ_y over which the lift fluctuation was assumed to act at constant frequency was taken equal to the cylinder span b. The results of these predictions, shown in figure 10, indicate good agreement with measured data at 31 m/sec (101 ft/sec) and 40 m/sec (131 ft/sec). At 63 and 76 m/sec (206 and 250 ft/sec) the prediction was approximately 6 dB below the data. In the latter case this is attributed to the Reynolds number being in the transition regime in which coherent vortex shedding did not seem to occur. Thus the dipole concept no longer described the acoustic radiation accurately.

For the 2:1 tapered cylinder, the tone existed only over a small portion of the cylinder span so the length ℓ_y over which the lift acted was taken equal to the spanwise integral of rms lift coefficient at constant frequency, divided by the maximum value of that rms lift coefficient. Here, the maximum rms lift coefficient corresponded to the maximum surface pressure

level displayed in figure 17. The integration was performed numerically over the spanwise variation of tone surface pressure level in figure 16. Also, the two-sided correlation length $2\ell_y$ was replaced by the length identified in figure 20 for the tapered cylinder.

The predicted and measured far-field sound pressure levels for the 2:1 tapered cylinder are shown in figure 42 for the four velocities at which surface measurements were conducted. Agreement is within 4 dB in all cases, providing confidence in the approach.

Airfoil cross section.

Far-field sound pressure levels. - By application of theories summarized in reference 5, the sound field produced by unsteady loading on an airfoil can be represented by a distribution of dipoles over the airfoil surface. The present section uses this approach to relate measurements of unsteady pressure on the airfoil surface to far-field sound.

If it were feasible to place pressure transducers at every point on the airfoil surface, the contribution of each point to the far field pressure could be directly summed. As this is not practical, the approach followed here is to propose a possible model for the unsteady loading and to use the measured surface pressure to determine necessary parameters in the model.

The model chosen here for the airfoil surface pressure P_s is

$$P_s(x,y,t) = P_{te}(y)\, e^{-\alpha x/c}\, e^{i(\omega t - kx)} \qquad (1)$$

where y is the spanwise coordinate and x is the chordwise coordinate, with the airfoil trailing edge at x = 0 and the leading edge at x = c. Thus, x is here assumed to be measured opposite to the flow direction. The phase $\omega t - kx$ indicates that there is an acoustic wave propagating from the trailing edge toward the leading edge.

The trailing edge pressure P_{te} is a stochastic variable in y. One reason for choosing this particular model is the following argument. Since the sound is produced by a trailing-edge mechanism, one might expect that the chordwise distribution would be determined once the distribution of trailing-edge dipoles is specified. Thus the present model combines a stochastic variation in y with a deterministic variation in x.

The pressure given by equation (1) propagates upstream at the speed of sound, whereas one might expect a propagation velocity equal to the difference of the sound speed and the flow speed. Since the measurements were taken at low Mach number, this difference is negligible. The variation of pressure amplitude with chordwise position was not measured in the present experimental program. Consideration of the data of reference 11 showed that a reasonable value for α was 1.2. The particular value chosen is not really very important since it has little effect on the calculation.

Since far-field pressure measurements were made directly overhead, one needs to know the fluctuation in overall lift in order to predict the far-field sound. Because this is a dipole type of mechanism, the pressure will be assumed to be anticorrelated on the upper and lower airfoil surfaces. Integration of equation (1) over chord then gives the spanwise sectional lift as

$$L(y) = 2P_{te}(y)\ \frac{c}{\alpha + ikc}\ (1 - e^{-\alpha - ikc})\, e^{i\omega t} \tag{2}$$

Since the acoustic wavelength λ was approximately equal to or greater than the chord in the present experiment, $kc = 2\pi c/\lambda$ and equation (2) can be approximated by

$$L(y) = -2\frac{i}{k} P_{te}(y) e^{i\omega t} \tag{3}$$

independent of the particular value chosen for α.

The far-field pressure produced directly above the airfoil by the dipole distribution over the airfoil is then

$$P_{ff} = \frac{i\omega}{4\pi c_0 R}\, e^{i\omega(t - z/c_0)} \int_{span} L(y)\, dy \tag{4}$$

Multiplying equation (4) by its complex conjugate and using equation (3) for $L(y)$ gives the following equation for the far-field PSD

$$S_{pp} = (2\pi R)^{-2} \iint_{span} P_{te}(y)\, P_{te}^{*}(y)\, dy, dyz \tag{5}$$

It appears from the data that there were discrete regions on the airfoil that produced definite frequencies. That is, a given tone was produced by only a small region of the trailing edge. Adjacent regions produced a tone at slightly different frequencies. A reasonable model for a given tone generating region is

$$P_{fe}(y) = P_{max}\, e^{-y^2/\pi(\ell_y)^2} \tag{6}$$

Then, from equation (5)

$$S_{pp} = \left(\frac{\ell_y}{2\pi R}\right)^2 S_{QQ} \tag{7}$$

where S_{QQ} is the maximum PSD of the pressure on the airfoil near the trailing edge at the given frequency.

The length ℓ_y can be considered to be a correlation length and can be determined from cross correlation measurements. These cross correlation plots were shown in figures 26, 27, 34, and 39. One difficulty is that the data points were rather widely spaced so that the correlation length cannot be precisely determined. An alternative procedure is to work with the tone surface pressure levels and to consider the variation of amplitude with position.

From the above sorts of considerations one can arrive at an estimate for correlation length. Using equation (7) this then leads to a prediction of the quantity 10 log (S_{QQ}/S_{PP}), the ratio of surface to far-field PSD. The results of these calculations are shown in Table I along with the experimentally measured values. It should be emphasized that the calculated values are approximations which serve to give some confidence in the type of mechanism considered. Since this difference depends on correlation length squared, a factor of two change would lead to a 6 dB change in the predicted value of 10 log(S_{QQ}/S_{PP}), and the measurements permit only a crude estimate of correlation length. Also, for the constant chord airfoil there could be more than one spanwise region on the airfoil generating the same frequency. The existence of more than one such region would lead to a decrease in the predicted value of surface to far-field pressure ratio. Finally, because of the rapid variation of surface pressure with spanwise position, one cannot be certain that the maximum value of surface pressure has been measured.

In view of these uncertainties, the agreement shown in Table I seems reasonable. The predictions differ from the data by less than 4 dB for three cases and up to 8 dB for the four others. For most of the comparisons the predicted value of surface to far-field pressure ratio is less than the measured values. Thus, if measured values of surface pressure were divided by the predicted value of this ratio, far-field sound pressures would be overpredicted. One possible source of error is the assumption that pressures on the airfoil upper and lower surface were anticorrelated. If there was an in-phase component as well as a component 180° out of phase, the measured sound level could be decreased significantly from what one would predict. Another possible source of error is the assumed rate of chordwise attenuation of the airfoil loading. If this were significantly different from that assumed in equation (1), the predicted sound could be affected. Probably the most critical uncertainty is the correlation length. Nevertheless, the comparison between theory and experiment in Table I seems to show that values of 5 to 10 cm for spanwise correlation length are reasonable, with this length tending to be smaller for the tapered airfoils.

Narrowband spectra for the airfoil in the turbulent wake of an upstream airfoil were shown in figure 42 for 79, 107, and 137 m/sec (260, 350, and 450 ft/sec) velocities. These spectra were obtained with 6.4 Hz bandwidth at 0 to 2000 Hz frequency range. Data are not shown for the 0 to 200 Hz frequency range because the chamber is not precisely anechoic at these low frequencies. The spectra for all frequencies contained a superimposed 120 Hz modulation from the power supply. Background noise spectra taken with the upstream airfoil in place were 10 to 15 dB below these spectra for this frequency range and are not shown. The figure also contains spectra calculated for these test conditions assuming uniform isotropic turbulence rather than the actual, relatively narrow, spatially nonuniform wake. A method that was reported in reference 22 to give good prediction of spectra for airfoils with incident turbulence was utilized. In that method, local lift coefficient response spectrum per unit normalized incident turbulence in an incompressible flow is obtained from the solution of Filotas (ref. 23). Separate analytic equations are used for large and for small reduced frequencies. The resulting lift response per unit turbulence is multiplied by the measured or predicted upwash spectrum to determine a lift force fluctuation spectrum. The conventional dipole noise radiation equation, as modified by Hayden (ref. 24) for source noncompactness effects at small ratios of chord to acoustic wavelength, then served as the acoustic transfer function between lift force spectrum and acoustic radiation spectrum.

This calculation of narrowband acoustic spectrum was given by

$$SPL = 20\log(\pi\rho V^3 b \sin\theta)(2c_0 R P_{ref})^{-1} + 10\log(\overline{v^2}/V) + 10\log\left[(\Delta F)\Lambda/V\right]$$
$$+ 20\log(F_c/V) + 10\log\overline{S_E^2} - 10\log\left[1+(\pi F_c/C_0)^2\right] + \log(VE/\overline{v^2}\Lambda) \tag{8}$$

where the equivalent Sears function for a three-dimensional airfoil with incident turbulence was taken from equation (35) of reference 23

$$\overline{S_E^2} = \begin{cases} \ell n\left[1.2+(\pi c/2\Lambda)^2\right] \Big/ \left[\ell n\, 1.2+3(\pi c/2\Lambda)^2\right], & fc/V \le (2/\pi)(\Lambda/c) \\ \ell n\left[1.2+(\pi^2 fc/V)^2\right] \Big/ \left[\ell n\, 1.2+3(\pi^2 fc/V^2\right], & fc/V > (2/\pi)(\Lambda/c) \end{cases} \tag{9}$$

and the normalized turbulence spectrum was approximated by equation (1-95) of reference 25.

$$VE/\overline{v^2}\Lambda = 4\left[1+(2\pi f\Lambda/V)^2\right]^{-1} \tag{10}$$

Thus the narrowband sound radiation spectrum was calculated as a function of reduced frequency, bandwidth, Mach number, normalized turbulence intensity, ratio of far-field distance to airfoil chord, ratio of span to chord, and ratio of turbulence integral scale length to chord. For this chord, acoustic noncompactness is predicted to decrease the spectrum amplitude at frequencies significantly greater than 1000 Hz.

As is shown in figure 42, the general spectrum shape and the shift of peak frequency with increasing velocity were fairly well predicted. Amplitudes were overestimated by about 4 dB. It is likely that this difference between predictions and data was caused by spatial nonuniformity of the turbulent wake convected past the airfoil. The analytical method had been developed and validated for flows having uniform turbulence intensity over large distances normal to the airfoil chord. In contrast, the actual

turbulent wake thickness for which rms turbulence intensities were greater than 70% of maximum was only about 5 cm (2 in.) or about half the airfoil chord. This narrow wake may have caused the lift force fluctuations to be only about 2/3 the levels predicted for uniform turbulence, resulting in the overestimate of measured acoustic intensity.

Tone frequencies. - One explanation of airfoil tones (ref. 26) has regarded them as trailing edge noise caused by Tollmein-Schlichting instabilities of the laminar boundary layer on the airfoil pressure surface. Of the range of frequencies that are unstable at the airfoil trailing edge, that frequency which has strongest amplitude will cause a feedback oscillation within the boundary layer. One tone, rather than broadband radiation over a sharply defined range of frequencies, would then be radiated. The dependence on Tollmein-Schlichting laminar instability explains why increasing the angle of attack, which greatly increases the chordwise extent of accelerating pressure gradient on the pressure surface of NACA 0012 airfoils, should increase the maximum velocity at which airfoil tones occur. It also explains why use of boundary layer trips on the airfoil pressure surface, either near the leading edge or near 3/4 chord, has been observed to eliminate this noise.

From the laminar boundary layer investigation reported in reference 27, the frequency at which Tollmein-Schlichting instability waves had maximum amplitude was given by the upper branch of the neutral stability contour evaluated at the local Reynolds number. (Minimum amplitude corresponded to the lower branch.) Shen's calculated values (ref. 28) for this contour were in best agreement with data for laminar boundary layers on flat plates. For convenience, the airfoil boundary layers were assumed equal to those for flat plates with zero pressure gradients so that local boundary layer displacement thickness could be easily related to airfoil chord. Then the predicted tone frequency, Hz, is given by

$$f=(2\pi)^{-1}(1.73)^{-1}(\beta\delta^{*}/V)V^{3/2}(c\nu)^{-1/2} \qquad (11)$$

where β is the angular frequency for neutral stability. The solution in reference 28 gave the ratio of reduced frequency $\beta\delta^{*}/V$ to Reynolds number referenced to displacement thickness as a function of Reynolds number. This reduced frequency for the upper neutral stability contour was calculated to decrease from 0.20 to 0.10 as Reynolds number based on flat plate chord increased from about 5×10^{4} to 1×10^{6}. If reduced frequency is assumed constant over a limited range of Reynolds number, the predicted tone frequency given by this equation would vary with velocity to the 3/2 power and inversely with the square root of chord. These predicted trends had been noted in reference 11 to give a good general description of available data.

Calculated tone frequencies for each flow velocity are shown with the narrowband spectra of figures 22 and 23. The variation of tone frequency with velocity as calculated for the constant-chord airfoil from this laminar instability theory was shown in figure 24. Except for velocities just below those at which there was a jump in frequency of the strongest tone, and for the highest test velocities, these calculations from flat-plate laminar boundary layer theory closely predicted the frequency of either the strongest or next strongest observed tone.

Tone frequencies calculated by this method for the narrow chord and the wide chord of the 2:1 tapered chord airfoil were shown as arrows on the frequency axis of narrowband spectra (figs. 28 and 29). These calculations predict the range of frequency for which acoustic tones occurred at low velocities. As velocity was increased, boundary layer transition at the wide-chord end eliminated the low-frequency tones. The corresponding calculated variations of tone frequency with velocity for both ends of the 2:1 tapered chord airfoil were given in figures 30 and 31 which contain data for two angles of attack. Because of the dependence of reduced frequency on Reynolds number, the ratio of these calculated frequencies at constant velocity was not the square root of two but varied from 1.5 at the lower to 1.7 at the higher velocities. These calculated curves generally enclosed the frequencies at which strong tones were radiated. Increasing the angle of attack increased the range of frequencies for which tones occurred at constant velocity. At low velocities the strongest measured tones occurred at frequencies associated with the wide-chord end of the model. Increasing the velocity and therefore the Reynolds number per unit length would have caused boundary layer transition at that end. Tones near the predicted low frequency were eliminated and the origin of strongest sound radiation along the model span was moved toward the narrow-chord end. These same trends occurred to a greater extent with the 4:1 tapered chord airfoil (figs. 35, 36, and 37). Airfoil tone noise from nonrotating airfoils is therefore shown to occur at frequencies for which Tollmein-Schlichting instability of the pressure-surface laminar boundary layer has maximum amplitude at the airfoil trailing edge.

Rotating Blades

Circular cross section. - Before comparing the calculated and measured spectra, it is useful to examine those spectra and qualitatively determine the measured trends. Comparisons given in figure 12 of reference 1 and figures 31 and 33 of reference 2 showed that tip shape of blades with circular cross-section generally had no effect on noise radiation. The only exception was for the open-end blades (model configuration 00) which developed an organ-pipe resonance in the 1600 Hz to 2000 Hz one-third-octave bands,

corresponding to the depth of the open-tip. Because only the squared-tip blades (model configuration 01) were tested both in the wind tunnel and outdoors, data for this model will be analyzed as representative of rotating blades with circular cylinder cross-section.

Directivity of noise from the cylindrical blades was assumed to be a sum of vortex noise which varies as cosine squared of the measurement angle from the rotational axis and thickness noise which varies as sine squared of this angle. To examine this assumption, OASPL directivity measured for the cylindrical blades tested outdoors rotating in their shed wakes is shown in figure 4 . The data for five rotational speeds are compared with curves calculated by arbitrarily fitting vortex-noise directivity to OASPL measured on the rotational axis and thickness-noise directivity to that measured in the rotor disc plane. The resulting curves are seen to give close prediction of OASPL at intermediate measurement direction angles. Therefore, attention was concentrated on vortex noise measured on the rotational axis.

Scaling of on-axis vortex noise spectra for the rotor with cylindrical blades in the wind tunnel with shed wakes blown downstream is shown in figure 44. Frequency was scaled by use of Strouhal number based on cylinder velocity and rotational tip speed. In the upper part of this figure, one-third octave sound pressure levels were scaled by subtracting sixty times the logarithm of rotational tip speed, m/sec. This sixth power scaling law would be correct if rms lift coefficient, correlation length, and Strouhal number were constant along the blade radius as was assumed by Yudin (ref. 9). This scaling law generally caused the velocity-adjusted spectra to agree within a spread of 4 dB for Strouhal numbers less than 0.05 and greater than 0.5. At intermediate Strouhal numbers where maximum amplitudes occur, increased rotational speed caused a consistent decrease of velocity-adjusted amplitude. Failure of the sixth power velocity scaling law for OASPL of these data had been shown in figure 13 of reference 1. It was noted in reference 1 that OASPL could be approximately matched by two sixth-power scaling curves, one for the three lower and the other for the two higher rotational speeds. The change in absolute level was attributed to exceeding a critical Reynolds number of 400,000 based on rotational tip speed. In contrast, normalized spectra shown in figure 44(a) fail to follow the sixth-power velocity scaling law between the lowest Reynolds numbers of about 220,000 and 350,000. It should be also noted that following the assumptions of reference 9, power spectral density should vary with Strouhal number to the sixth power. The resulting one-third octave levels should then increase 21 dB per octave of frequency. The spectrum measured for the lowest rotational speed follows this behavior for Strouhal numbers from 0.08 to 0.125; spectra for higher rotational speeds have considerably smaller slope. One possible interpretation of these data would be that rms lift coefficient, spanwise correlation length, or both these quantities decrease rapidly at local Reynolds numbers greater than about 140,000.

These spectra are plotted in figure 44(b) adjusted for a fourth-power velocity law. This scaling law would correspond to noise radiated by a fluctuation of mass flow. Agreement between spectra for different rotational speeds is improved for Strouhal numbers less than 0.5. Very good agreement is obtained only for Strouhal numbers between 0.2 and 0.5. This fourth-power dependence may be a coincidental result of the variations of cylinder rms lift coefficient and correlation length with Reynolds number at these test conditions.

Scaling of on-axis vortex noise spectra for the rotor with cylindrical blades operating within its shed wake in outdoor tests was shown in figure 22(a) of reference 2. The data were scaled assuming a sixth-power velocity law. Except for Strouhal numbers larger than about one, increasing rotational speed caused a decrease of velocity-adjusted sound pressure level. These spectra are replotted in figure 45(a) assuming a fourth-power velocity scaling law. Spectra for these blades tested in the wind tunnel at zero forward velocity are shown in figure 45(b) for the same fourth-power velocity scaling law. Spectra for Strouhal numbers up to about 0.5 are brought into general agreement by this scaling law. For Strouhal numbers less than about 0.16, the velocity-adjusted spectra still have largest amplitude at lowest rotational speed. This portion of the spectra would be better matched by a smaller empirical velocity exponent such as 3. The spectrum slope associated with such an empirical velocity law would be 12 dB per octave, in good agreement with the data. Both the empirical exponent of a velocity law that produces agreement for velocity-adjusted spectra at Strouhal numbers less than 0.2, and the measured spectrum slope at these Strouhal numbers, differ from that expected for the classical sixth-power velocity law (ref. 5) for vortex noise. It is likely that for these test Reynolds numbers the product of mean square lift coefficient fluctuation, correlation length, and local rotational velocity to the sixth power actually varies as local rotational velocity to about the third power.

Vortex noise of rotating cylinders was found (ref. 2) to have a broadband spectrum. It is likely that vortex noise originating at each radial station is narrowband random with a center frequency given by a constant Strouhal number referenced to local relative velocity. The calculation of vortex noise regarded each of a discrete number of radial stations as producing pure tones at its center frequency. Intensity of each tone was assumed as that for a cylinder with coherent oscillations along a spanwise distance equal to the correlation length, at a velocity equal to the local rotational velocity. Root mean square lift coefficient and correlation lengths were obtained from curves faired through the collection of data for nonrotating cylinders given in figures 5 and 6. Acoustic intensity in each one-third octave band was then calculated by summing the intensity of all tones within that band.

To perform this calculation, it is necessary to make some assumptions for the spacing of acoustically radiating regions. One possible method would assume that the radial distance between centers of each tone-producing region was some constant fraction of correlation length or cylinder diameter. Alternately, radiating regions could be assumed to differ by a constant interval of frequency or Strouhal number. It can be shown that use of constant increments of radial distance is equivalent to constant increments of Strouhal number. Constant increments of frequency would give a more rapid increase of OASPL with rotational speed than would be calculated for constant increments of Strouhal number. Because the test conditions included the critical Reynolds number regime, radial increments equal to a constant fraction of correlation length gave a more rapid increase of OASPL with rotational speed.

Spectra measured on the rotational axis two rotor diameters ahead of the cylindrical blades with their shed wakes blown downstream are compared with calculated one-third octave spectra in figure 46. The two symbols denote blades with squared tips (squares, runs 38-41) and semisphere tips (circles, runs 50-53). Radial increments between tone-producing segments were taken as one-third the local correlation length for calculations shown as dash lines. The solid lines represent 5 Hz frequency increments between adjacent segments. Both calculations excluded noise from radial positions within one cylinder diameter from the tip. This arbitrary tip effect was needed to prevent calculation of excessive noise in the one-third octave band that contains a Strouhal number of 0.2 referenced to rotational speed. Experimentally, changing the blade tip shape had no effect on sound radiation. Both calculations produced irregular spectra at low one-third octave center frequencies where only a small number of tones occurred within each frequency band. Use of a constant fraction of correlation length (dash lines) closely predicted the vortex noise spectrum at the lowest rotational speed. It did not give as much rounding of the spectrum with increasing speed as had been measured. Use of a constant frequency increment (solid lines) gave a better prediction of the change in spectrum shape with increasing rotational speed. Both methods gave nearly the same values for OASPL which were within 1.4 dB of the data. Both methods gave no explanation for the spread of peak amplitude to one or two one-third octave bands above those which corresponded to a Strouhal number of 0.2 referenced to rotational tip speed.

The spectrum measured at the lowest speed could also be matched by using radial increments of half a cylinder diameter. For this geometry, that radial increment corresponds to increments of about 0.003 for Strouhal number. These spectra are not shown in figure 46 to avoid excessive clutter of the figure. Spectra calculated with this approximation for larger rotational speeds had low-frequency amplitudes between those given by the other two methods and a

rounded shape similar to that for constant frequency increment. Amplitudes at constant frequency, and OASPL, became increasingly underpredicted as rotational speed was increased.

The calculation which used a constant increment of frequency gives one-third octave spectrum levels that are independent of rotational speed except for the highest frequency band. Measured and calculated spectra for these four rotational speeds are superimposed in figure 47. It can be seen that the measured vortex shedding noise for frequencies from 125 to 400 Hz did behave in this manner.

This same method was used for calculating vortex noise of cylindrical blades rotating in their own shed wakes. It was found in reference 18 that upstream turbulence decreases rms lift coefficient and correlation length for untapered cylinders in nonrotating flow. This effect was considerably larger at a subcritical Reynolds number than in the critical Reynolds number regime. As sketched in figures 5 and 6, turbulence was assumed to have no effect on lift coefficient and correlation length at a Reynolds number of 300,000. Below this Reynolds number, the increase of each quantity with decreasing Reynolds number was arbitrarily assumed to be halved. For larger Reynolds numbers, rms lift coefficient was assumed to decrease to the levels reported in reference 16. Spectra measured at microphone 5 on the rotational axis two rotor diameters ahead of the cylindrical blades in the wind tunnel at zero axial velocity are compared with calculated spectra in figure 48. These data for cylindrical blades rotating in their shed wakes are from runs 31-34 for the squared-tip blades. At frequencies above 80 Hz and below a Strouhal number of 0.2 based on tip speed, measured one-third octave SPL's were independent of rotational speed as predicted by the calculation. The calculated spectra were considerably steeper and more sharply peaked than was measured, but calculated and measured OASPL's agreed within about 1.5 dB.

Airfoil cross section.

High-frequency spectra. - The most distinctive feature of spectra measured with the helically twisted NACA 0012 airfoil blades and shed wakes blown downstream was a peak at high frequencies. Spectra measured two rotor diameters upstream on the rotational axis are shown in figure 49 for these blades with two different tip shapes at 700 and 850 rpm rotational speeds. Also shown are background noise spectra for the wind tunnel at approximately the same axial velocity and the drive motor at the same rotational speeds but without blades. The background noise contained peaks in the 125 and 500 Hz one-third octave bands which influenced spectra measured with the blades. However, blade spectra for frequencies greater than 800 Hz were considerably stronger than background. The blades with squared-off tips (model configuration 20) had sharply peaked spectra at high frequencies. Adding a rounded body of revolution to the blade tip (configuration 21) greatly decreased the peak.

Scaling of on-axis spectra for the blades with squared-off tips had been shown in figure 24(a) of reference 2. Amplitude was normalized for a sixth-power velocity law by subtracting sixty times the logarithm of rotational tip speed. Frequency was scaled by dividing one-third octave center frequencies by the rotational tip speed. The low-frequency portion of those scaled data for 400 rpm did not agree with scaled data for other speeds, probably because it was dominated by background noise. The high-frequency portion of these scaled spectra for the blades with shed wakes blown downstream are shown in figure 50(a) for the squared-off blade tips and figure 50(b) for rounded blade tips. Spectra for the squared-off tip were coalesced at large frequencies and exhibited a well-defined peak with amplitude 10 to 15 dB above the normalized level measured at lower frequencies. In contrast, scaled spectra for the same blades but with rounded tips had a broader, less well-defined peak with about 5 dB increase of amplitude. The scaled frequency at this peak was about half an octave smaller than that for the squared-off blade tip.

Normalized high-frequency peaks measured on the rotational axis for the untwisted rotor with airfoil blades operating in their shed wakes are shown in figure 51. For tests conducted in the wind tunnel at zero axial velocity (fig. 51(a)), the squared-off tips within their shed wakes produced a smaller peak than with the wake blown downstream (fig. 50(a)) but a stronger peak than that for the rounded tips with the wake blown downstream (fig. 50(b)). Blades with rounded tips produced roughly the same scaled spectra whether in (fig. 51(a)) or out (fig. 50(b)) of their shed wakes. Narrowband spectra for these two configurations, shown in figure 33 of reference 2, indicated no effect of tip shape because they did not extend above 2000 Hz frequency where these peaks occurred. The untwisted blades were tested outdoors only with squared-off tips. Scaled spectra for this condition (fig. 51(b)) were about 10 dB below those for the wind tunnel at zero axial velocity but they continued to show a well-defined peak. Adding No. 14 grit roughness to the blade leading edge did not change the normalized spectra (fig. 51(b)).

One possible explanation for the high-frequency peak would be the presence of airfoil tone noise (refs. 11, 26, and 29). As discussed previously, constant-chord nonrotating airfoils having large chordwise extents of laminar flow on one surface will radiate sound at the frequency for which Tollmein-Schlichting instability waves have maximum amplitude at the trailing edge. Blade rotation would produce a radial variation of relative velocity and therefore of tone frequency. If this is the blade tone noise mechanism, frequency should be normalized as the quantity $f(c\nu)^{1/2}V_t^{-3/2}$ where ν is the kinematic viscosity. Maximum scaled tone frequency in nonrotating flow can then be obtained from equation (11) where the last term on the right-hand side is a function of Reynolds number given by laminar boundary layer instability theory. For nonrotating flow at the tip Reynolds numbers of these tests, this term would be approximately equal to 0.10 so the normalized spectra would be expected to peak at a frequency parameter near 0.09. Also, if tone

amplitude for nonrotating airfoils varied with relative velocity to the sixth power for these test Reynolds numbers, it can be shown that power spectral density should vary with frequency to the 14/3 power. The resulting one-third octave spectra would then increase with a slope of 17 dB per octave. Because airfoil tone noise is a feedback process, its amplitude can saturate causing a smaller velocity exponent for amplitude and therefore a smaller slope. Helicopter tail rotor spectra measured along the rotational axis, plotted in figures 45 through 49 of reference 29, also exhibited a high-frequency peak. The spectrum amplitudes grew with this expected slope at moderate collective pitch angles (3° to 9°) and smaller slopes at larger angles. Those blades had constant chord and rounded tips.

Spectra normalized for this frequency behavior are plotted in figure 52 for both tip shapes of the helically twisted rotor with blade wakes blown downstream. The high-frequency peak measured with the rounded tip at different rotational speeds was coalesced about as well by this frequency parameter as by the simple scaling of figure 50(b). Maximum amplitude generally occurred in the one-third octave bands centered at frequency parameters near 0.01 and 0.0125. Thus the peak frequency was about one-third octave larger than the value of 0.09 predicted for airfoil tone noise in nonrotating flow. As with the tail rotor tests reported in reference 29, tone noise apparently occurred on these rotating blades at considerably larger Reynolds numbers than would be expected from tests of nonrotating airfoils. The measured spectrum slopes were only about half the 17 dB per octave predicted for strong tone noise and measured with the cited tail rotor.

In contrast, spectra for different rotational speeds of the blades with squared-off tips were spread apart by this frequency scaling law. Peak amplitudes occurred at scaled frequencies up to twice that predicted for nonrotating flow. Much better agreement was obtained by the scaling law of figure 50 as would be expected for bluff-body vortex shedding noise. For such noise, and rms lift coefficient, and correlation length independent of spanwise position, power spectral density should increase with frequency to the sixth power. The resulting predicted one-third octave spectrum slope of 21 dB per octave, shown in figures 44(a) and 52(a), is in good agreement with the measured spectra. Amplitude of this spectrum peak had been decreased by rotating the untwisted blades within their own wake but had not been changed by adding surface roughness to cause boundary layer transition (fig. 51(b)). Thus the noise behavior resembles that expected for bluff-body vortex shedding along the blade radius. If the appropriate flow velocity actually is the rotational tip velocity, the peak scaled frequency near 70 m^{-1} and a Strouhal number of 0.2 would correspond to about 3 mm thickness. This dimension is about three times the nominal trailing-edge thickness of an NACA 0012 airfoil with the tested blade chord. There is no obvious reason why removing the rounded blade tip should have affected the trailing edge thickness for an

extensive part of the blade radius, as would be needed to produce the observed spectrum shape. Broadband vortex noise of lifting rotors has been hypothesized (ref. 30) to be trailing-edge noise caused by the thick turbulent viscous core of the blade tip vortex as it is convected around the tip and past the trailing edge. These blades had been operated at zero local incidence to eliminate the lifting vortex. However, rotation of the blades would be expected to produce centrifugal flow of boundary layer air. This airflow might have generated bluff-body vortex shedding noise as streamlines near the blade tip moved downstream and over the squared-off tip. The range of radiated frequencies might have been caused by the chordwise variation of local tip thickness. Such noise would be expected to have a spectrum slope less than was measured, so this possible explanation may not be correct.

Blades operating within shed wakes. - Narrow-band spectrum measured along the rotational axis for blades with NACA 0012 airfoil sections rotating in their shed wakes were found to be dominated by tones at harmonics of blade passing frequency. However, one-third octave spectra at these positions had the appearance of broadband noise. Simple theories are available (ref. 22) for calculating broadband noise of isolated airfoils in turbulent flow, so it was of interest to determine whether those methods would predict the measured spectra. It was shown in figures 23(a) and 25(a) of reference 2 that on-axis spectra measured at the outdoor whirlstand and in the wind tunnel at zero airspeed were coalesced when one-third-octave data, normalized by subtracting sixty times the logarithm of rotational tip speed, were plotted against the ratio of frequency to tip speed. These data presentations are reproduced in figure 53 herein. The spectra increase about 12 dB per octave at low frequencies corresponding to a power spectral density that varies with frequency cubed. They decrease 9 dB per octave at high frequencies corresponding to a power spectral density that varies inversely with frequency to the fourth power. Power spectral densities calculated by the method recommended in reference 22 would follow this high-frequency decay rate but would increase with frequency squared at low frequencies.

Helicopter rotor discrete-frequency rotational noise had been predicted in references 31 and 32 by representing the blade loads over the entire rotor by their spectra as measured at 80% radius. Following the same simplifying approximation, on-axis broadband noise of the two-blade untwisted rotor moving in its own turbulent wake was approximated as that from a nonrotating airfoil with chord equal to the blade chord, span equal to the blade diameter, and velocity equal to 0.8 times the rotational tip speed. One-third octave spectra were than calculated from equation (23) of reference 22, which is given by equation (8) herein with the bandwidth taken as 0.232 f.

In this comparison, velocity was taken as 0.8 times the rotational tip speed. Turbulence level and turbulence length scale were arbitrarily varied until general properties of the measured spectra were matched. Resulting

calculated curves are shown in figure 53 for the lowest, second lowest, and highest rotational speeds. Turbulence level was taken as 0.35% for the outdoor tests and 0.7% for the wind tunnel, and 3 cm was used for the turbulence scale length. These very small turbulence levels, and a scale length of about twice the turbulent wake thickness at the blade trailing edge, were sufficient to match the general levels and behavior of measured spectra. The measured 4 dB decrease of normalized peak amplitude with increasing rotational speed was predicted by the noncompactness compressibility factor, and the predicted 6 dB decrease of amplitude at larger reduced frequencies agreed with the wind tunnel data. Calculated spectra were less sharply peaked than the data. It is likely that the turbulence spectrum in the blade rotational plane is not that for isotropic turbulence as given by equation (10) but itself is somewhat peaked. The second peak in these measured spectra at very high frequencies appears to be airfoil vortex noise.

Spectra measured on the rotational axis of untwisted airfoil blades operating in their own wakes were found by narrowband analysis to contain peaks at large harmonics of blade passing frequency. An example 10 Hz bandwidth spectrum measured in the wind tunnel at 850 rpm, taken from figure 2 of reference 2, is shown in figure 54(a). This spectrum has peaks at more than thirty harmonics of blade passing frequency with a broad maximum centered near the 15th harmonic. Narrowband spectra for the cylinder blades operating in their shed wakes, also given in reference 2, did not contain these peaks. Uniformly distributed turbulence would be expected to produce broadband noise rather than tones. Tone radiation by isolated rotating blades at zero flight speed has been attributed (ref. 33) to chopping of turbulent eddies by blades having nonzero unsteady lift response. Tones observed on the rotation axis with untwisted airfoil blades operated in their own wakes outdoors might have been caused by atmospheric turbulence convected through the rotor disc by occasional gusts. When the wind tunnel is run at zero mean flow speed the eddies arise from the wakes of previous blade passages. Starting with a simple analytical model for the sound spectrum produced by airfoil blades chopping through turbulent eddies (ref. 34), it is possible to calculate correlation lengths of these eddies. Cylindrical blades operated in air containing these same eddies would not radiate tone noise because cylinders have negligible lift force response to incidence fluctuation.

Acoustic power radiated along the rotational axis will be proportional to the second time derivative of the loading. Thus the acoustic power spectral density S_{pp} will be proportional to the product of frequency squared and the overall rotor loading power spectral density S_{LL}

$$S_{pp}(\omega) = A\omega^2 S_{LL} \tag{12}$$

In terms of the correlation functions of acoustic pressure and blade loading,

$$R_{pp}(\tau) = -A \frac{d^2}{d\tau^2} R_{LL}(\tau) \tag{13}$$

The autocorrelation of the loading $R_{LL}(\tau)$ can be written as

$$R_{LL}(\tau) = g(\tau) \sum_{n=-\infty}^{\infty} f(\tau - 2\pi n/B\Omega) \tag{14}$$

where f and g are general functions of frequency. If this loading is generated by turbulence with a transverse scale much smaller than the distance between rotor blades, f will be a sharply peaked function of time and g a broad function of time. This type of analytical model of the autocorrelation function of blade loading is sketched in figure 54(b). The sharply peaked function f, also sketched in this figure, is similar to the lift cross-correlation that would be incurred by the rotor blade moving rectilinearly through the same turbulence field.

If the turbulence has a long axial scale or if its rate of movement through the rotor plane is small, then one would expect a strong blade-to-blade cross-correlation at a retarded time equal to the blade passage time. In other words, if one rotor blade experiences a certain force pattern when it passes a specified azimuthal position, the following blade would be expected to experience much the same force when it passes the same point at a time $T = 2\pi/B\Omega$ later. Thus, $g(\tau)$ represents the rate at which turbulent eddies decay or pass out of the rotor plane.

The Fourier transform of equation (14), the autocorrelation of loading, is

$$S_{LL}(\omega) = B\Omega \sum_{-\infty}^{\infty} F(nB\Omega) G(\omega - nB\Omega) \tag{15}$$

Since in general the Fourier transform of a broad function is a peaked function and vice-versa, $F(\omega)$ which is the Fourier transform of $f(\tau)$ will be a broad function of frequency. Also, $G(\omega)$, the Fourier transform of $g(\tau)$, will be a peaked function. Combining equations (12) and (15) gives for the far-field sound on the rotor axis

$$S_{pp}(\omega) = A\omega^2 B\Omega \sum_{-\infty}^{\infty} F(nB\Omega) G(\omega - nB\Omega) \tag{16}$$

If an acoustic spectrum measured on the axis of a rotor has similarly shaped spectral peaks at harmonics of blade passage frequency, equation (16) can be utilized to derive some of the turbulence characteristics.

The correlation between loading fluctuations on successive blades can be determined from the function $G(\omega)$ whose Fourier transform is the envelope of the autocorrelation as sketched in figure 54(b). Two simple analytic-functions that have the observed exponential decay, and their Fourier transforms, are given by

$$G(\omega) = e^{-(\omega/\omega_0)^2}, \qquad g(\tau) = \sqrt{\pi}\, \omega_0 e^{-(\omega_0 \tau/2)^2} \tag{17}$$

$$G(\omega) = e^{-|\omega|/\omega_0}, \qquad g(\tau) = 2\omega_0 (1 + \omega_0^2 \tau^2)^{-1} \tag{18}$$

The reference frequency ω_0 can be determined by requiring that these assumed spectra reproduce the narrowband peaks in the acoustic spectra of figure 54(a) between roughly 200 and 400 Hz frequency. These show a decrease of about 14 dB over a frequency change of about 8.75 Hz. Blade passing frequency was 28.3 Hz for this two-bladed rotor at 850 rpm rotation speed. The 14 dB change would be given by the first parts of equations (17) and (18) if the reference frequency ω_0 was about 30.6 rad/sec or 1.08/T for equation (17) and about 18.45 rad/sec or 0.603/T for equation (18). Here, T is the time between blade passages (the reciprocal of blade passing frequency). The correlation between the unsteady force on a blade and the force on the following blade a time T later is given by the ratio of $g(\tau)$ evaluated at time T to its value at zero delay time. This ratio is 0.750 for equation (17) and 0.734 for equation (18). Thus the unsteady loading which produced the observed noise shown in figure 54(a) had a strong blade-to-blade correlation. Also, because the autocorrelation functions $g(\tau)$ decayed to about e^{-1} in two blade passage times, the eddies existed within the blade disc for a time not much larger than one rotation.

From the analytical model of the sound PSD as given by equation (16), $G(\omega)$ represents the shape of each particular peak and $\omega^2 F(\omega)$ represents the overall envelope of the peaks. Peak amplitudes obtained from the data of figure 54(a), normalized relative to an average of the maximum peaks, are shown by circle symbols in figure 54(c). To determine a correlation length for the turbulent eddies, two different analytical approximations to the envelope of these peaks were assumed. The simple approximation

$$\omega^2 F(\omega) = (f/400)^2 e^{1-(f/400)^2} \tag{19}$$

is shown in figure 54(c) by a solid line and the lengthier approximation

$$\omega^2 F(\omega) = 0.165(f/100)^2 \cos(0.179 f/100)\, e^{-(0.207 f/100)^2} \tag{20}$$

gives a better match to the high-frequency data and is shown as a dash line. The approximate eddy scale of the flow can be determined by calculating the value of delay time at which the Fourier transforms of these expressions decay by e^{-1}. For both equations (19) and (20), this delay time is about 8.0×10^{-4} sec. The distance traveled by the station at 3/4 blade radius during this time was about 8.1 cm (3.2 in.) which represents the azimuthal distance over which the unsteady blade force can be considered correlated. Because there was zero mean axial flow through the rotor, nothing can be inferred about the turbulence axial length scale.

The inferred turbulent eddy azimuthal length scale of 8 cm (3.1 in.) required to produce the narrowband peaks measured on the rotation axis is about three times the 3 cm (1.2 in.) length scale inferred by regarding the one-third octave spectra as broadband noise. Both types of analysis thus show that the turbulent eddy scale length was of the order of the 5 cm (2 in.) airfoil blade maximum thickness.

CONCLUSIONS AND RECOMMENDATIONS

Noise data were obtained for a nonrotating constant-diameter circular cylinder, constant-chord NACA 0012 airfoil, tapered-diameter cylinder, and tapered-chord airfoils. Available theories, surface pressure measurements, and surface pressure cross-correlations were utilized to predict far-field noise for comparison with data. These calculation methods were then utilized to predict sound spectra on the rotational axis of rotating blades with circular cylinder and with NACA 0012 airfoil sections. On the basis of this analysis, the following conclusions and recommendations were obtained:

1. Noise radiation from nonrotating circular cylinders at transcritical Reynolds numbers depends strongly on surface condition and Reynolds number.

2. Because bluff-body vortex noise from aircraft landing gear wheels and cylindrical struts is likely to be a major component of airframe noise for aircraft during landing approach, it is recommended that noise measurements be obtained for such configurations at close to full-scale Reynolds numbers and compared with current prediction methods.

3. Rotating-blade circular cylinder vortex noise overall sound pressure level, and spectrum shape at frequencies up to the peak frequency, can be predicted using rms lift coefficient and correlation length data for nonrotating cylinders. At higher frequencies, the rotating-blade spectra decay less abruptly than is predicted from nonrotating cylinder data.

4. Blowing the shed wake of rotating cylindrical blades downstream reduces the turbulence level at the blades, slightly increasing the rms lift coefficients and correlation lengths on the blade outboard regions and thereby increasing the vortex noise without greatly changing the spectrum shape.

5. Noise radiation from nonrotating airfoils in low-turbulence flow occurs as very sharp narrowband random peaks. Center frequencies of these peaks are approximately predicted by Tollmein-Schlichting laminar boundary layer instability theory. This noise weakens and disappears as Reynolds number is increased sufficiently to eliminate laminar boundary layers near the trailing edge.

6. Noise radiation from nonrotating airfoils in the turbulent wake shed by an upstream airfoil is about 4 dB weaker than that calculated for airfoils in spatially uniform turbulent flow having the same turbulence properties at the airfoil chord plane.

7. Vortex noise from rotating airfoil-shaped blades with their shed wakes blown downstream have the behavior of airfoil tone noise for blades with rounded tips. Blade rotation increases the maximum Reynolds number at which such noise occurs. Rotating blades with square tips produced stronger high-frequency noise which varied with rotation speed in the manner of bluff-body vortex shedding noise. This noise may have been caused by boundary layer flow being centrifuged off the sharp-edged blade tips.

8. It is recommended that vortex noise from rotating blades with square and rounded tips be measured for blades at nonzero thrust to determine whether the high-frequency noise observed with square-tip blades is altered by formation of the blade tip vortex.

9. On-axis noise from airfoil-shaped blades rotating in their shed wakes is dominated by incidence-fluctuation noise caused by blades slicing through discrete turbulent eddies with length scales of the order of the blade maximum thickness and turbulence levels of the order of half a percent.

REFERENCES

1. Scheiman, J., Hilton, D. A., and Shivers, J. P.: Acoustical Measurements of the Vortex Noise for a Rotating Blade Operating With and Without Its Shed Wake Blown Downstream. NASA TN D-6364, Aug. 1971.

2. Scheiman, J.: Further Analysis of Broadband Noise Measurements for a Rotating Blade Operating With and Without Its Shed Wake Blown Downstream. NASA TN D-7623, Sept. 1974.

3. Phillips, O. M.: The Intensity of Aeolian Tones. J. Fluid Mech., Vol. 1, Part 6, Dec. 1956, pp 607-624.

4. Morse, P. M. and Ingard, K. U.: Theoretical Acoustics. McGraw-Hill Book Co., New York, 1968, pp 750-755.

5. Goldstein, M.: Aeroacoustics. NASA SP-346, 1974, pp 219-230.

6. Gaster, M.: Vortex Shedding from Slender Cones at Low Reynolds Numbers. J. Fluid Mech., Vol. 38, Part 3, Sept. 1969, pp 565-576.

7. Chen, C. F. and Mangione, B. J.: Vortex Shedding from Circular Cylinders in Sheared Flow. AIAA J., Vol. 7, No. 6, June 1969, pp 1211-1212.

8. Stowell, E. Z. and Deming, A. F.: Vortex Noise From Rotating Cylindrical Rods. NACA TN 519, 1935.

9. Yudin, E. Y.: On the Vortex Sound From Rotating Rods. NACA TM 1136, 1947.

10. Paterson, R. W., Vogt, P. G., and Foley, W. M.: Design and Development of the United Aircraft Research Laboratories Acoustic Research Tunnel. J. Aircraft, Vol. 10, No. 7, July 1973, pp 427-433.

11. Paterson, R. W., Vogt, P. G., Fink, M. R., and Munch, C. L.: Vortex Noise of Isolated Airfoils. J. Aircraft, Vol. 10, No. 5, May 1973, pp 296-302.

12. Amiet, R. K.: Correction of Open Jet Wind Tunnel Measurements for Shear Layer Refraction. AIAA Paper 75-532, Mar. 1975.

13. Hardin, J. C., Fratello, D. J., Hayden, R. E., Kadman, Y., and Africk, S.: Prediction of Airframe Noise. NASA TN D-7821, Feb. 1975.

14. Roshko, A.: Experiments on the Flow Past a Circular Cylinder at Very High Reynolds Numbers. J. Fluid Mech., Vol. 10, Part 3, May 1961, pp 345-356.

15. Fung, Y. C.: Fluctuating Lift and Drag Acting on a Cylinder in a Flow at Supercritical Reynolds Numbers. J. Aero. Sci., Vol. 27, No. 11, Nov. 1960, pp 801-814.

16. Schmidt, C. V.: Fluctuating Force Measurements Upon a Circular Cylinder at Reynolds Numbers up to 5×10^6. Meeting on Ground Wind Load Problems in Relation to Launch Vehicles. NASA TM X-57779. June 1966.

17. Loiseau, H. and Szechenyi, E.: Analyse Expérimentale des Portances sur un Cylindre Immobile Soumis a un Écoulement Perpendiculaire a son Axe a des Nombres de Reynolds Élevés. Recherche Aérospatiale, No. 1972-5, Sept.-Oct. 1972, pp 279-291.

18. Batham, J. P.: Pressure Distributions on Circular Cylinders at Critical Reynolds Numbers. J. Fluid Mech., Vol. 57, Part 2, Feb. 1973, pp 209-228.

19. McGregor, D. M.: An Experimental Investigation of the Oscillating Pressures on a Circular Cylinder in a Fluid Stream. U. of Toronto, Inst. of Aerophysics, UTIA Report 14, 1957.

20. Kacker, S. C., Pennington, B., and Hill, R. S.: Fluctuating Lift Coefficient For a Circular Cylinder in Cross Flow. J. Mech. Eng. Science, Vol. 16, No. 9, April 1974, pp 215-224.

21. Baroudi, M. Y.: Measurement of Two Point Correlations of Velocity Near a Circular Cylinder Shedding a Karman Vortex Street. U. of Toronto, Inst. of Aerophysics, UTIA TN 31, 1960.

22. Fink, M. R.: Investigation of Scrubbing and Impingement Noise. NASA CR-134762, Feb. 1975.

23. Filotas, L. T.: Theory of Airfoil Response in a Gusty Atmosphere. Part II - Response to Discrete Gusts or Continuous Turbulence. U. of Toronto, Inst. for Aerospace Studies, UTIAS Report 141, Nov. 1969.

24. Hayden, R. E.: Noise from Interaction of Flow with Rigid Surfaces: A Review of Current Status of Prediction Techniques. NASA CR-2126, Oct. 1972.

25. Hinze, J. O.: Turbulence. McGraw-Hill Book Co., Inc., New York, 1959.

26. Fink, M. R.: Prediction of Airfoil Tone Frequencies. J. Aircraft, Vol. 12, No. 2, Feb. 1975, pp 118-120.

27. Erens, P. J. and Chasteau, V. A. L.: Laminar Boundary Layer Response to Free-stream Disturbances. AIAA J., Vol. 12, No. 1, Jan. 1974, pp 93-94.

28. Shen, S. F.: Calculated Amplitude Oscillations in the Plane Poissuille and Blasius Flows. J. Aero. Sci., Vol. 21, No. 1, Jan. 1954, pp 62-64.

29. Paterson, R. W., Vogt, P. G., Fink, M. R., and Munch, C. L.: Vortex Shedding Noise of an Isolated Airfoil. United Aircraft Research Laboratories Report K910867-6, Dec. 1971.

30. Lowson, M. V., Whatmore, A. R., and Whitfield, C. E.: Source Mechanisms for Rotor Noise Radiation. NASA CR-2077, Aug. 1973.

31. Wright, S. E.: Discrete Radiation From Rotating Periodic Sources. J. Sound & Vib., Vol. 17, No. 4, Aug. 22, 1971, pp 437-498.

32. Hosier, R. N. and Ramakrishnan, R.: Helicopter Rotor Rotational Noise Predictions Based on Measured High-Frequency Blade Loads. NASA TN D-7624, Dec. 1974.

33. Hanson, D. B.: Spectrum of Rotor Noise Caused by Atmospheric Turbulence. J. Acoust. Soc. Am., Vol. 56, No. 1, July 1974, pp 110-126.

34. Amiet, R. K.: Tone Prediction by Coherence Between Blade to Blade Rotor Forces. United Aircraft Research Laboratories Report UAR-N65, April 1974.

35. Gerrard, J. H.: Measurements of the Sound from Circular Cylinders in an Air Stream. Proc. Phys. Soc. London, Section B, Vol. 68, Part 7, July 1955, pp 453-461.

APPENDIX A: STRIP THEORY FOR VORTEX NOISE

Vortex noise of circular cylinders in uniform flow was analyzed by Phillips (ref. 3) for very low subsonic flow velocities. A rigorous analysis that includes subsonic convection effects is given in Section 3.5.1.2 of reference 5. That solution should be directly applicable to vortex noise from any surface which is acoustically compact along the chord. Lift force fluctuation was assumed to have the same simple-harmonic frequency and amplitude everywhere along the span but to vary randomly in spanwise phase. Equivalently, one could regard the lift force fluctuation at all spanwise locations as having the same sharply peaked narrowband-random spectrum when averaged over many periods of oscillation. Cross-correlations taken over times of the order of a period might show that lift forces per unit span were different in frequency and amplitude in addition to phase. Effects of spanwise nonuniformity in geometry and relative velocity are examined below while maintaining the description of constant lift force spectrum but randomly varying spanwise phase. Nomenclature is that of reference 5 except that subscript and superscript zeros which denoted free-stream quantities have been omitted except for the speed of sound. Far-field density fluctuation per unit length of cylinder was given by equation (3-89) of reference 5. The density fluctuation produced in the far field by the force fluctuation along the entire cylinder was given by equation (3-91). That equation can be modified for spanwise nonuniformity by moving all quantities which might vary, such as rms lift coefficient K, Strouhal number St, relative velocity V, and relative Mach number M, under the integral sign. Then from equation (3-94) the far-field acoustic intensity $\bar{I} = \overline{p^2}/\rho c_0$ is

$$\bar{I} = \frac{\rho \sin^2\theta \cos^2\phi}{32\, c_0^3 R^2} \int_{-b/2}^{b/2} \exp\left[i(\omega/c_0)\xi \sin\theta \sin\phi\right] \int_{-(b/2)-\zeta_3}^{(b/2)-\zeta_3} \frac{K^2 St^2 V^6}{(1-M\cos\theta)^4} \exp\left\{i\left[\Phi(\zeta_3-\xi)-\Phi(\zeta_3)\right]\right\} d\xi\, d\zeta_3 \tag{A1}$$

Here the coordinate system is centered at midspan with ζ_3 measured spanwise. The azimuth angle θ, sideline angle ϕ, and other geometric quantities are sketched below, and ξ is a spanwise distance.

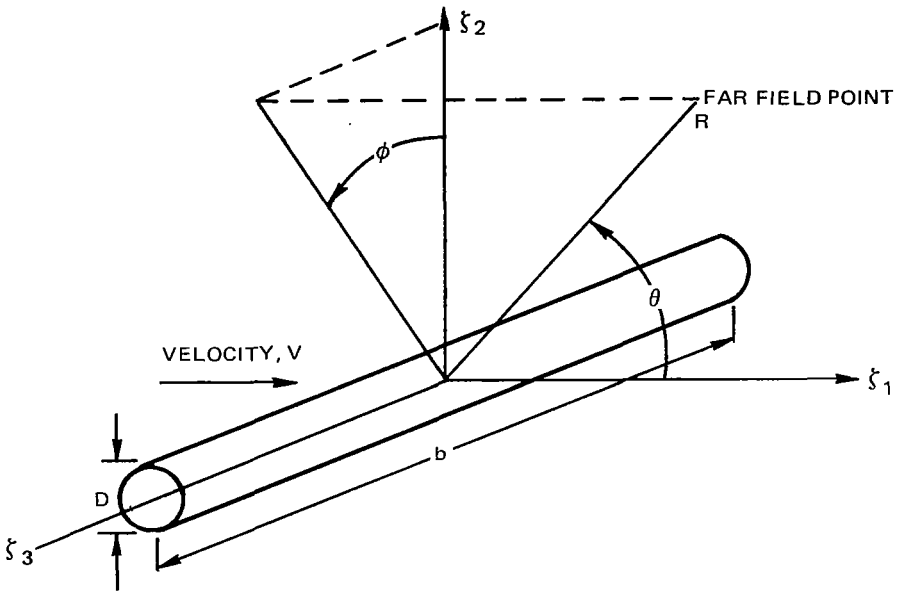

If the geometry and flow field had no spanwise variation and if the vortex shedding process was highly coherent along the span, the phase angle Φ would be constant along the span. Then the second exponential in equation (A1) would be equal to unity. If the argument of the first exponential is small compared with unity, either because the Mach number is very small or because the sideline angle is small, the first exponential would also be unity. Then for a lift force fluctuation that is highly coherent along the span as can occur with small, slightly vibrating wires, equation (3-93) of reference 5 is obtained.

$$\bar{I} = \frac{K^2 St^2 b^2 \rho V^6 \sin^2\theta \cos^2\phi}{32 c_0^3 R^2 (1 - M\cos\theta)^4} \tag{A2}$$

The form of this equation was verified experimentally by Gerrard (ref. 35) who found that acoustic intensity varied with length squared and was independent of diameter for cylindrical wires at Reynolds numbers near 6000.

The analysis within reference 5 was concerned with constant-diameter cylinders for which rms lift coefficient had constant amplitude and constant spectrum shape along the span. Only the phase angle at each frequency was assumed to vary with spanwise position. If the spectrum of lift coefficient was narrowband-random rather than concentrated at one frequency, the analysis would be changed only in that acoustic intensity, lift coefficient, and correlation length would have to be expressed as power spectral densities.

However, problems of interest for this study include spanwise variations of local lift coefficient spectrum in addition to phase angle. The narrowband correlation coefficient is assumed to be Gaussian as in reference 5 but the lift coefficient at each frequency is assumed given by its constant-diameter value for only a correlation length ℓ_y and to be zero elsewhere. Diameter and relative velocity are assumed constant over a phase correlation length ℓ. Then,

$$\int_{-b/2-\zeta_3}^{b/2-\zeta_3} \frac{f^2D^2V^4K^2(f)}{(1-M\cos\theta)^4} \exp\left\{i\left[\Phi(\zeta_3-\xi)-\Phi(\zeta_3)\right]\right\} d\xi_3 = \frac{f^2D^2V^2K^2(f)}{(1-M\cos\theta)^4}\ell_y \exp(-\xi^2/2\ell^2) \tag{A3}$$

$$\bar{I}(f)=\frac{\rho f^2\sin^2\theta\cos^2\phi}{32\,c_0^3R^2}\int_{-b/2}^{b/2}\frac{D^2V^4K^2(f)\ell_y(f)}{(1-M\cos\theta)^4}\exp\left[i(\omega/c_0)\xi\,\sin\theta\sin\phi-(\xi^2/2\ell^2)\right]d\xi \tag{A4}$$

If the phase correlation length ℓ is small compared with the cylinder length, the limits of the remaining integral in equation (A1) can be extended to plus and minus infinity. For constant geometry and velocity, equation (A4) can then be integrated to yield

$$\bar{I}=\frac{\sqrt{2\pi}K^2St^2\ell\ell_y\rho V^2\sin^2\theta\cos^2\phi}{32\,c_0^3R^2(1-M\cos\theta)^4}\exp\left[-\frac{1}{2}(\omega\ell/c_0)^2\sin^2\theta\sin^2\phi\right] \tag{A5}$$

This equation would be identical to equation (3-95) of reference 5 if the lift coefficient correlation distance ℓ_y is taken equal to the span. For practical calculations involving nonuniform geometry and flow, it is convenient to consider only those measurement directions for which the sideline angle is approximately zero. Then equation (A4) becomes

$$\bar{I}(f)=\frac{\rho f^2\sin^2\theta}{32\,c^3R^2}\int_{-b/2}^{b/2}\frac{D^2V^4K^2(f)\ell_y(f)}{(1-M\cos\theta)^4}\exp(-\xi^2/2\ell^2)d\xi \tag{A6}$$

which is the key equation for vortex noise calculation.

The Gaussian spanwise decay assumed in references 3 and 5 is not necessarily a good approximation for Reynolds numbers of interest. It was shown in figure 12 of reference 20 to give a close prediction of the spanwise decay of correlation coefficient for a circular cylinder at a Reynolds number of 53,500. However, correlation coefficients shown in figure 19 of reference 17 had a more rapid initial decay and a less rapid fall-off at large distances. Those data for Reynolds numbers from 260,000 to 5,500,000 were closely matched by an exponential decay, $\exp(-|\xi|/\ell)$. Then the term $(-\xi^2/2\ell^2)$ in equations (A3), (A4), and (A6) would be replaced by $(-|\xi|/\ell)$ and the factor $\sqrt{2\pi}\ell$ in equation (A5) would become 2ℓ. This result is conceptually appealing because correlation length ℓ is defined for correlations extending in only one spanwise direction. If this correlation length was half the cylinder length, lift fluctuations would be correlated over the entire span and equation (A5) modified for exponential decay would reduce to equation (A2).

This analysis gives no obvious way to predict or even define precisely the distance ℓ_y for which the power spectral density of lift force fluctuation has significant content at a given frequency. For a constant-diameter cylinder, this distance is equal to the entire span. It is smaller than the span of a tapered nonrotating or constant-diameter rotating cylinder, with a lower limit equal to twice the phase correlation length. The data presented herein for a 2:1 tapered cylinder were utilized for comparing these two experimentally determined lengths.

APPENDIX B: RELATION BETWEEN CYLINDER SURFACE PRESSURE FLUCTUATION AND LIFT COEFFICIENT FLUCTUATION

Consider the pressure distribution on a lifting circular cylinder in incompressible inviscid flow. From the unsteady Bernoulli equation,

$$-d\phi/dt+\frac{1}{2}q^2+p/\rho = \text{constant} \tag{B1}$$

where ϕ is the potential function and q is the resultant velocity. Far upstream, the flow is steady with velocity V and pressure p_∞ . Then the spatially and time-varying static pressure is obtained from equation (B1) as

$$p(t)=p_\infty+\frac{1}{2}\rho(V^2-q^2)+\rho d\phi/dt \tag{B2}$$

On the surface of a solid cylinder of diameter D, the local velocity must be parallel to the surface

$$p(D/2,\theta,t)=p_\infty+\frac{1}{2}\rho V^2-\frac{1}{2}\rho V_\theta^2(D/2,\theta,t)+\rho d\phi/dt\,|_{D/2,\theta,t} \tag{B3}$$

For the sum of uniform flow about a cylinder and sinusoidally fluctuating circulation about a cylinder,

$$\phi(t)=-(\Gamma/2\pi)(\theta-\frac{\pi}{2})\cos\omega t+V\sin\theta(r+D^2/4r) \tag{B4}$$

$$V_\theta(D/2,\theta,t)=(\Gamma/\pi D)\cos\omega t+2V\cos\theta \tag{B5}$$

If there is no circulation, the radial component of velocity at the circle is zero and the angular component is given by $2V\cos\theta$ where θ is the angle from

upstream. Denoting the spatially varying pressure for this case by p', equation (B1) becomes

$$p'(D/2,\theta)=p_\infty+\frac{1}{2}\rho V^2-2\rho V^2\cos^2\theta \tag{B6}$$

A transducer that measures surface pressure fluctuations would measure the difference between p and p'. This quantity can be obtained from equations (B3) through (B6).

$$\Delta p(D/2,\theta,t)=p-p'=\frac{1}{2}\rho\left[V^2-V_\theta^2(t)\right]+\rho\, d\phi/dt\,|_{D/2,\theta,t} \tag{B7}$$

$$\Delta p(D/2,\theta,t)=\frac{1}{2}\rho\left[-\frac{4V\Gamma}{\pi D}\cos\theta\cos\omega t-\left(\frac{\Gamma}{\pi D}\right)^2\cos^2\omega t+\frac{\Gamma}{\pi}\left(\theta-\frac{\pi}{2}\right)\omega\sin\omega t\right] \tag{B8}$$

The measured quantity is actually the time average of this pressure difference squared.

$$\overline{\Delta p^2}=\frac{1}{T}\int_0^T(\Delta p)^2dt=\frac{1}{2}\left(\frac{2\Gamma}{DV}\right)^2\left[\left(\frac{\rho V^2}{\pi}\cos\theta\right)^2+\left(\frac{\theta-\pi/2}{2\pi}\rho V D\omega\right)^2+3\left(\frac{\Gamma}{DV}\right)^2\left(\frac{1}{2}\rho V^2\right)^2(2\pi)^{-2}\right] \tag{B9}$$

Usually, the third term within the square brackets is much smaller than the other two terms. Maximum normalized circulation $2\Gamma/DV$, which is equal to maximum fluctuating lift coefficient per unit span, then can easily be determined from measured values of mean square surface pressure fluctuation by neglecting that term. Mean square lift coefficient per unit span is given by

$$\overline{C_L^2}=\overline{L^2}/\left(\frac{1}{2}\rho V^2D\right)^2=2(\Gamma/DV)^2 \tag{B10}$$

$$\overline{C_L^2} = \left[\overline{\Delta p^2}/\left(\tfrac{1}{2}\rho V^2\right)^2\right]\left\{\left(\frac{2}{\pi}\cos\theta\right)^2 + \left[\left(\frac{\theta}{\pi} - \frac{1}{2}\right)\frac{\omega D}{V}\right]^2\right\}^{-1} \qquad \text{(B11)}$$

Thus the rms lift coefficient spectrum per unit span and therefore the fluctuating lift force spectrum required for calculating dipole sound radiation can be determined from the measured variation of surface pressure amplitude with frequency, evaluated at one angular position on the cylinder.

TABLE I

Description	f(kHz)	ℓ_y/c_{min}	$10 \log(S_{QQ}/S_{PP})$ Measured	$10 \log(S_{QQ}/S_{PP})$ Predicted	C_{min}, cm	ℓ_y, cm
$\alpha = 0^\circ$	1.77	0.75	45.2	44.3	11.4	8.6
Constant chord	2.06	0.75	52.0	44.3	11.4	8.6
$\alpha = -4^\circ$	3.42	0.75	40.5	44.3	11.4	8.6
Constant chord	4.17	0.75	36	44.3	11.4	8.6
2:1 Taper	4.52	0.75	48.6	47.9	7.6	5.7
$\alpha = -4^\circ$	4.98	0.75	54.5	47.9	7.6	5.7
4:1 Taper $\alpha = 2^\circ$	5.65	1.5	53	46.2	4.6	6.9

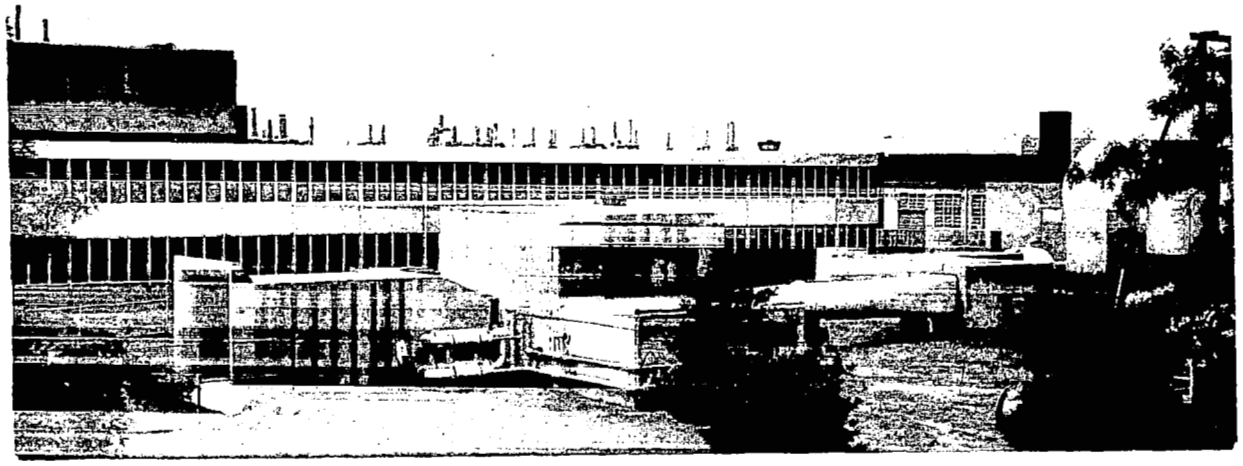

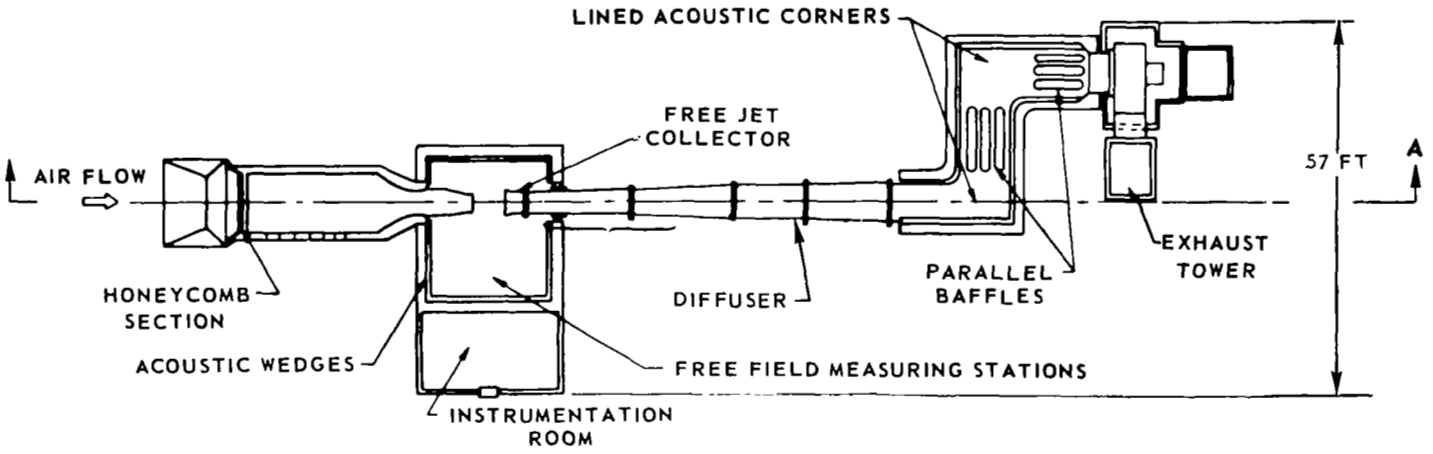

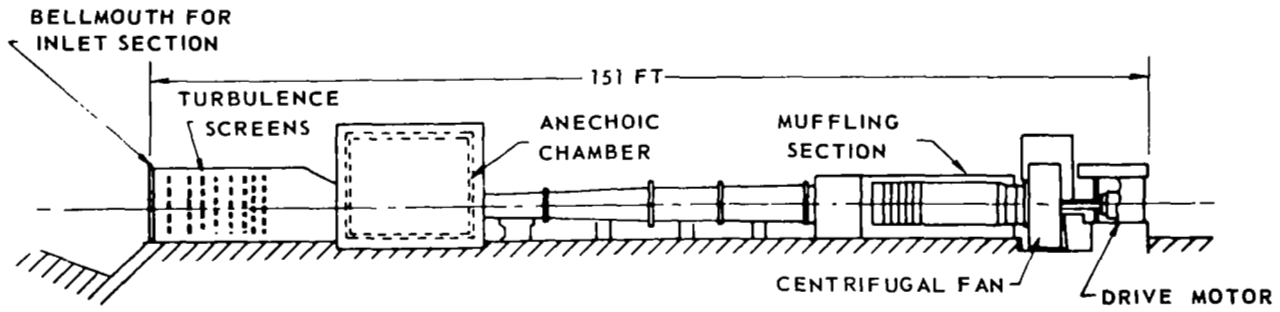

PARTIAL SECTION A–A

FIGURE 1. – UTRC ACOUSTIC RESEARCH TUNNEL

1/8 SCALE, ALL DIMENSIONS IN CENTIMETERS

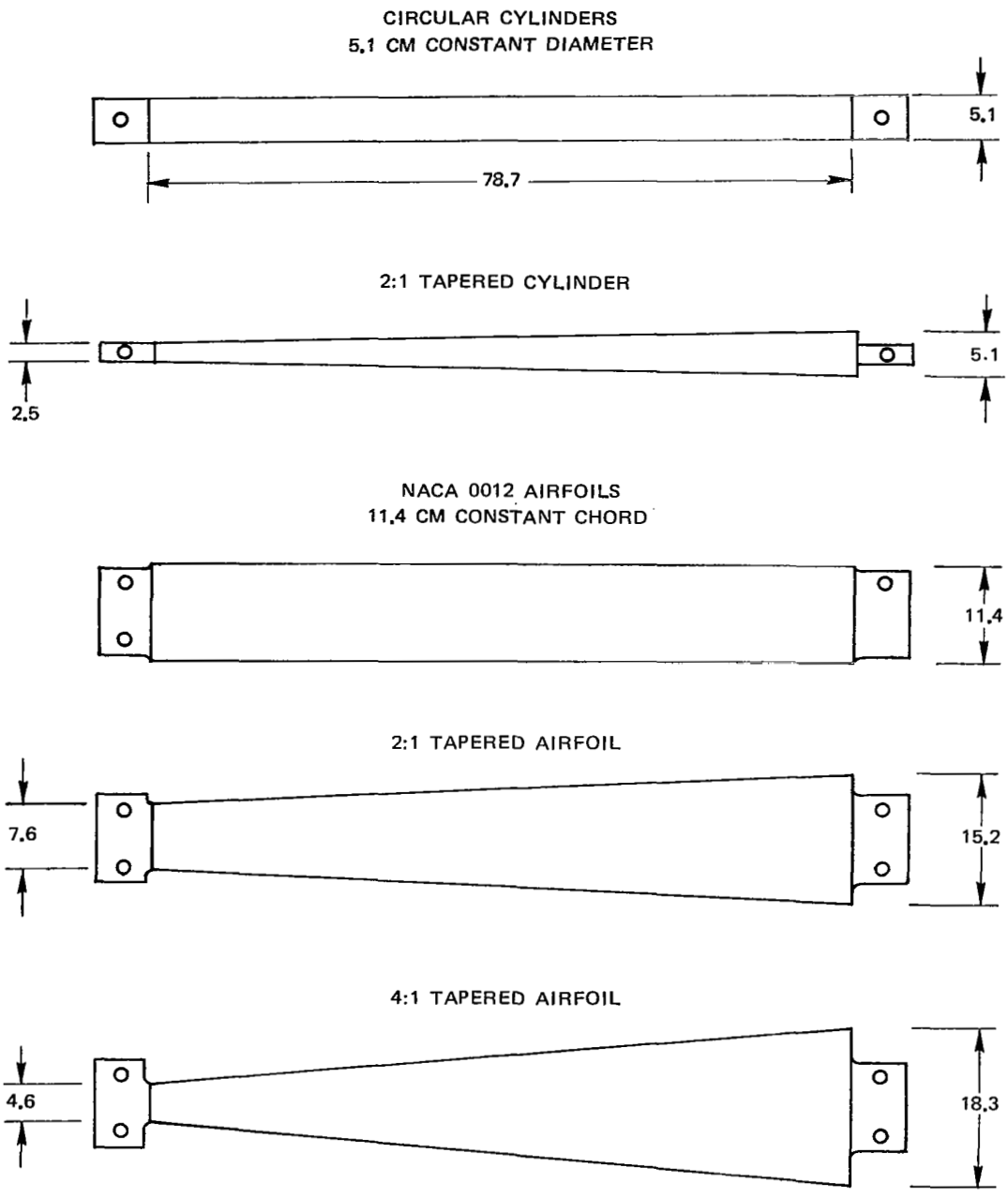

FIGURE 2. – SKETCH OF NONROTATING AIRFOIL MODELS

CONSTANT CHORD

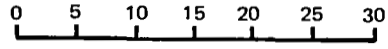

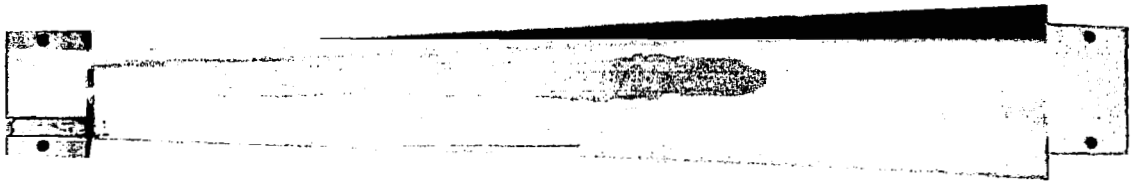

2:1 TAPER RATIO

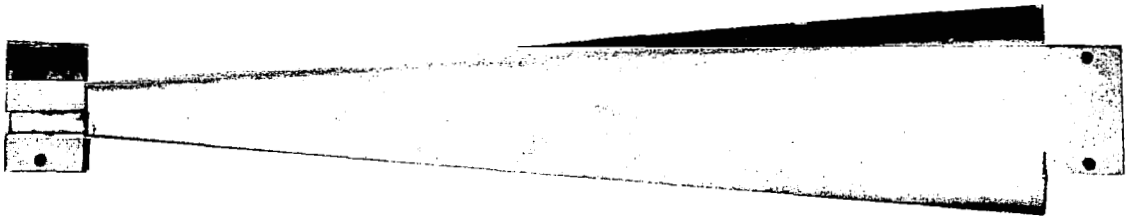

4:1 TAPER RATIO

FIGURE 3 – NACA 0012 NONROTATING AIRFOIL MODELS

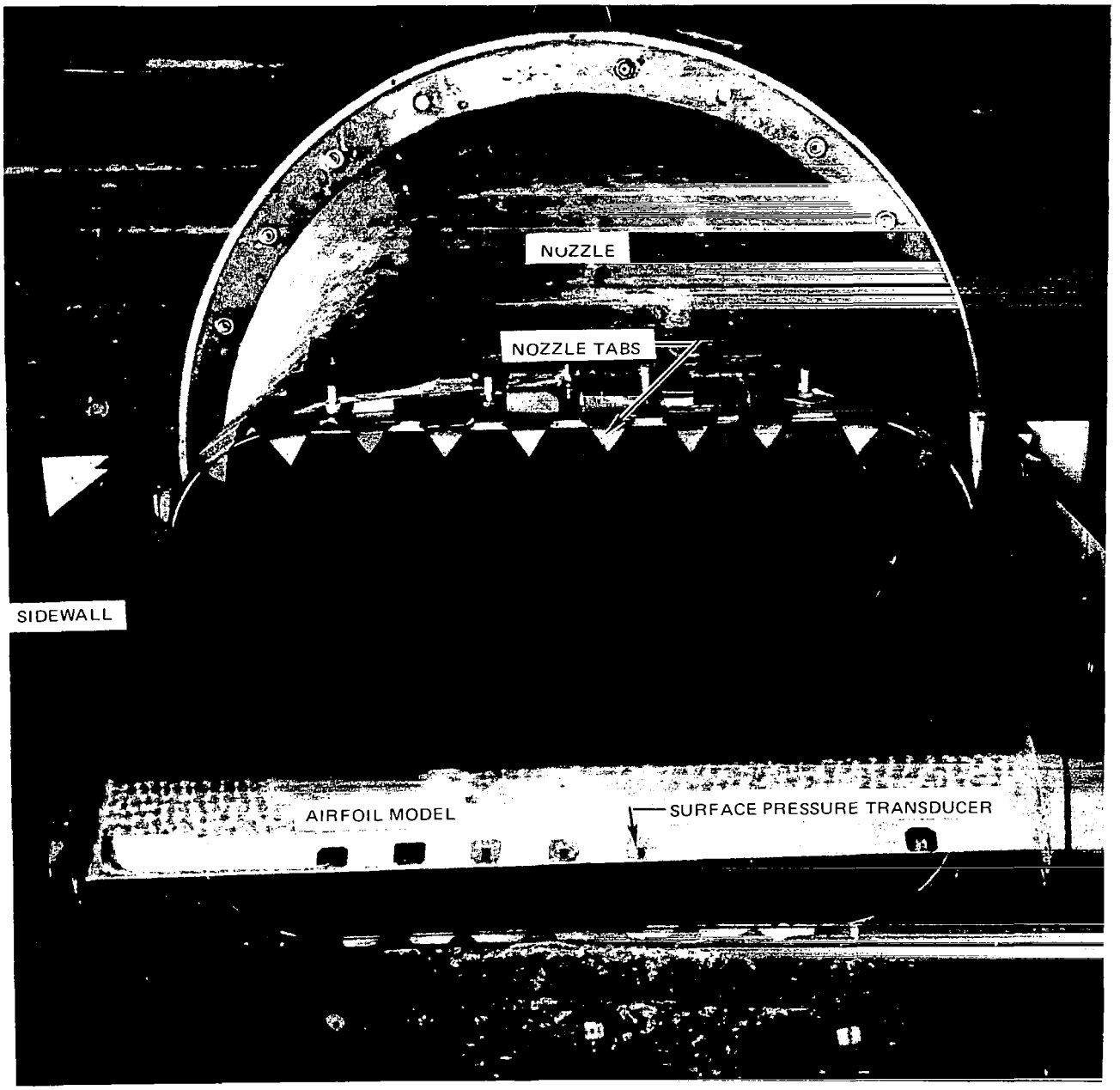

FIGURE 4 – INSTALLATION OF SURFACE PRESSURE TRANSDUCERS ALONG TRAILING EDGE OF CONSTANT–CHORD AIRFOIL MODEL

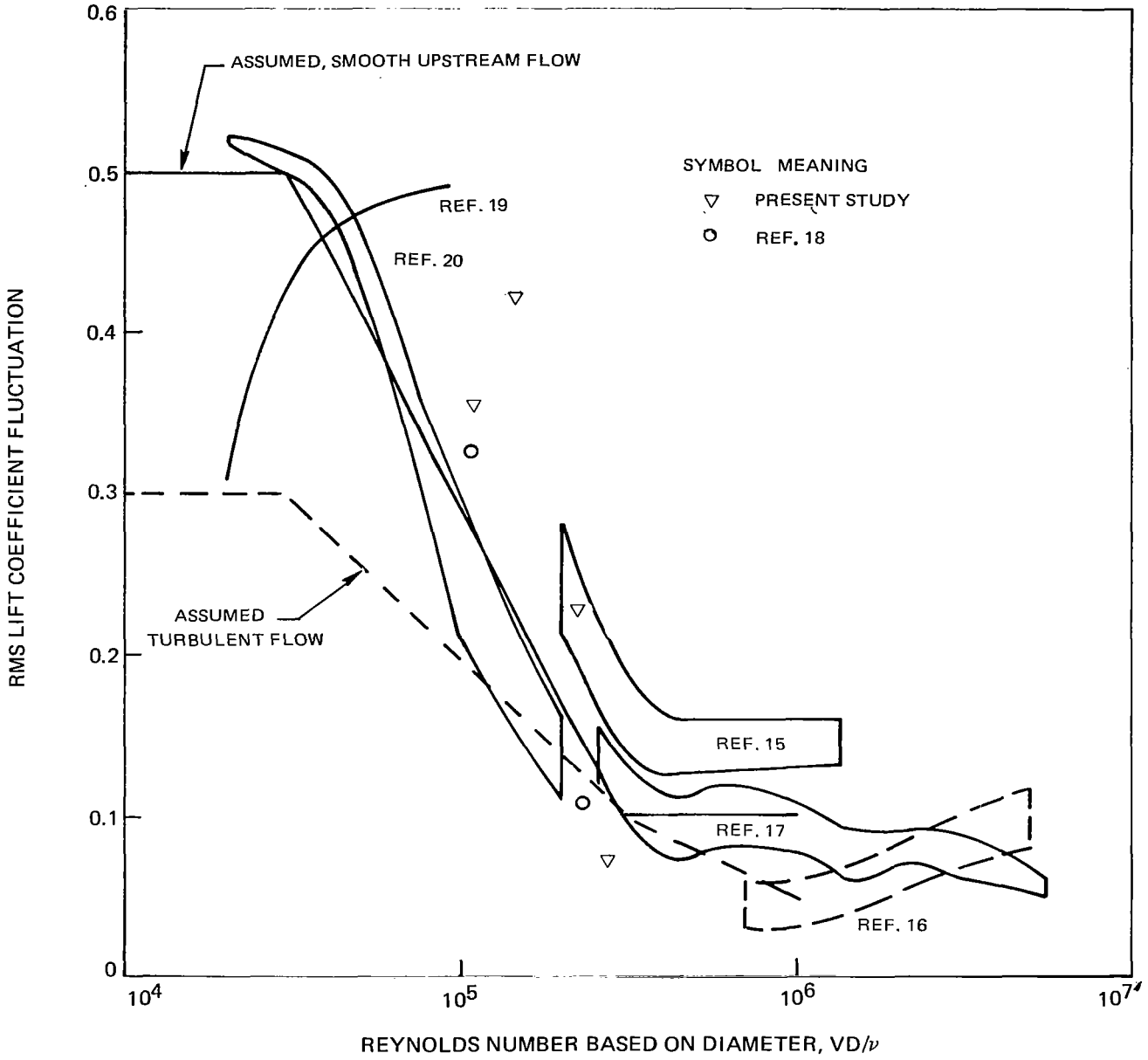

FIGURE 5– VARIATION OF RMS LIFT COEFFICIENT WITH REYNOLDS NUMBER FOR SMOOTH CIRCULAR CYLINDERS

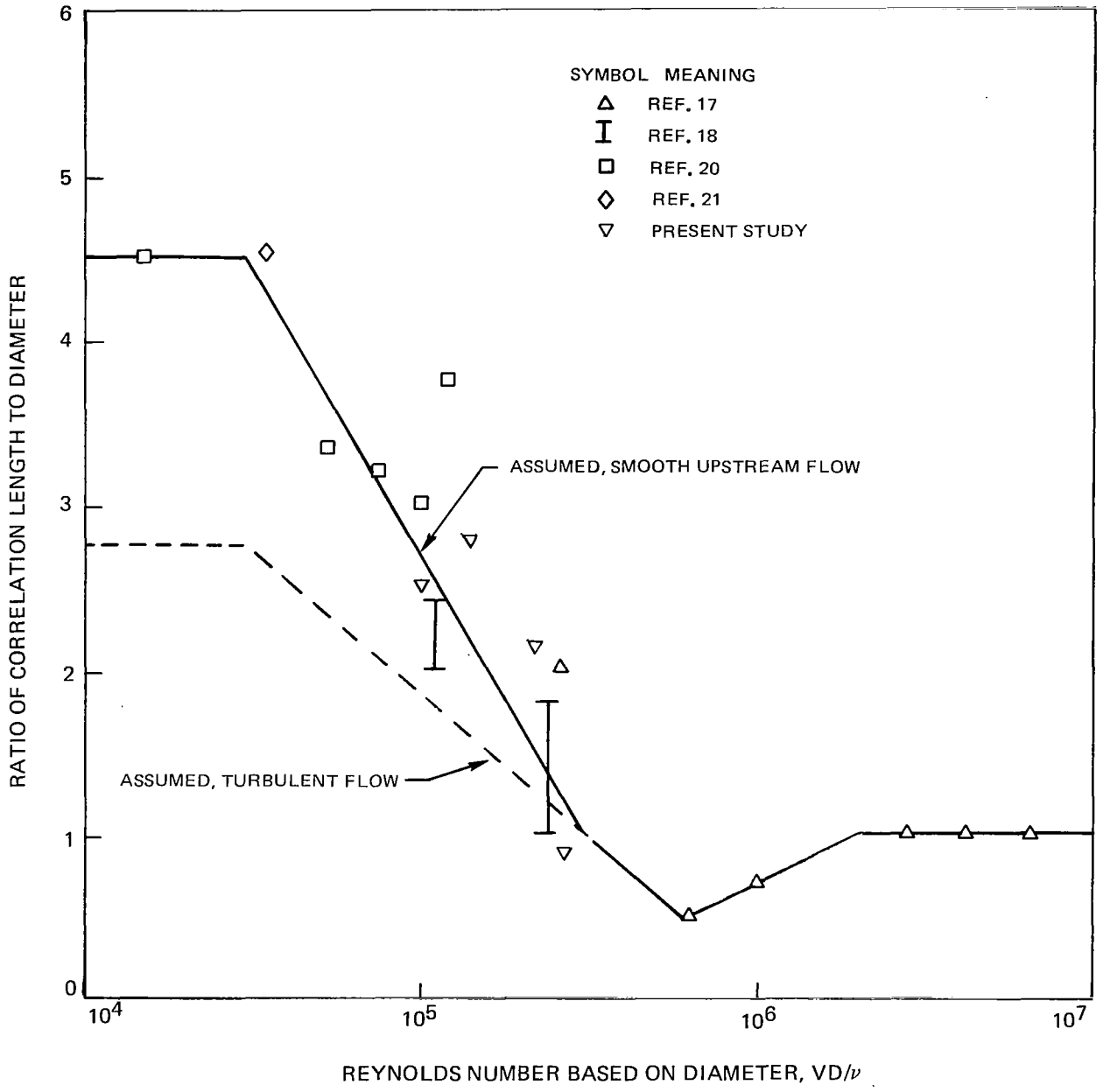

FIGURE 6 – VARIATION OF CORRELATION LENGTH WITH REYNOLDS NUMBER FOR SMOOTH CIRCULAR CYLINDERS

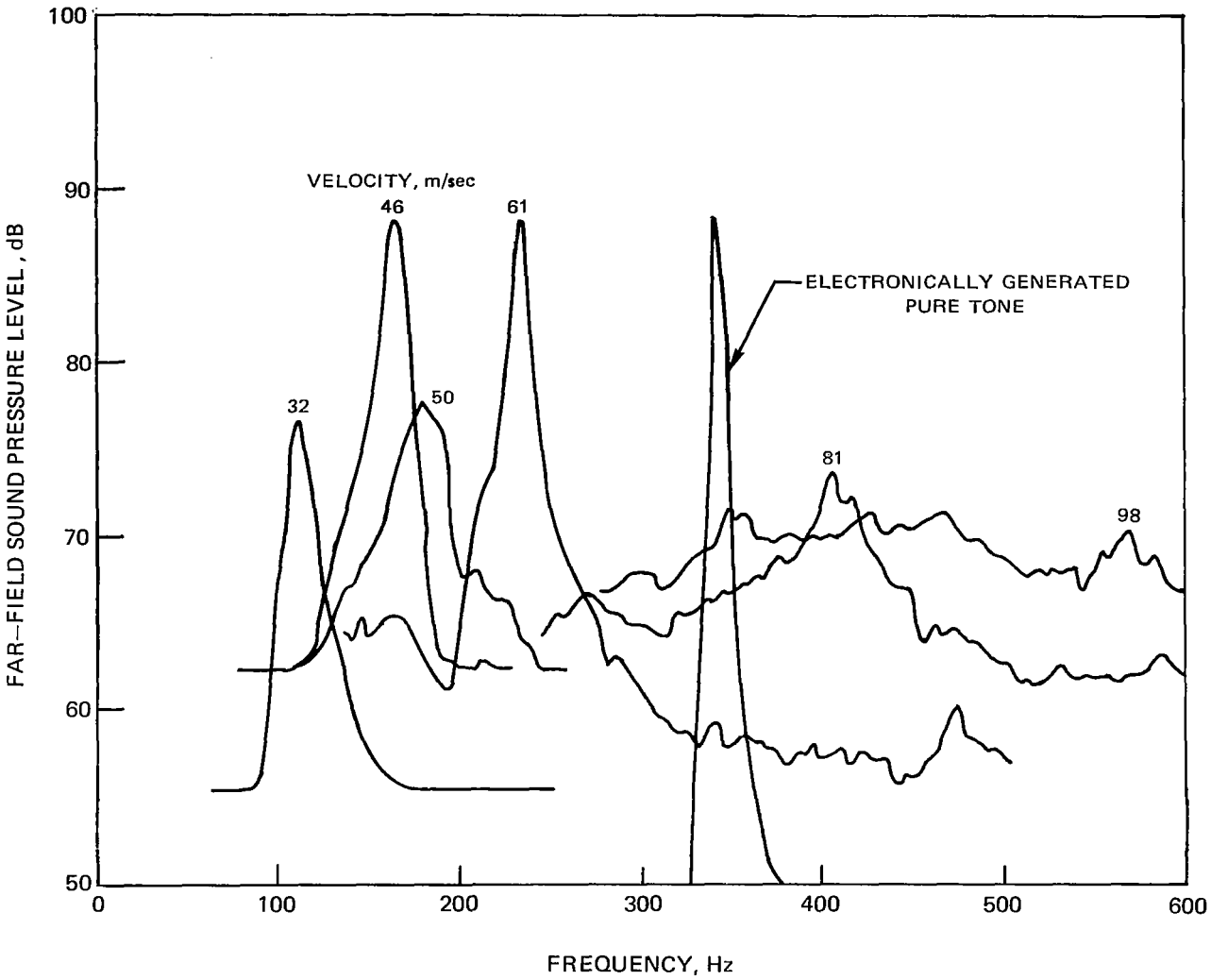

FIGURE 7 – VARIATION OF SOUND PRESSURE SPECTRUM WITH VELOCITY FOR A 5.08 CM CONSTANT–DIAMETER CYLINDER NO UPSTREAM TURBULENCE GENERATOR.

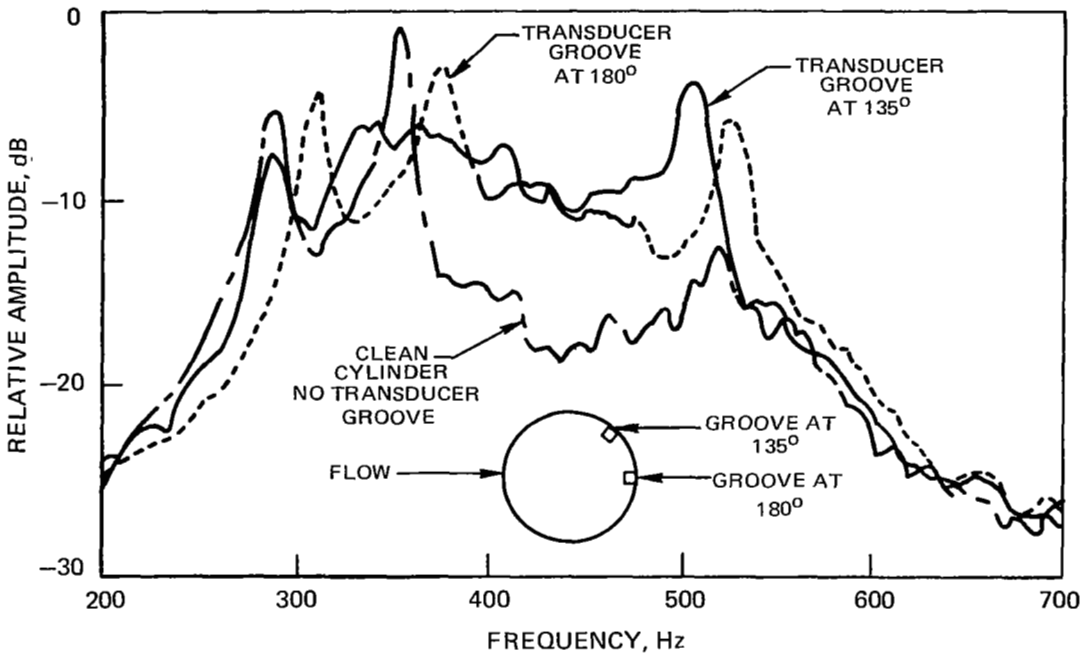

FIGURE 8 – VARIATION OF SOUND PRESSURE SPECTRUM WITH ANGULAR POSITION OF TRANSDUCER GROOVE ON THE 2:1 TAPERED CYLINDER, NO UPSTREAM TURBULENCE GENERATOR.

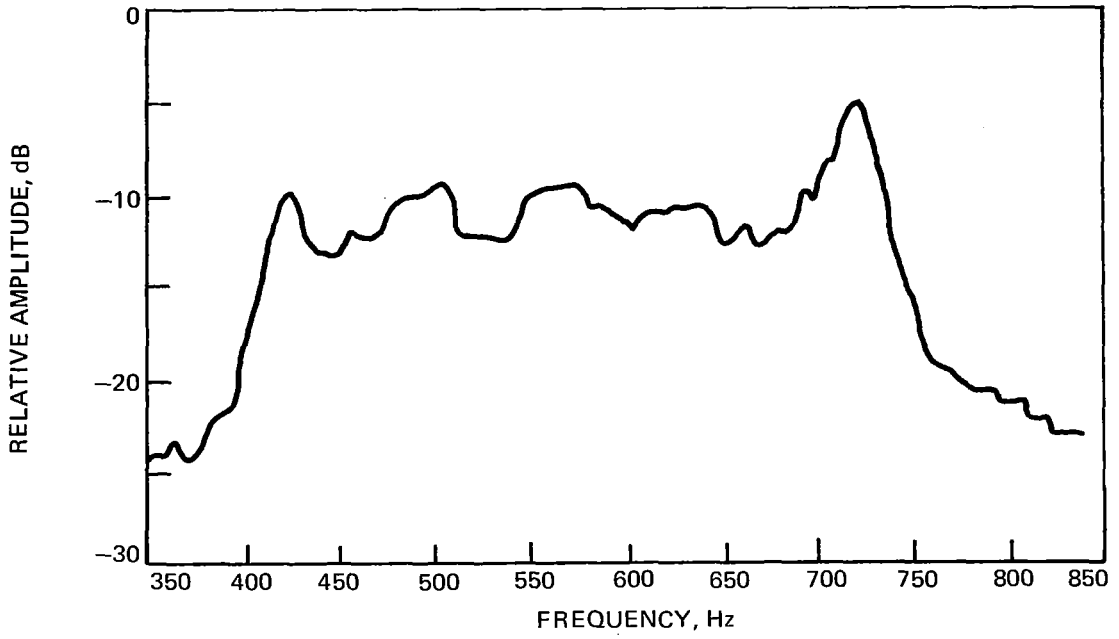

a) SHORTLY AFTER STARTING TUNNEL

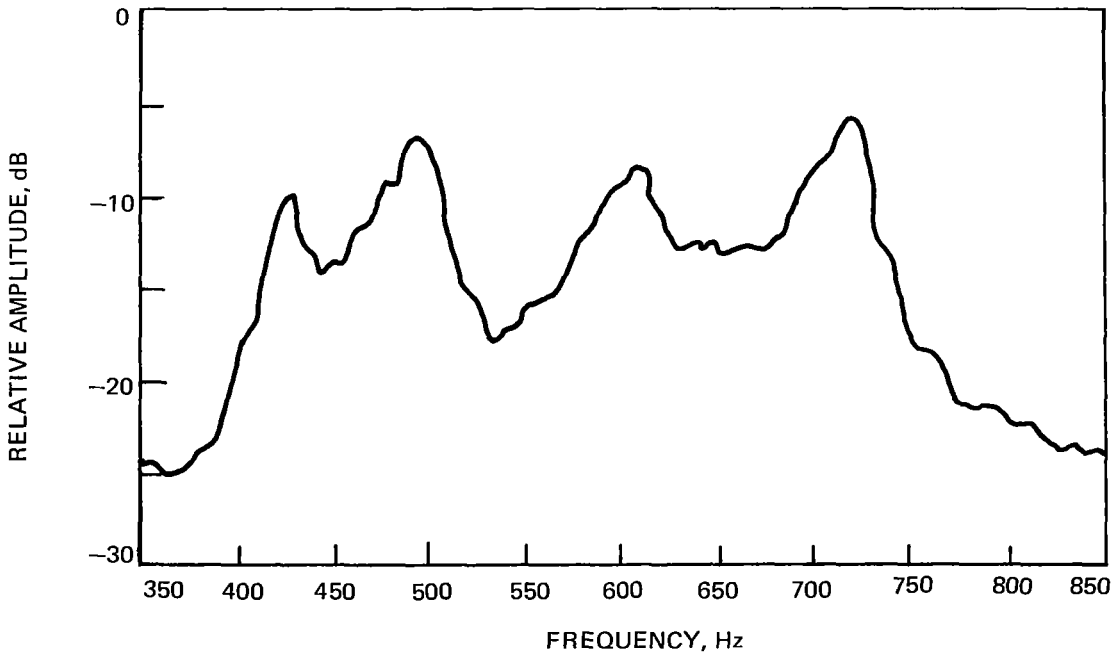

b) SEVERAL MINUTES LATER

FIGURE 9— VARIATION OF SOUND PRESSURE SPECTRUM WITH TIME FOR THE 2:1 TAPERED CYLINDER, NO UPSTREAM TURBULENCE GENERATOR

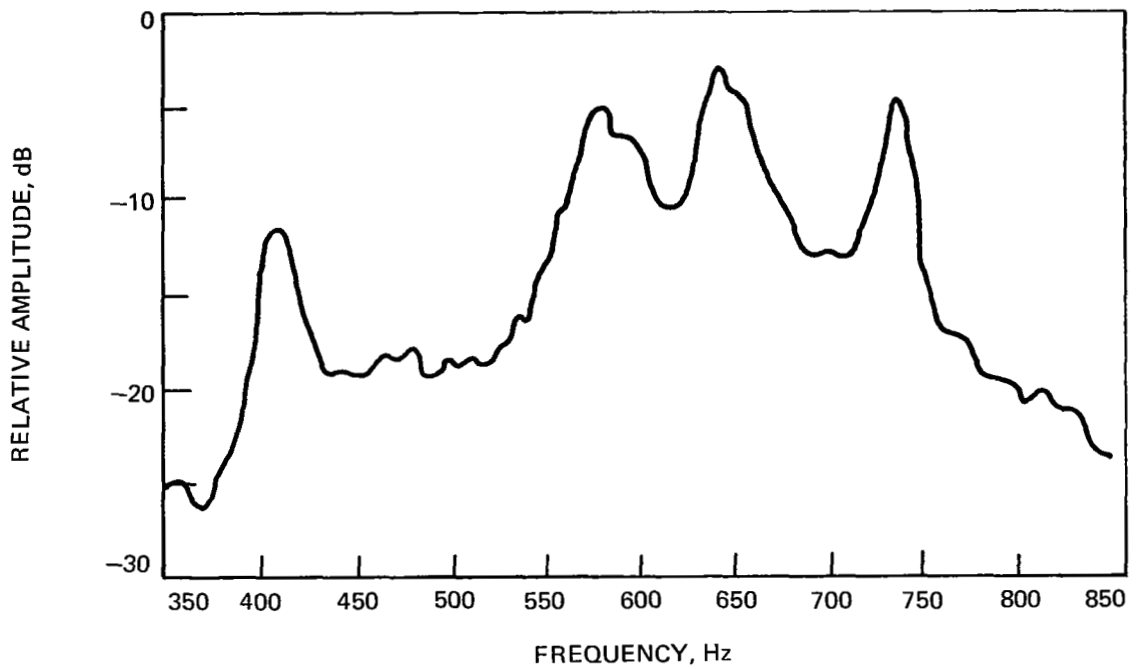

c) ATTEMPTED REPAIR OF SECOND SPECTRUM

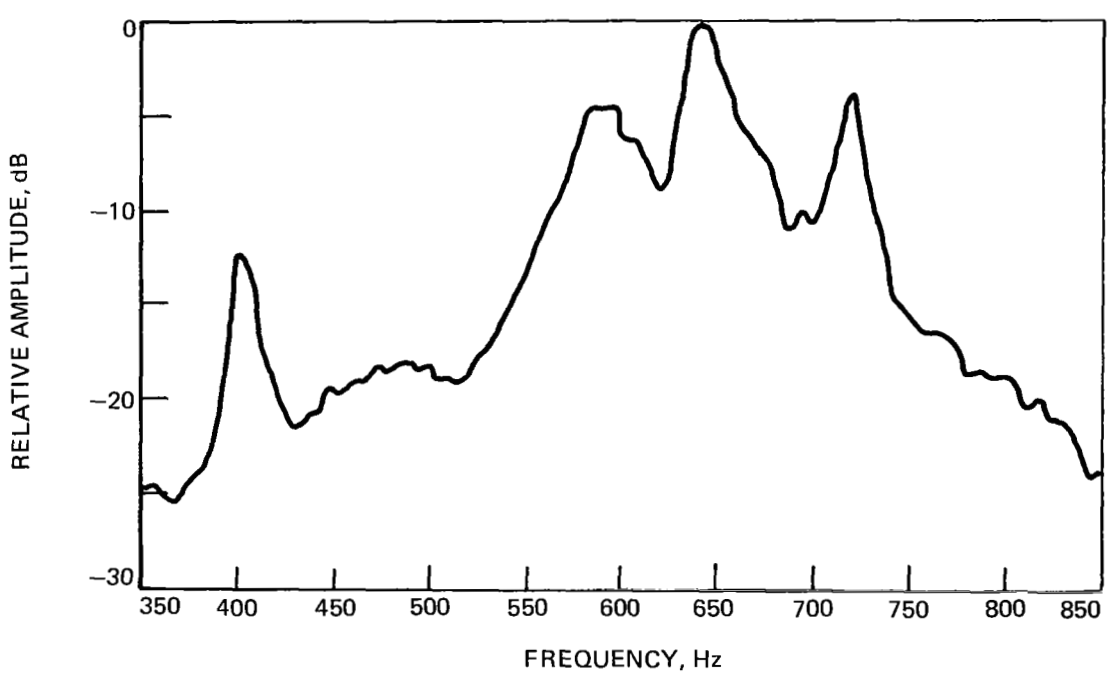

d) SPECTRUM PRIOR TO TUNNEL SHUT DOWN

FIGURE 9 – CONCLUDED

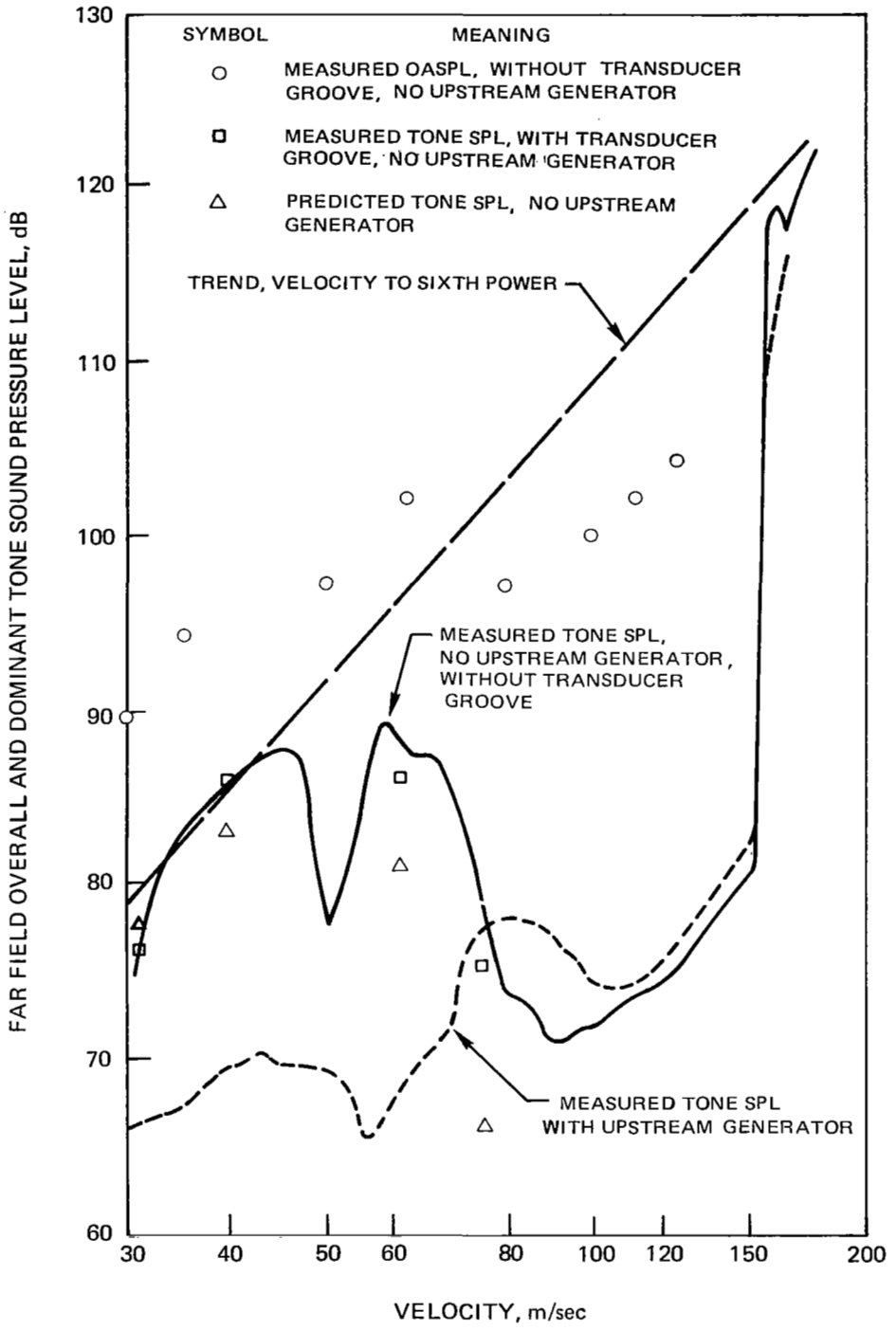

FIGURE 10– VARIATION OF OVERALL AND DOMINANT TONE SOUND PRESSURE LEVEL, WITH VELOCITY FOR CONSTANT DIAMETER CYLINDER, WITH AND WITHOUT UPSTREAM GENERATOR.

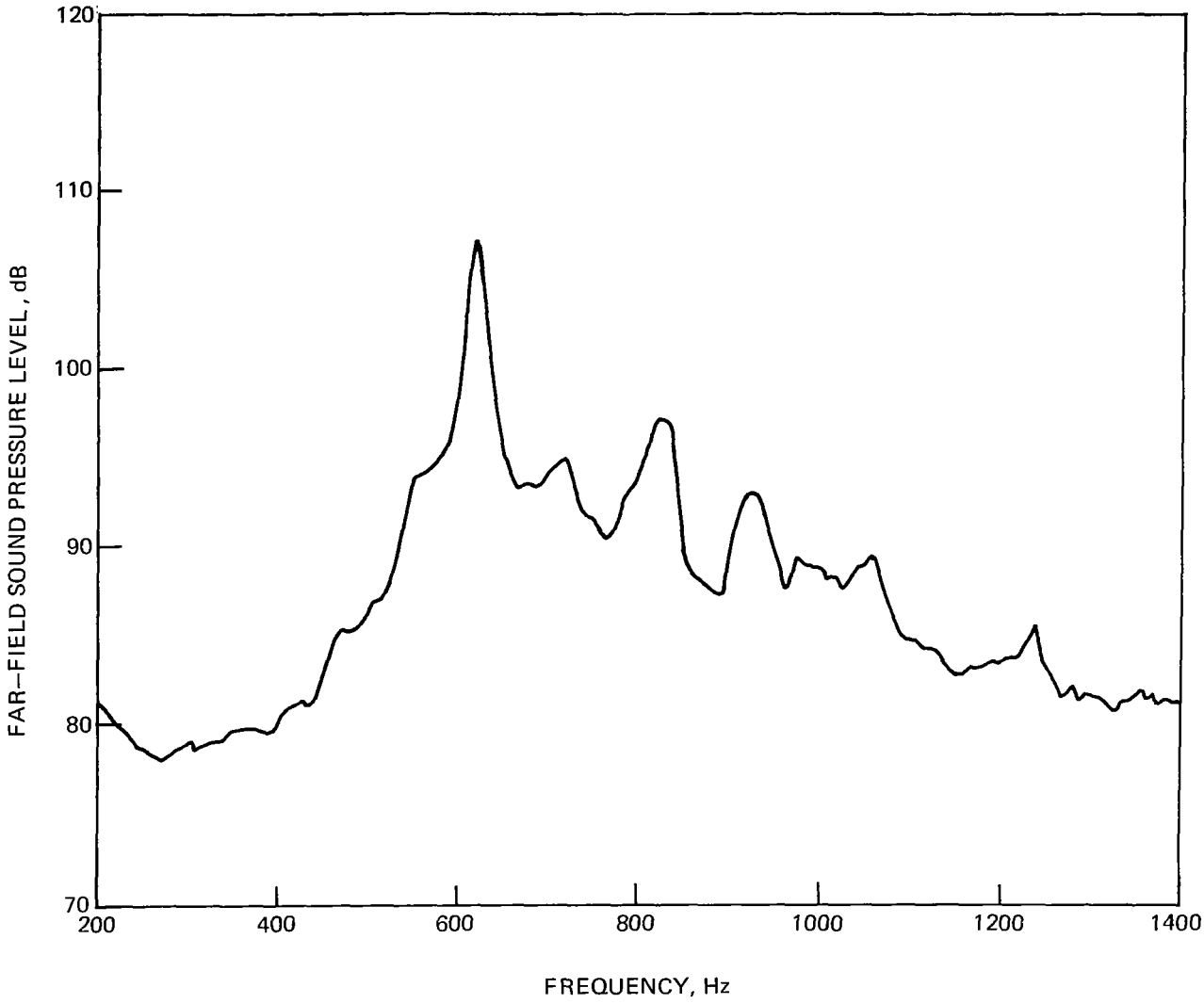

FIGURE 11 – SOUND PRESSURE SPECTRUM OF 2:1 TAPERED CYLINDER AT 159 m/sec (520 ft/sec) VELOCITY. REYNOLDS NUMBER 550,000 BASED ON MAXIMUM DIAMETER . NO UPSTREAM GENERATOR.

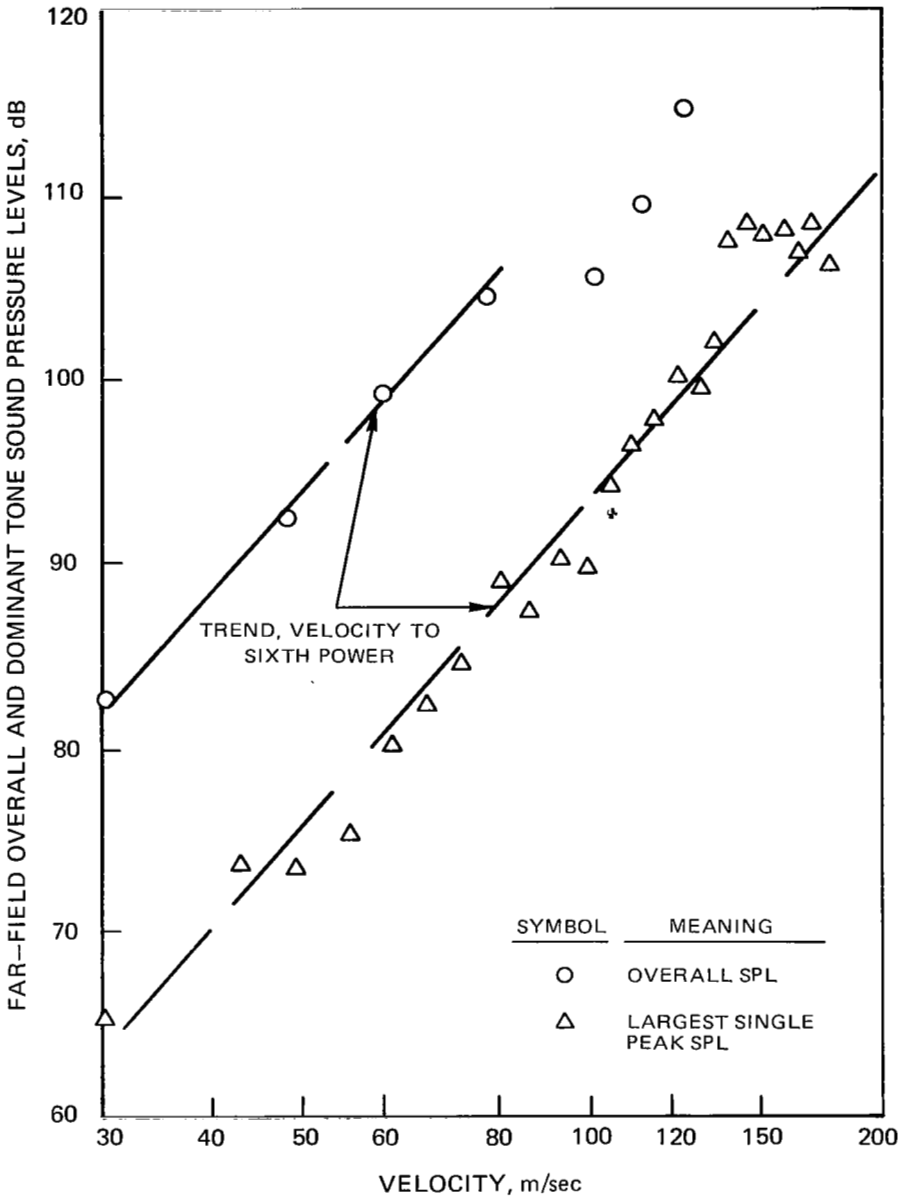

FIGURE 12– VARIATION OF OVERALL SOUND PRESSURE LEVEL, AND DOMINANT TONE SOUND PRESSURE LEVEL, WITH VELOCITY FOR 2:1 TAPERED CYLINDER

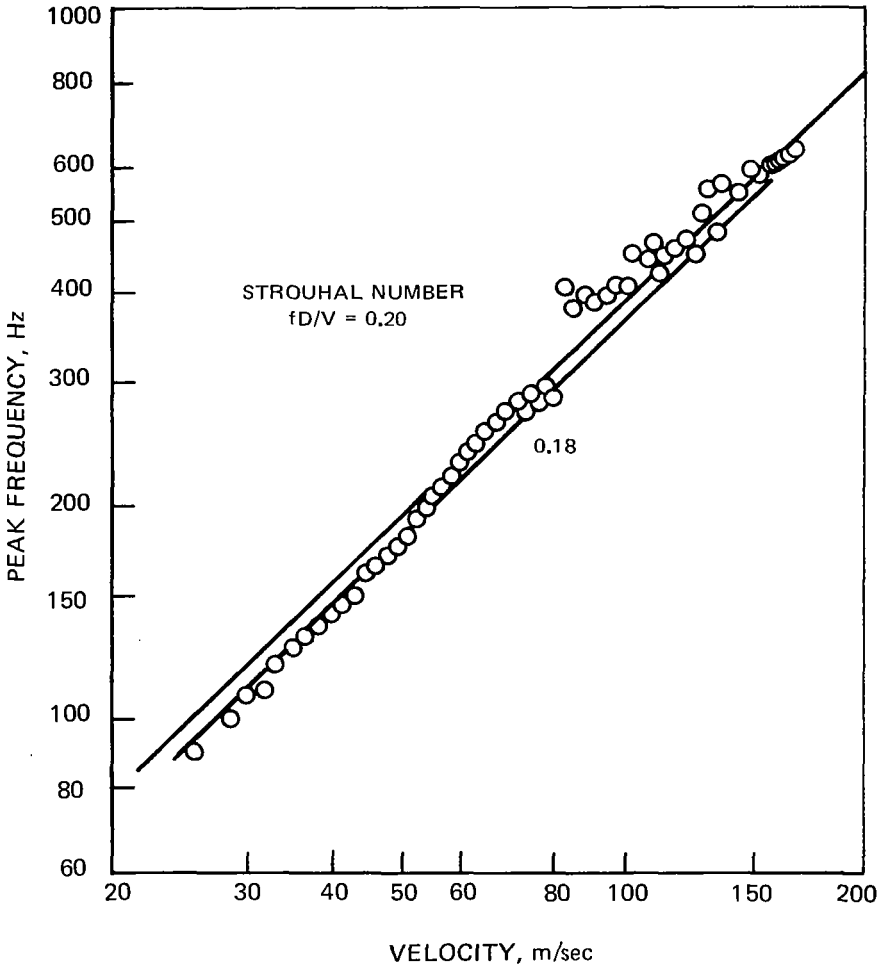

FIGURE 13 – VARIATION OF PEAK FREQUENCY WITH VELOCITY FOR A 5.08 CM CONSTANT–DIAMETER CYLINDER. NO UPSTREAM TURBULENCE GENERATOR

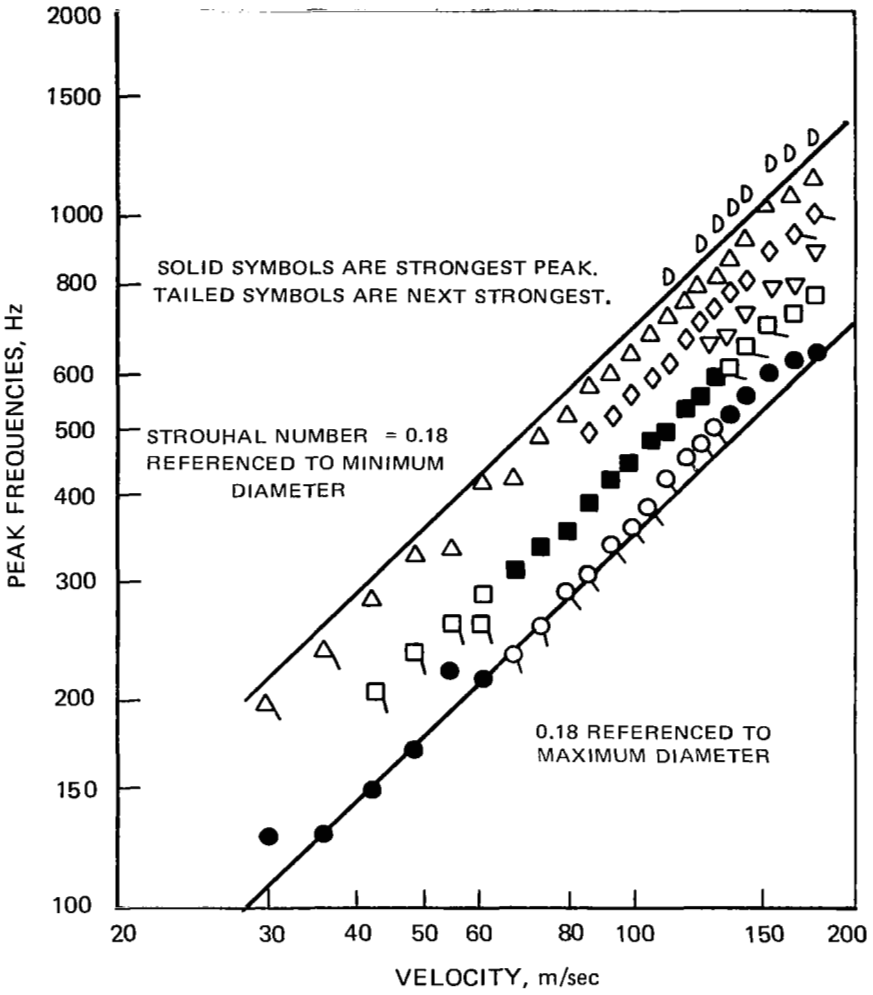

FIGURE 14 – VARIATION OF PEAK FREQUENCIES WITH VELOCITY FOR 2:1 TAPERED CYLINDER

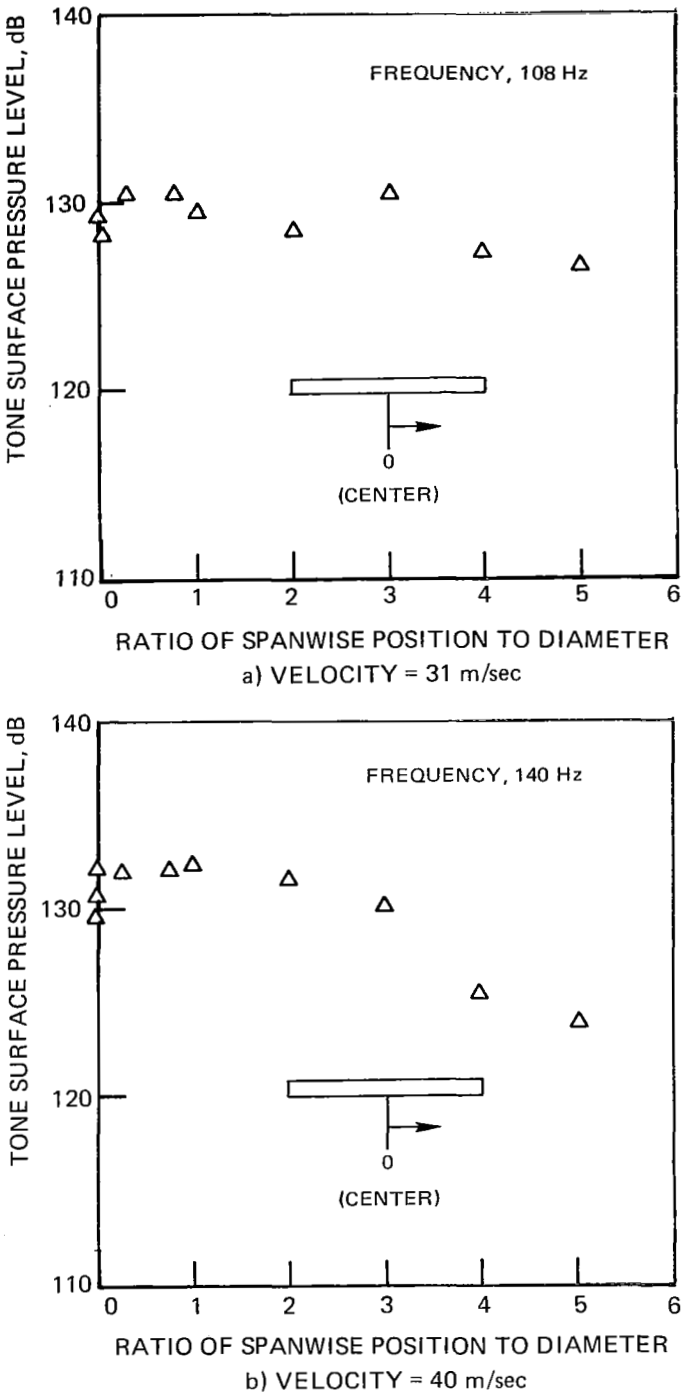

FIGURE 15 – VARIATION OF TONE SURFACE PRESSURE LEVEL WITH SPANWISE POSITION ON THE CONSTANT – DIAMETER CYLINDER. NO UPSTREAM TURBULENCE GENERATOR.

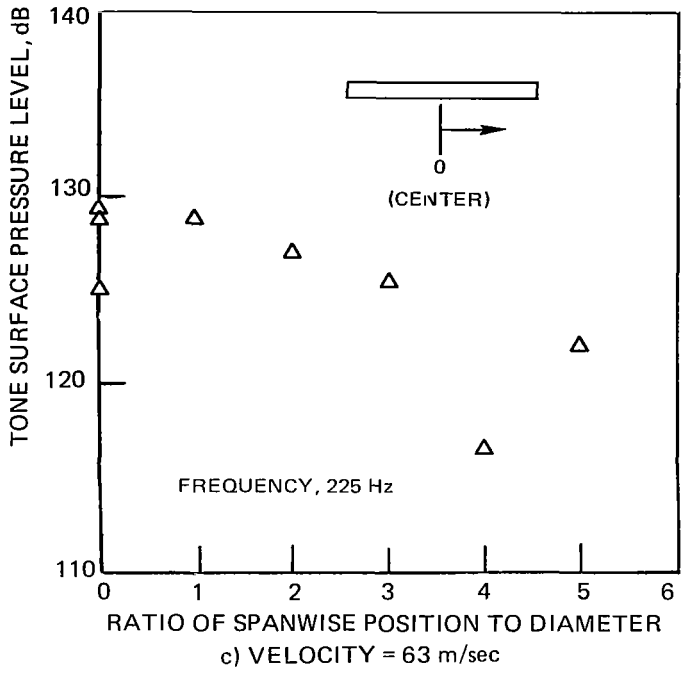

c) VELOCITY = 63 m/sec

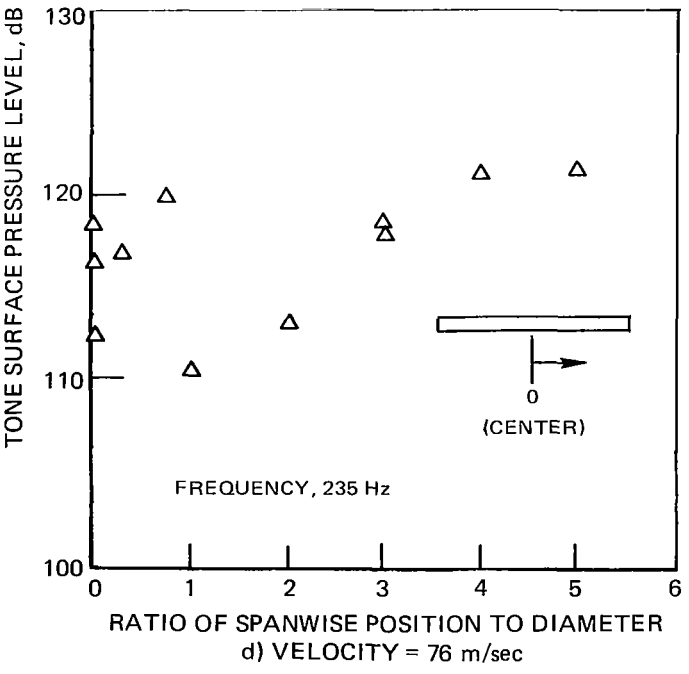

d) VELOCITY = 76 m/sec

FIGURE 15 – CONCLUDED.

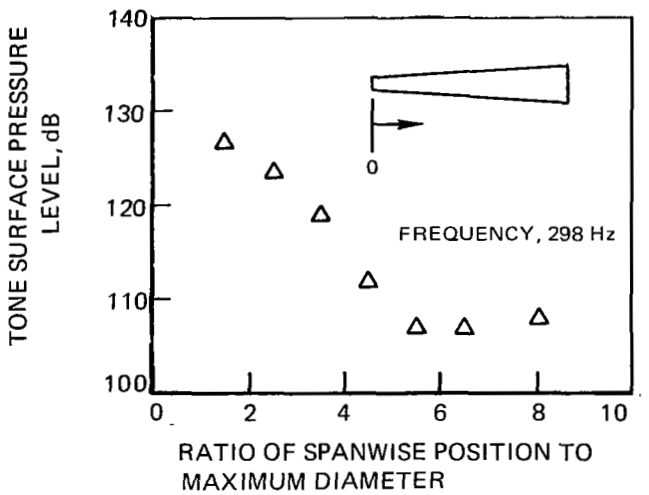

a) VELOCITY = 49 m/sec

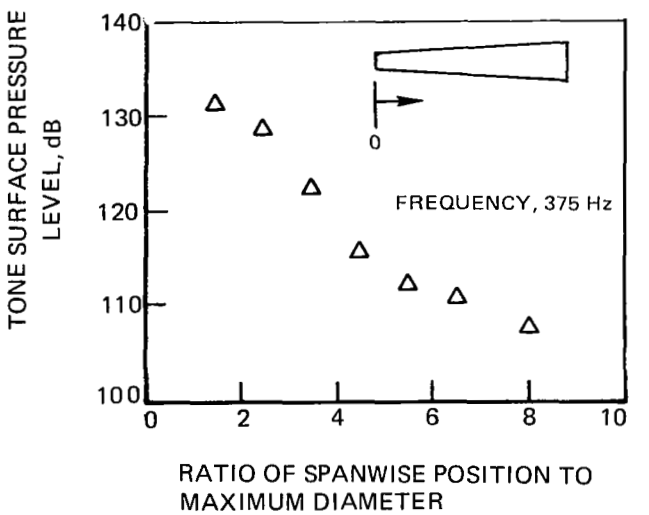

b) VELOCITY = 61 m/sec

FIGURE 16- VARIATION OF TONE SURFACE PRESSURE LEVEL WITH SPANWISE POSITION ON THE 2:1 TAPERED CYLINDER, NO UPSTREAM TURBULENCE GENERATOR.

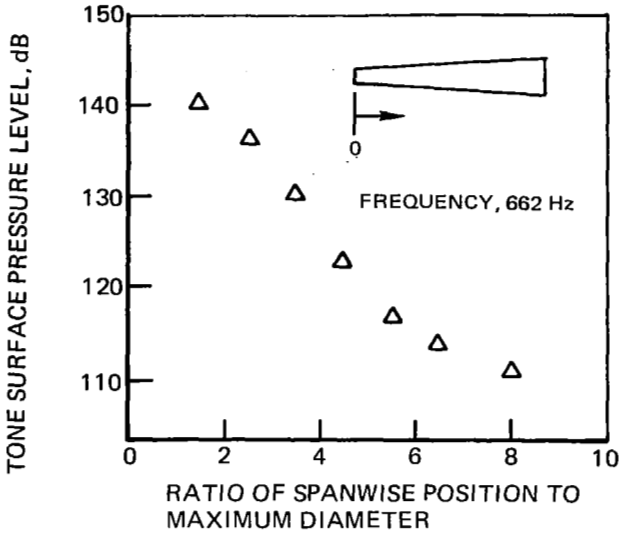

c) VELOCITY = 97.5 m/sec

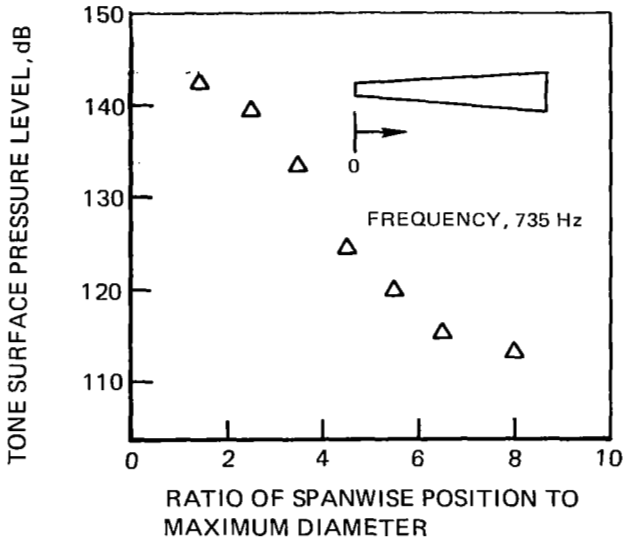

d) VELOCITY = 110 m/sec

FIGURE 16– CONCLUDED.

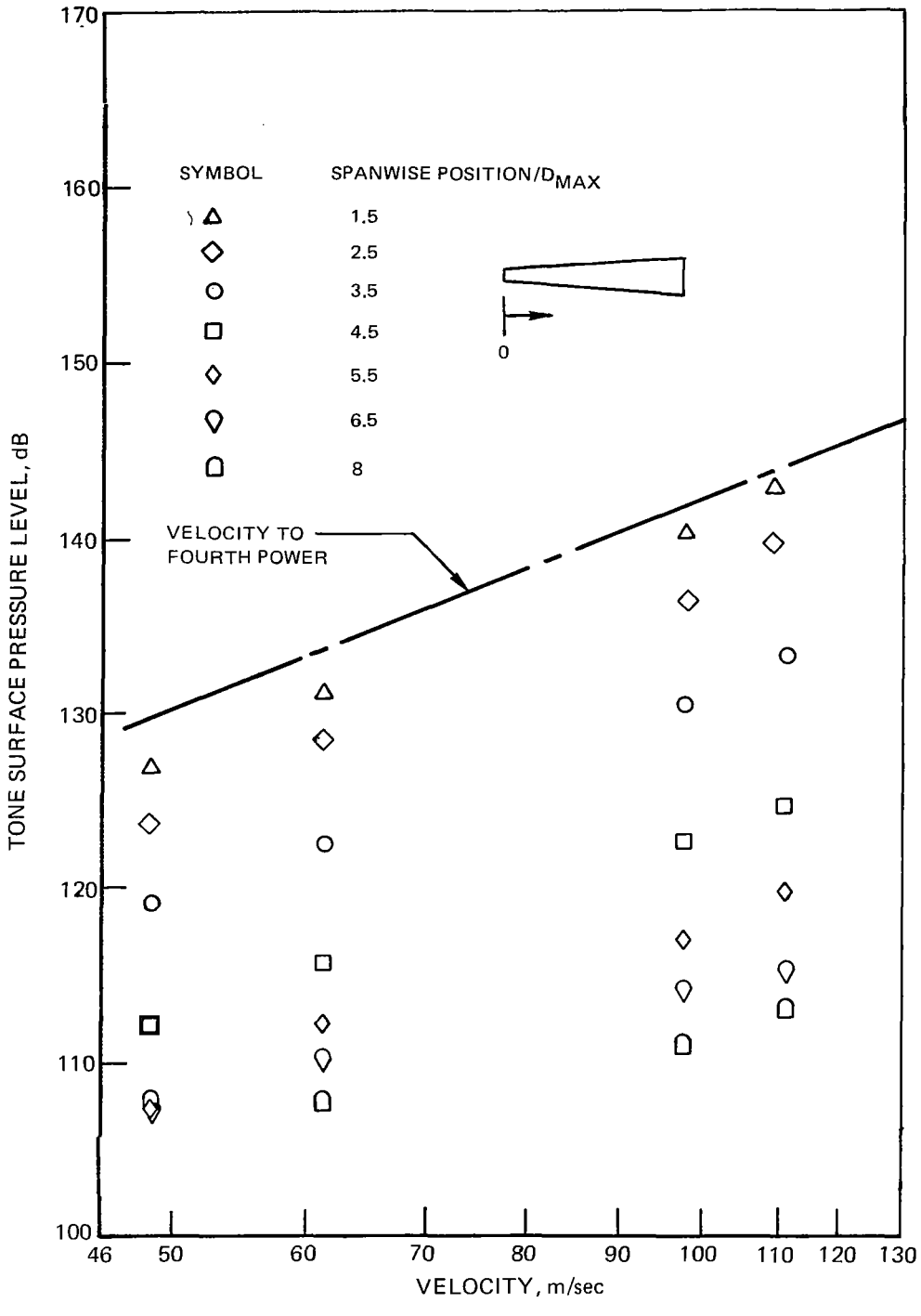

FIGURE 17– VELOCITY DEPENDENCE OF THE TONE SURFACE PRESSURE LEVEL AT FIXED SPANWISE POSITION, 2:1 TAPERED CYLINDER. NO UPSTREAM TURBULENCE GENERATOR.

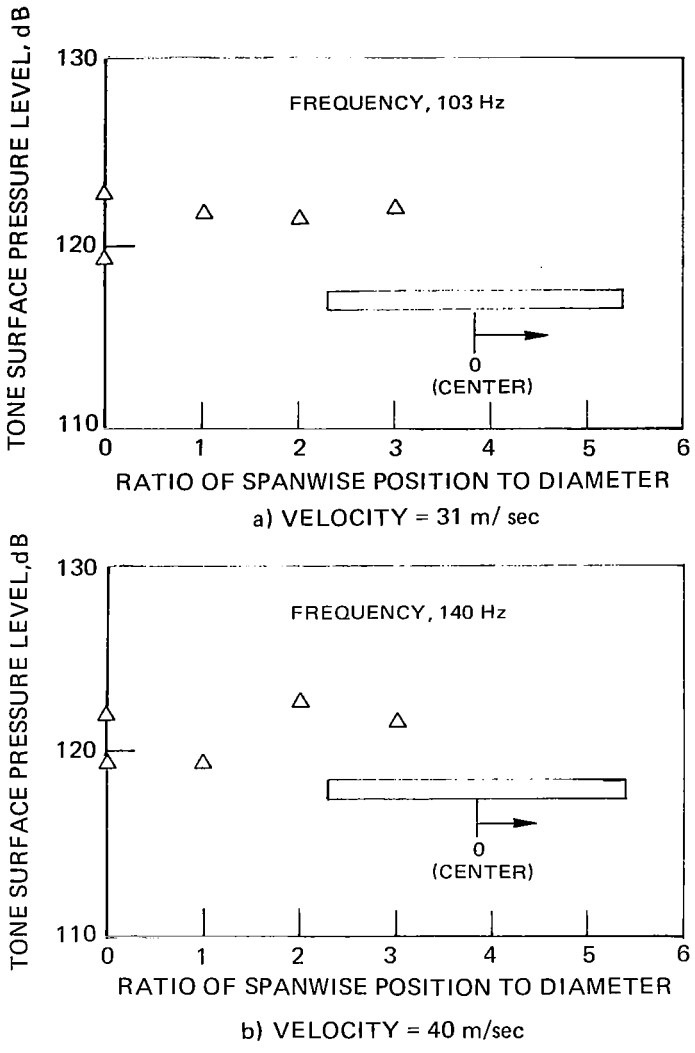

FIGURE 18 – VARIATION OF TONE SURFACE PRESSURE LEVEL WITH SPANWISE POSITION ON THE CONSTANT – DIAMETER CYLINDER WITH UPSTREAM TURBULENCE GENERATOR.

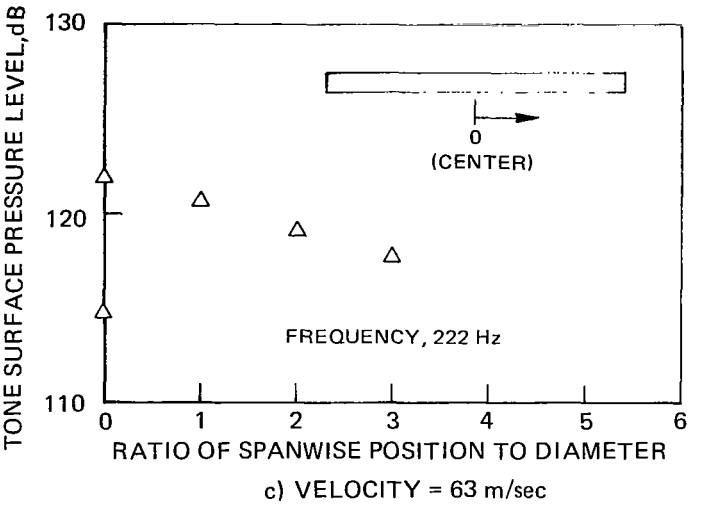

c) VELOCITY = 63 m/sec

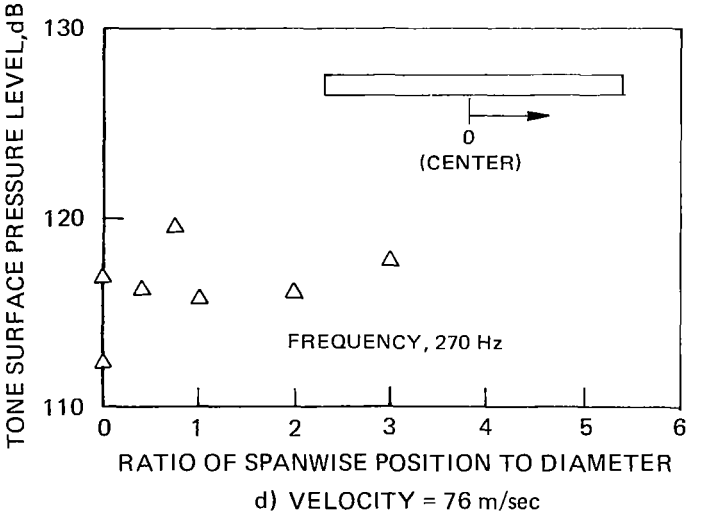

d) VELOCITY = 76 m/sec

FIGURE 18– CONCLUDED.

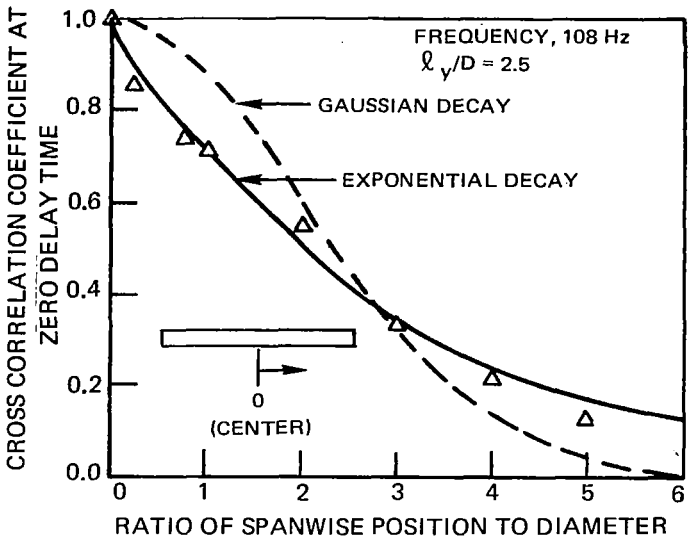

a) VELOCITY = 31 m/sec

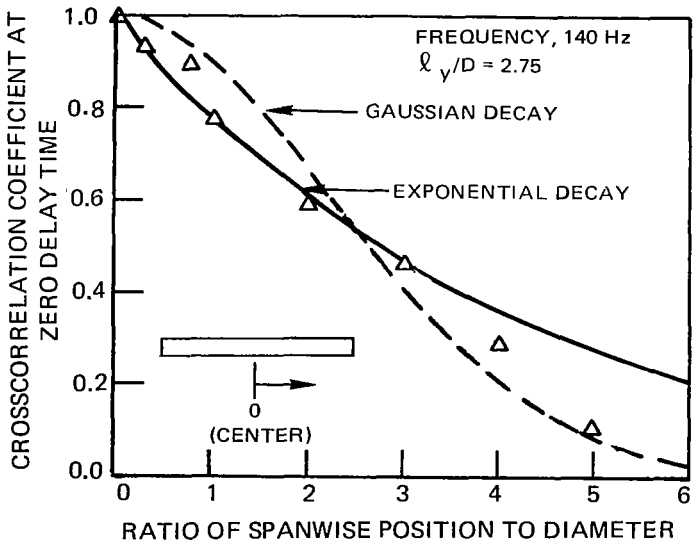

b) VELOCITY = 40 m/sec

FIGURE 19– VARIATION OF CROSSCORRELATION COEFFICIENT WITH VELOCITY FOR CONSTANT –DIAMETER CYLINDER, NO UPSTREAM TURBULENCE GENERATOR .

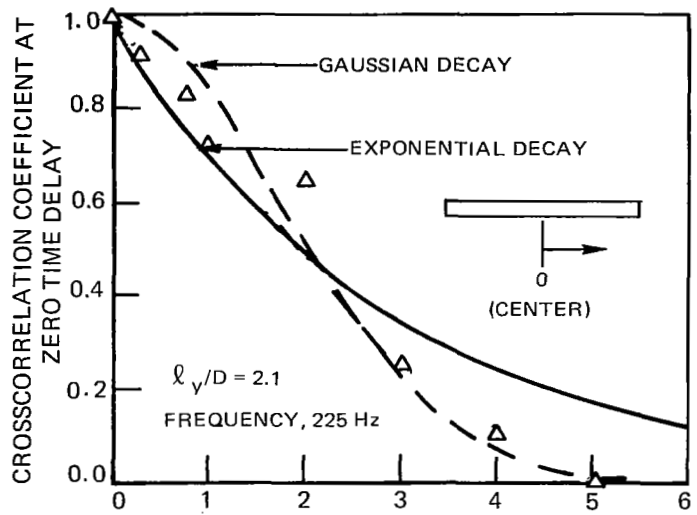

c) VELOCITY = 63 m/sec

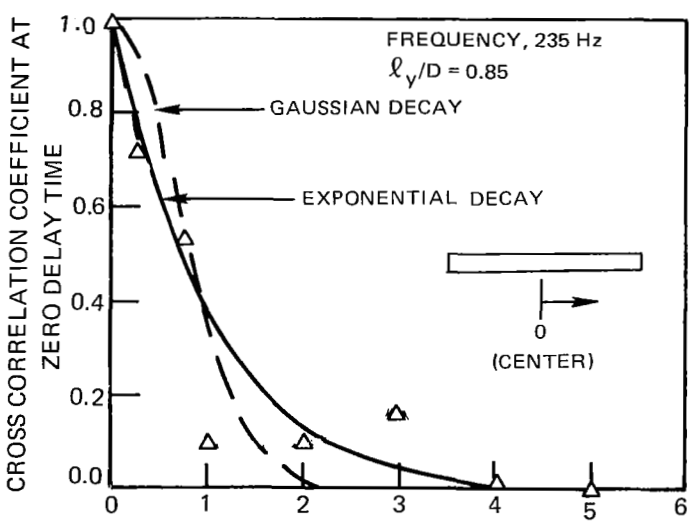

d) VELOCITY = 76 m/sec

FIGURE 19 – CONCLUDED.

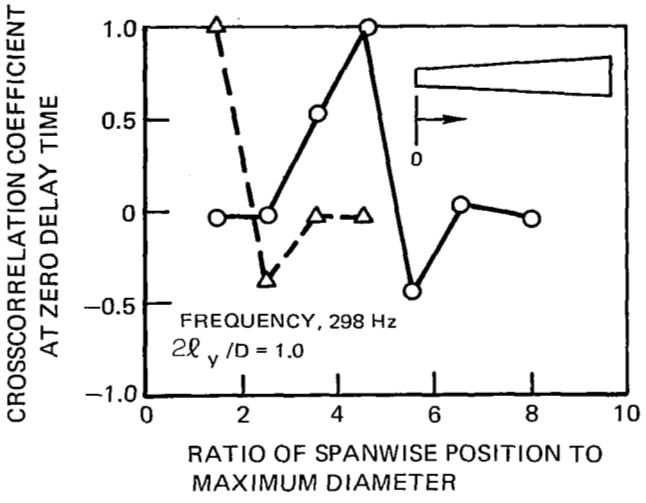

a) VELOCITY = 49 *m/sec*

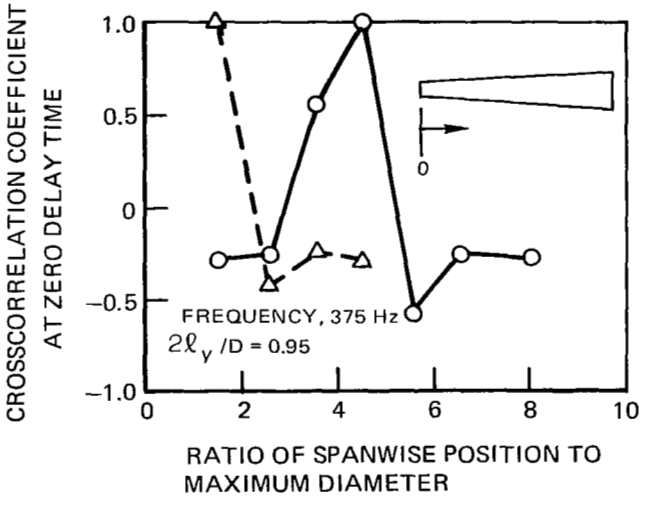

b) VELOCITY = 61 m/sec

FIGURE 20 - VARIATION OF CROSSCORRELATION COEFFICIENT WITH VELOCITY FOR THE 2:1 TAPERED CYLINDER , NO UPSTREAM TURBULENCE GENERATOR CROSSCORRELATION.

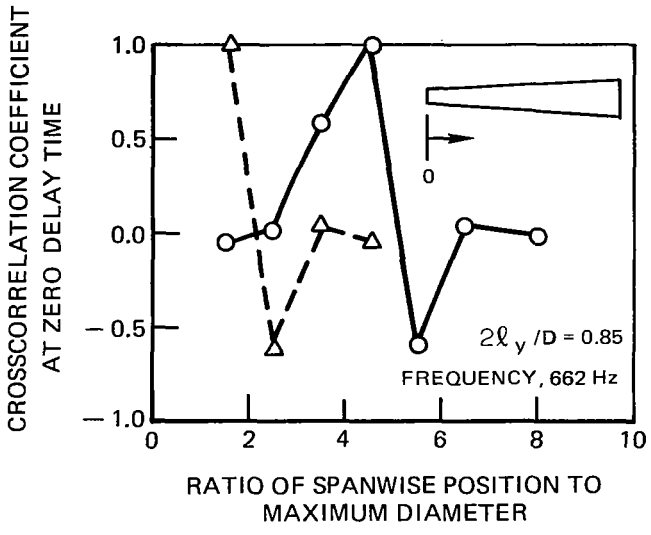

c) VELOCITY = 97.5 m/sec

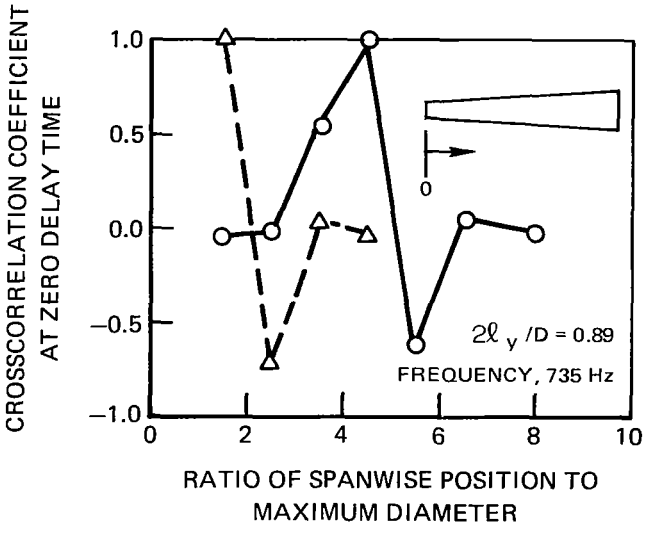

d) VELOCITY = 110 m/sec

FIGURE 20— CONCLUDED.

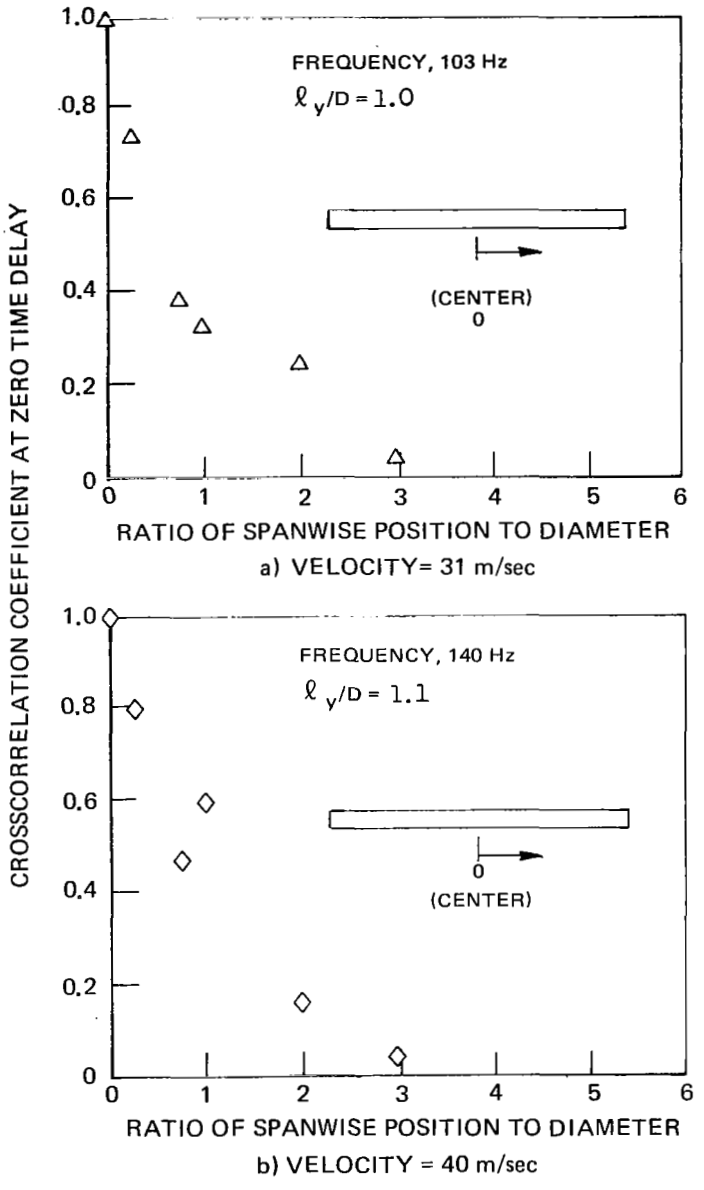

FIGURE 21– VARIATION OF CROSSCORRELATION COEFFICIENT WITH VELOCITY FOR CONSTANT – DIAMETER CYLINDER WITH UPSTREAM TURBULENCE GENERATOR.

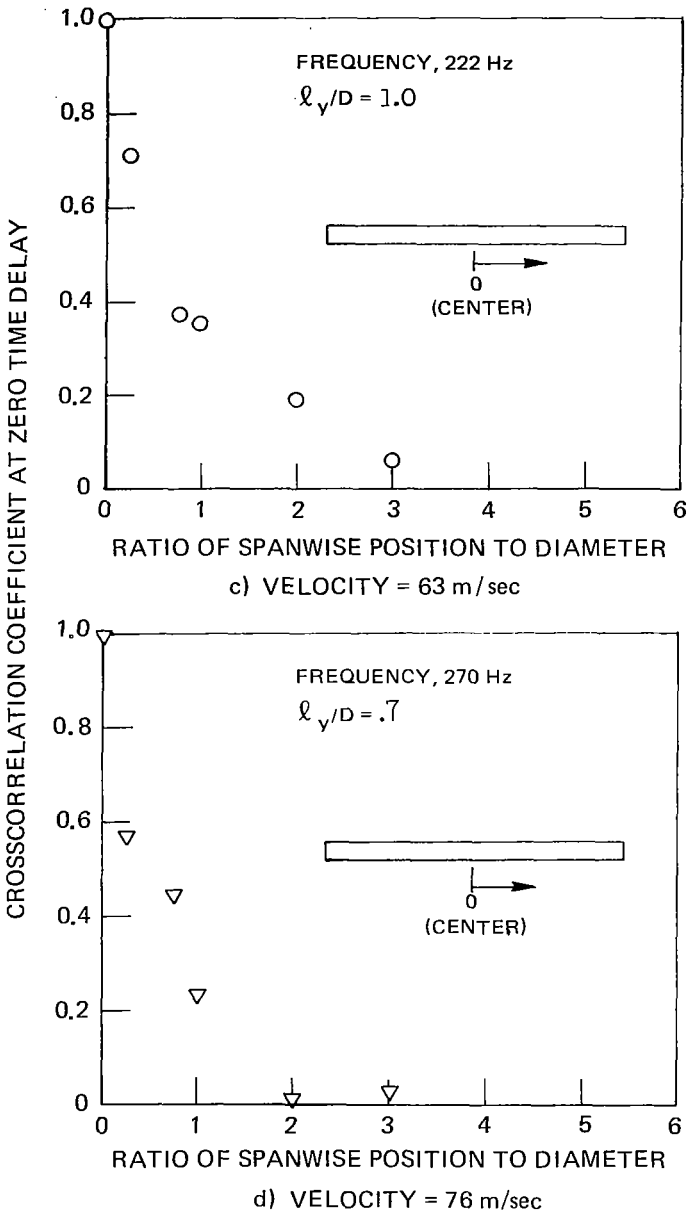

FIGURE 21– CONCLUDED.

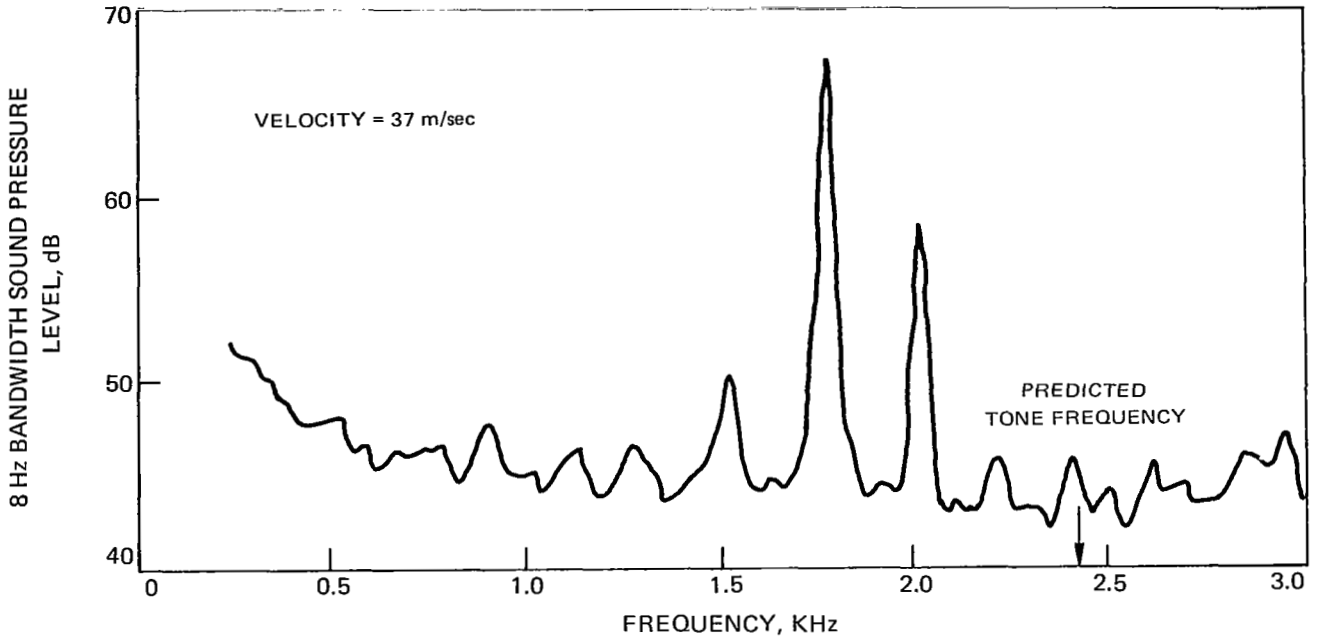

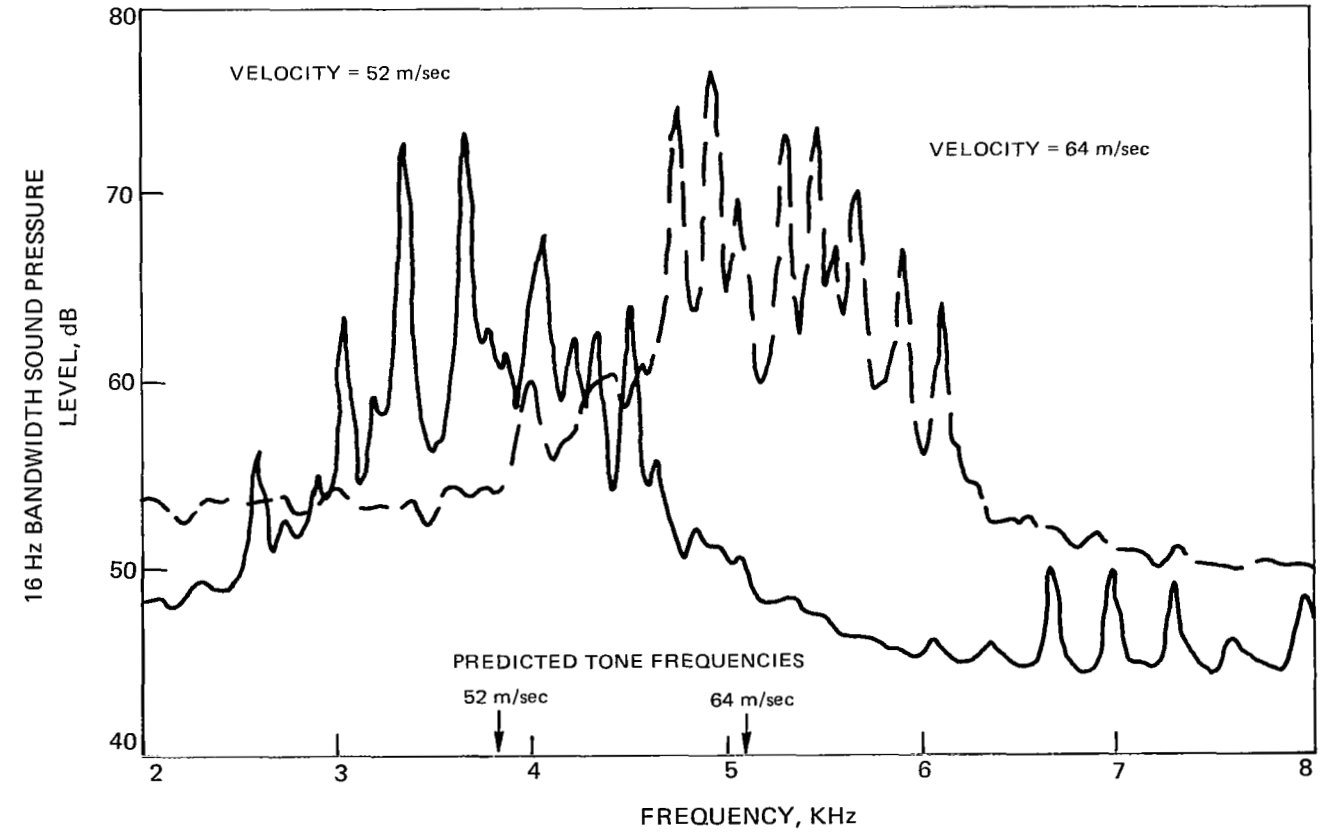

FIGURE 22 – NARROW BAND SPECTRA DIRECTLY ABOVE CONSTANT CHORD AIRFOIL AT –4° ANGLE OF ATTACK AND 37, 52, AND 64 m/sec VELOCITIES, NO UPSTREAM TURBULENCE GENERATOR.

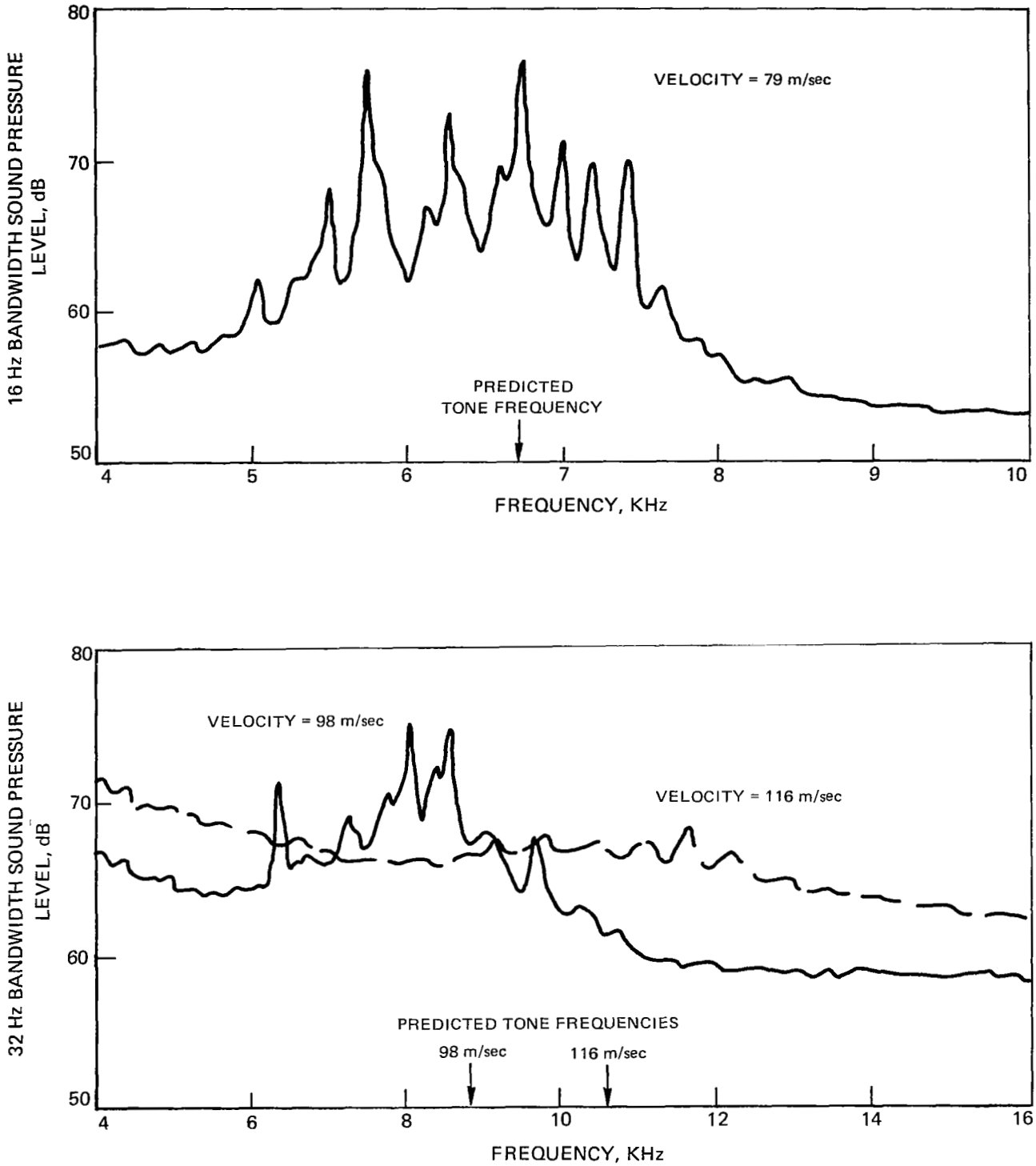

FIGURE 23 – NARROWBAND SPECTRA DIRECTLY ABOVE CONSTANT CHORD AIRFOIL AT –4° ANGLE OF ATTACK AND 79, 98, AND 116 m/sec VELOCITIES , NO UPSTREAM TURBULENCE GENERATOR.

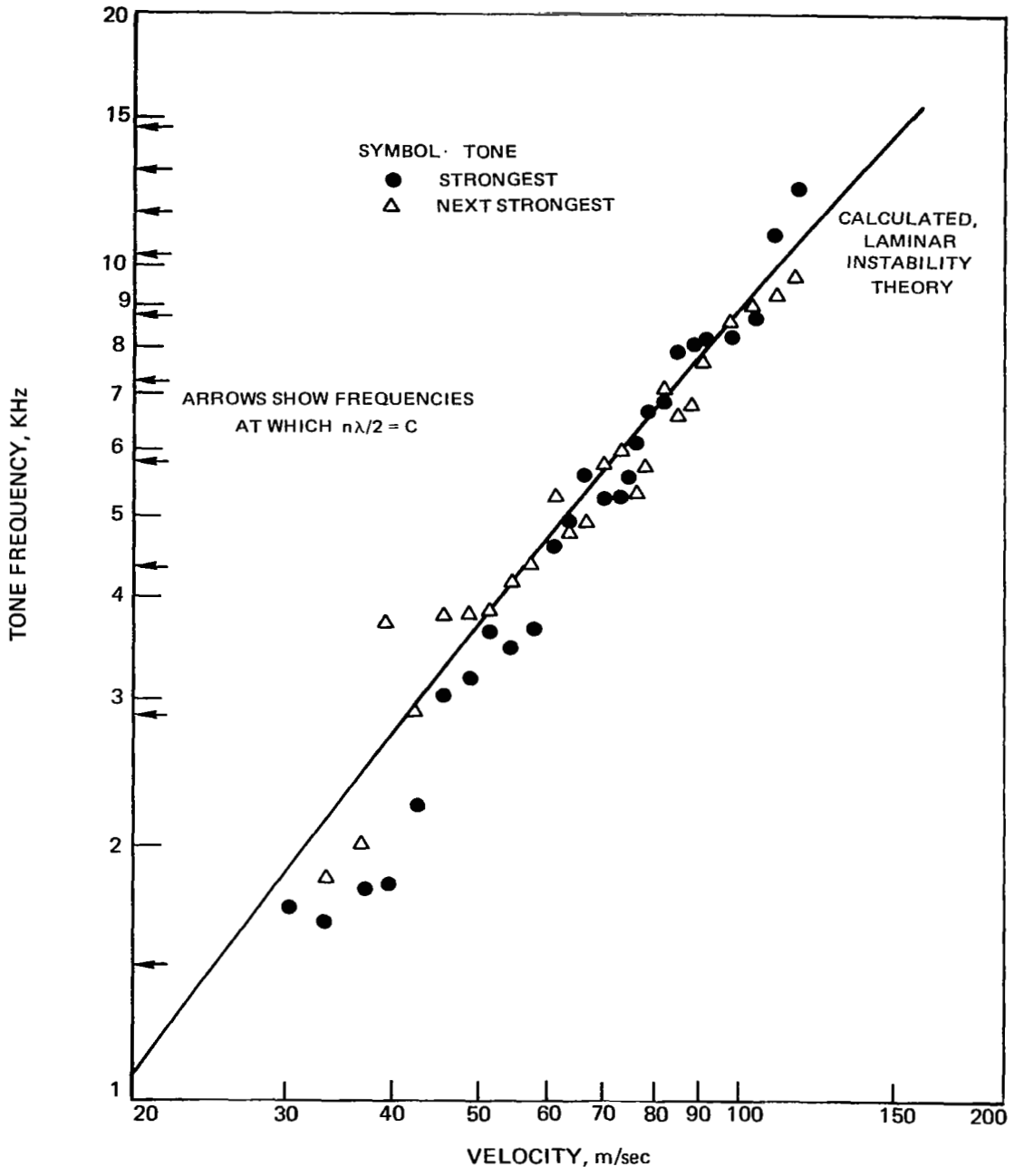

IGURE 24 – VARIATION OF FAR–FIELD TONE FREQUENCY WITH VELOCITY FOR CONSTANT CHORD AIRFOIL AT –4° ANGLE OF ATTACK , NO UPSTREAM TURBULENCE GENERATOR.

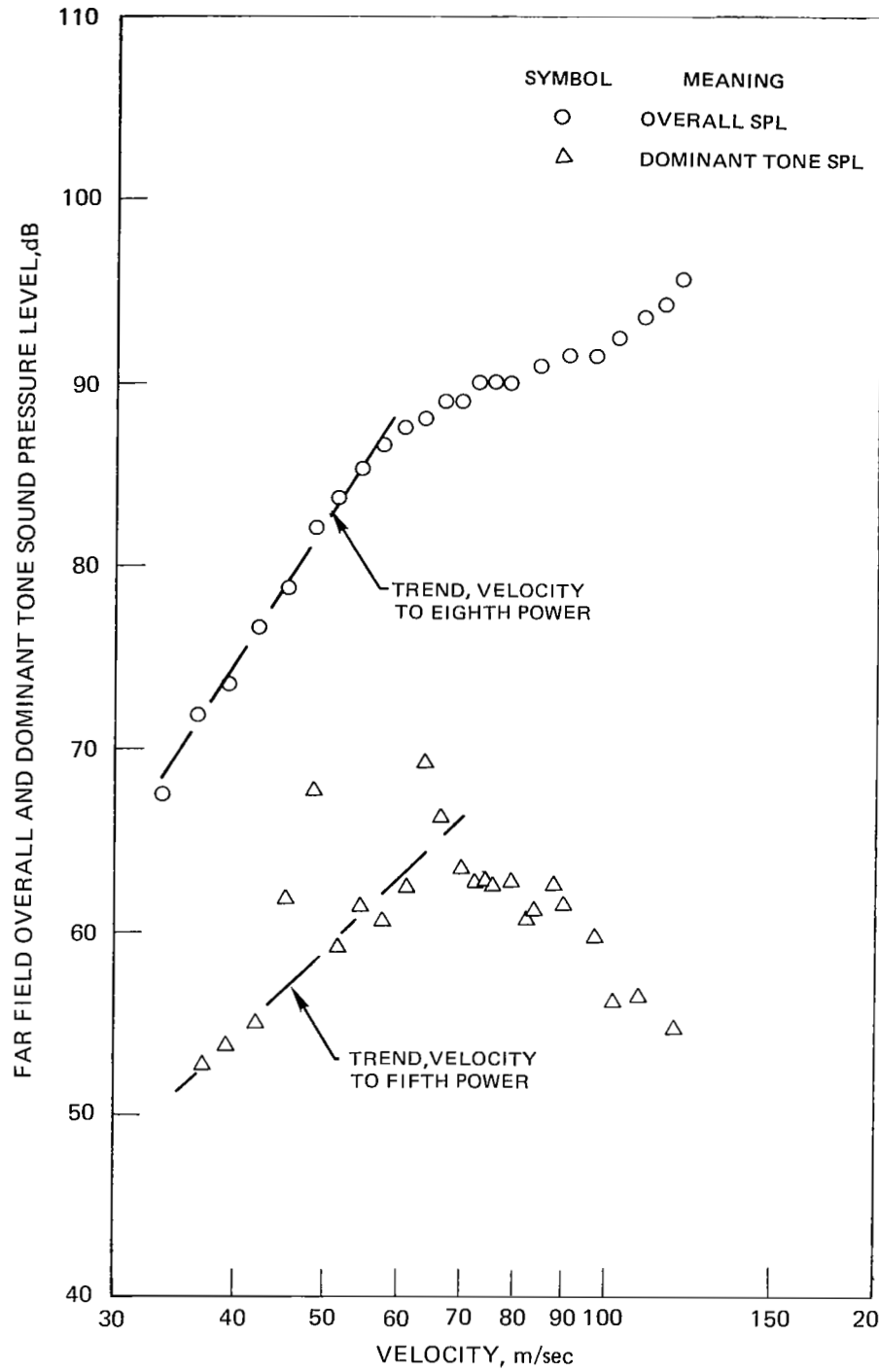

FIGURE 25 – VARIATION OF OVERALL SOUND PRESSURE LEVEL, AND DOMINANT TONE SOUND PRESSURE LEVEL, WITH VELOCITY FOR CONSTANT – CHORD AIRFOIL AT – 4 º ANGLE OF ATTACK. NO UPSTREAM TURBULENCE GENERATOR.

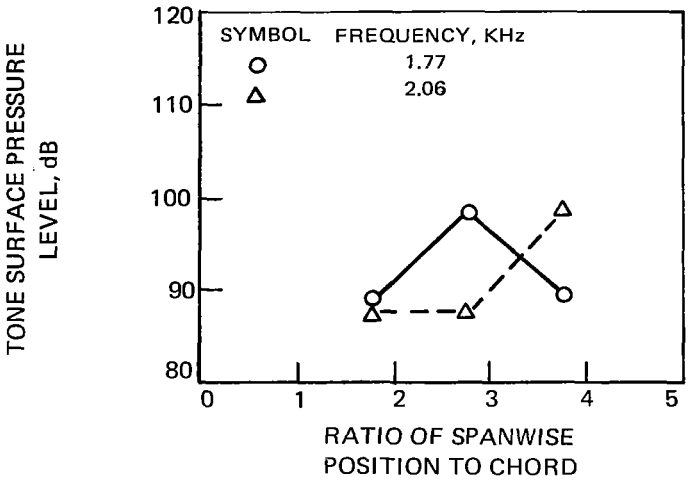

(a) VARIATION OF TONE SURFACE PRESSURE LEVELS WITH SPANWISE POSITION

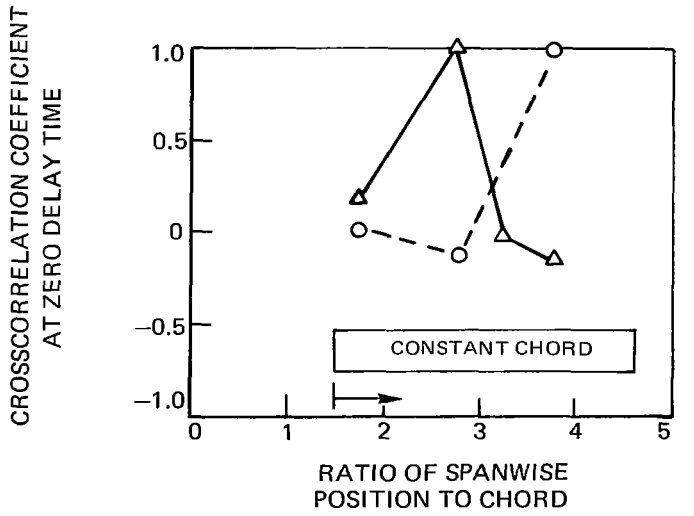

(b) VARIATION OF CROSSCORRELATION COEFFICIENT WITH SPANWISE POSITION

FIGURE 26 – TONE SURFACE PRESSURE LEVEL AND CROSSCORRELATION COEFFICIENT FOR CONSTANT CHORD AIRFOIL, ANGLE OF ATTACK = 0°, VELOCITY = 31 m/sec , NO UPSTREAM TURBULENCE GENERATOR.

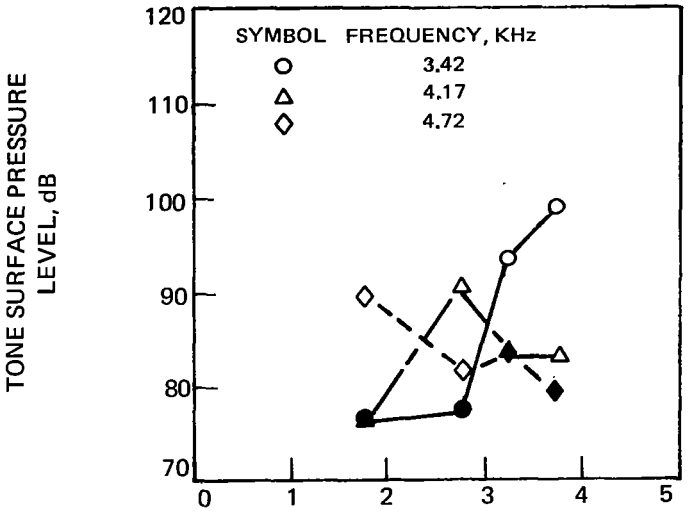

(a) VARIATION OF TONE SURFACE PRESSURE LEVEL WITH SPANWISE POSITION, SOLID SYMBOLS INDICATE BROADBAND LEVEL

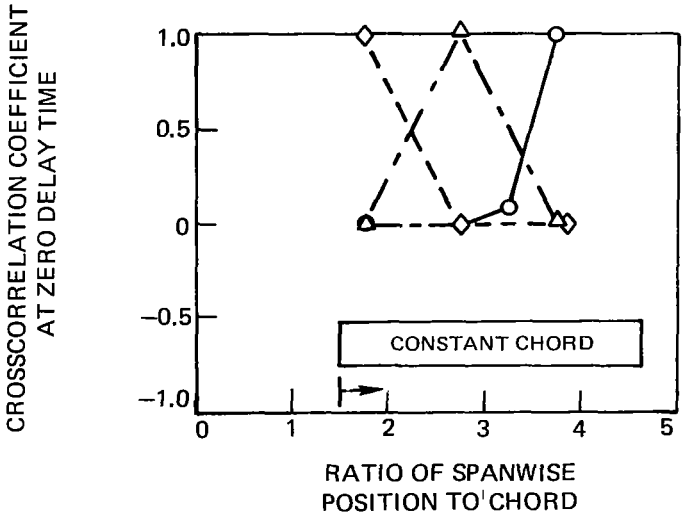

(b) VARIATION OF CROSSCORRELATION COEFFICIENT WITH SPANWISE POSITION

FIGURE 27 – TONE SURFACE PRESSURE LEVEL AND CROSSCORRELATION COEFFICIENT FOR CONSTANT CHORD AIRFOIL, ANGLE OF ATTACK = -4^{o}, VELOCITY = 54.2 m/sec , NO UPSTREAM TURBULENCE GENERATOR.

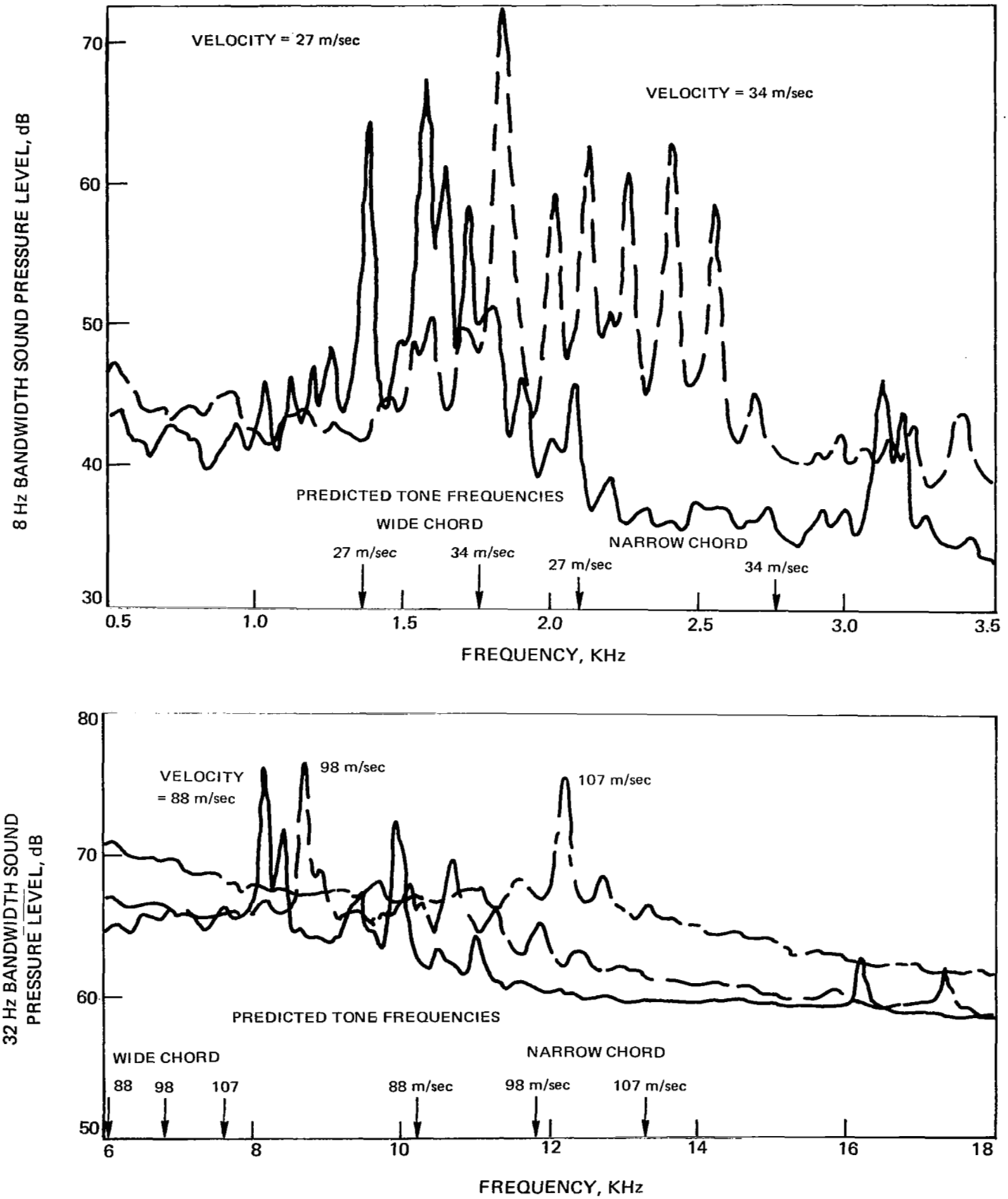

FIGURE 28– NARROWBAND SPECTRA DIRECTLY ABOVE 2:1 TAPERED CHORD AIRFOIL AT –4° ANGLE OF ATTACK AND 27, 34, 88, 98, AND 107 m/sec VELOCITIES.

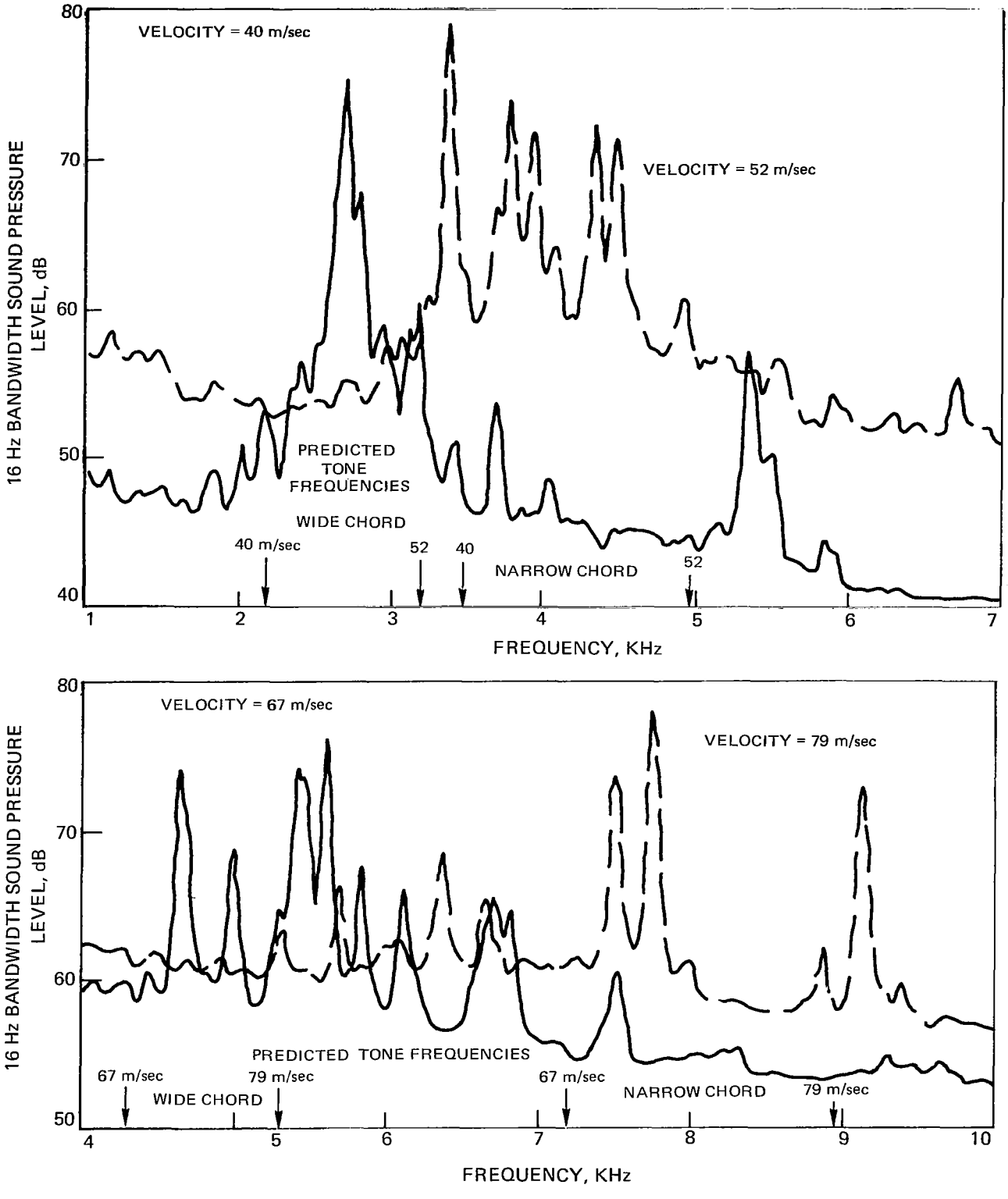

FIGURE 29 – NARROWBAND SPECTRA DIRECTLY ABOVE 2:1 TAPERED CHORD AIRFOIL AT –4° ANGLE OF ATTACK AND 40, 52, 67, AND 79 m/sec VELOCITIES.

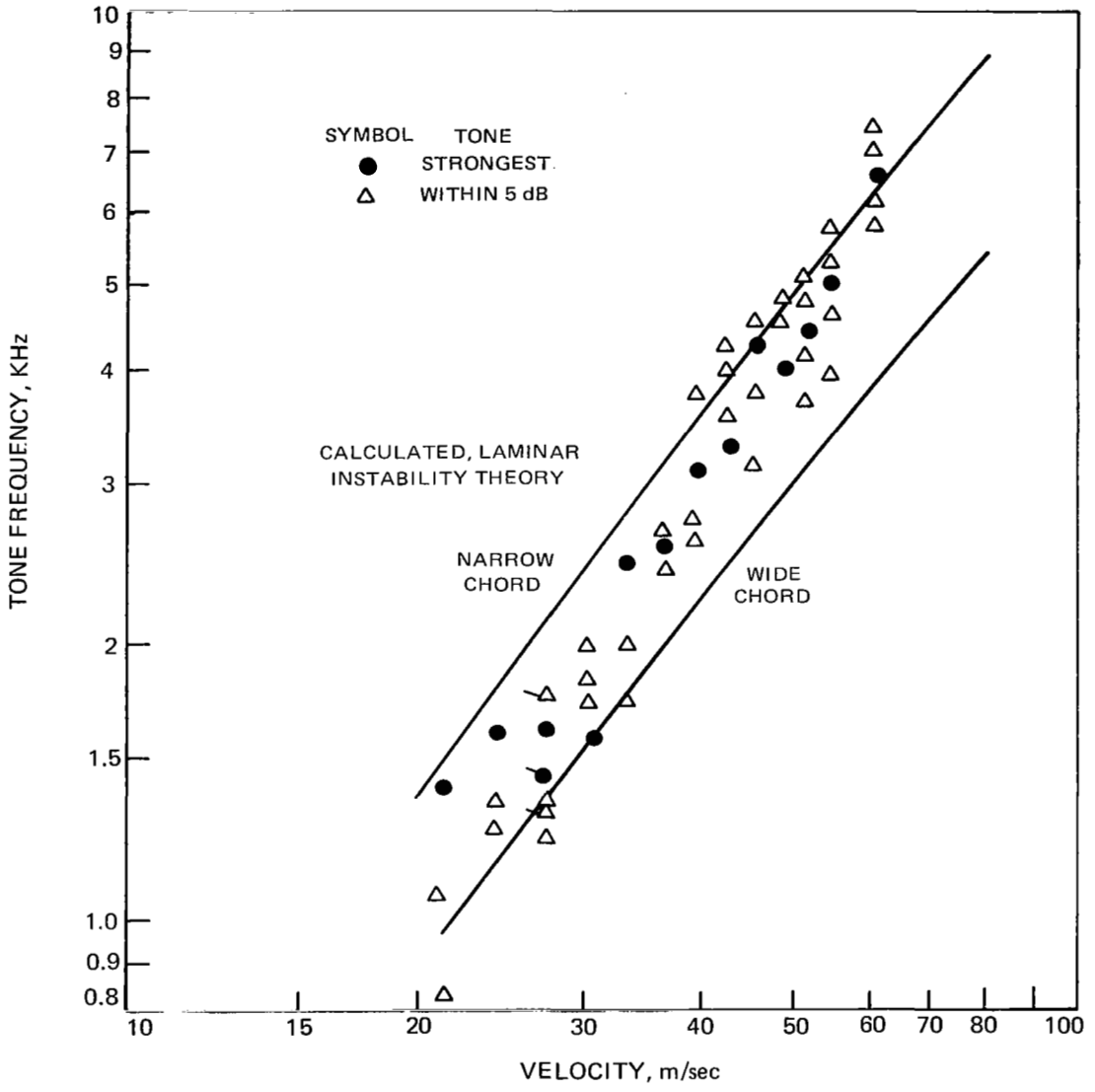

FIGURE 30 – VARIATION OF FAR–FIELD TONE FREQUENCY WITH VELOCITY FOR 2:1 TAPERED CHORD AIRFOIL AT 0° ANGLE OF ATTACK.

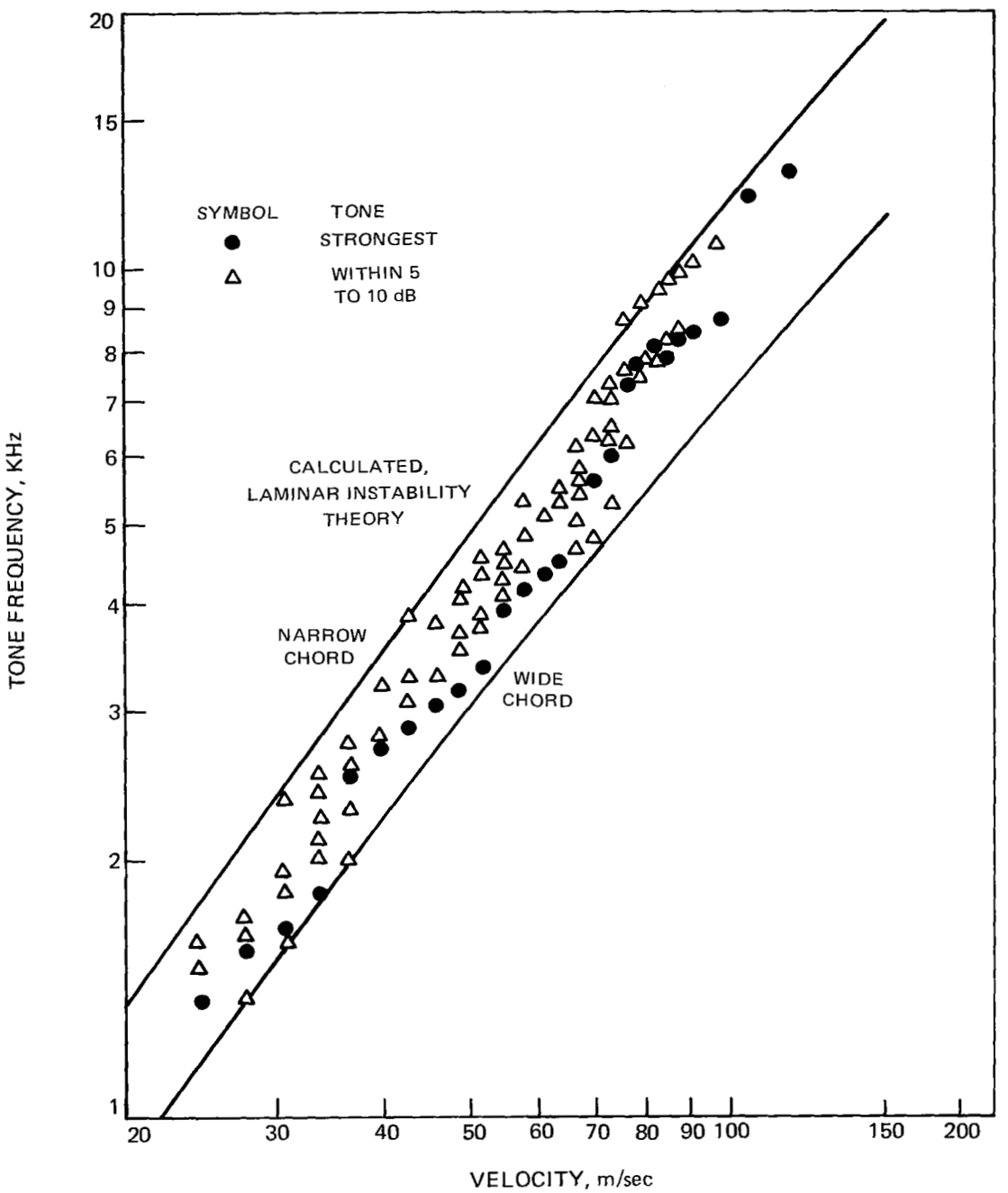

FIGURE 31 - VARIATION OF FAR–FIELD TONE FREQUENCY WITH VELOCITY FOR 2:1 TAPERED CHORD AIRFOIL AT –4° ANGLE OF ATTACK.

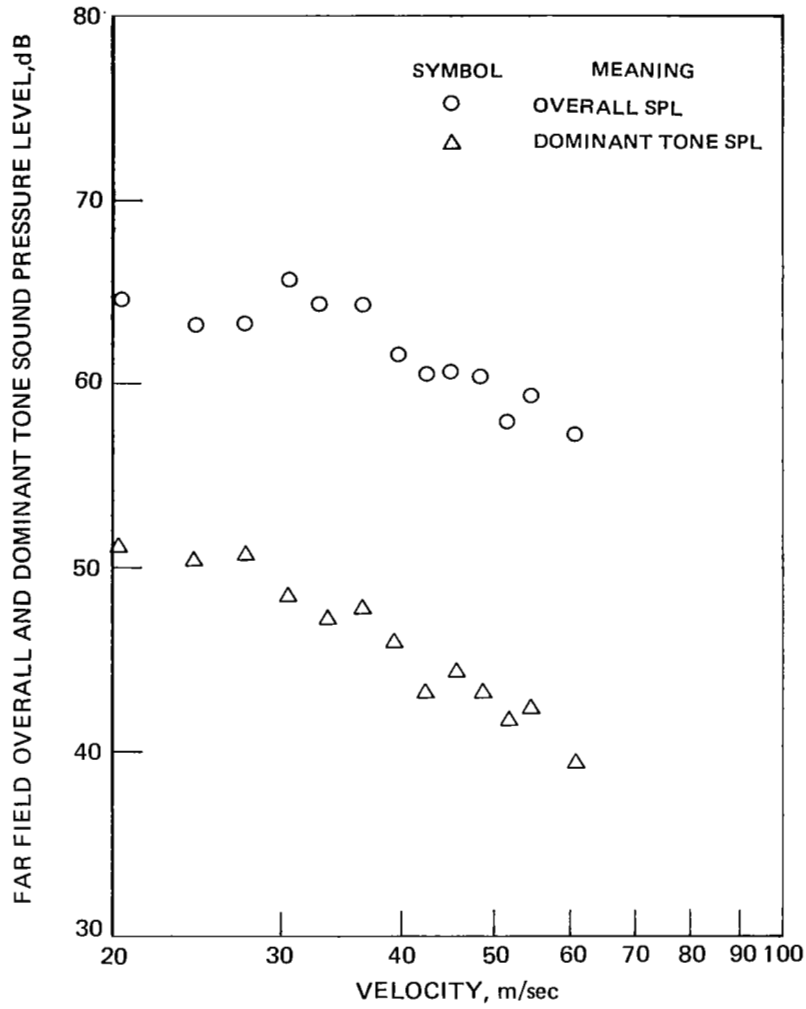

FIGURE 32 – VARIATION OF OVERALL AND DOMINANT TONE SOUND PRESSURE LEVEL, WITH VELOCITY FOR 2:1 TAPERED CHORD AIRFOIL AT 0º ANGLE OF ATTACK.

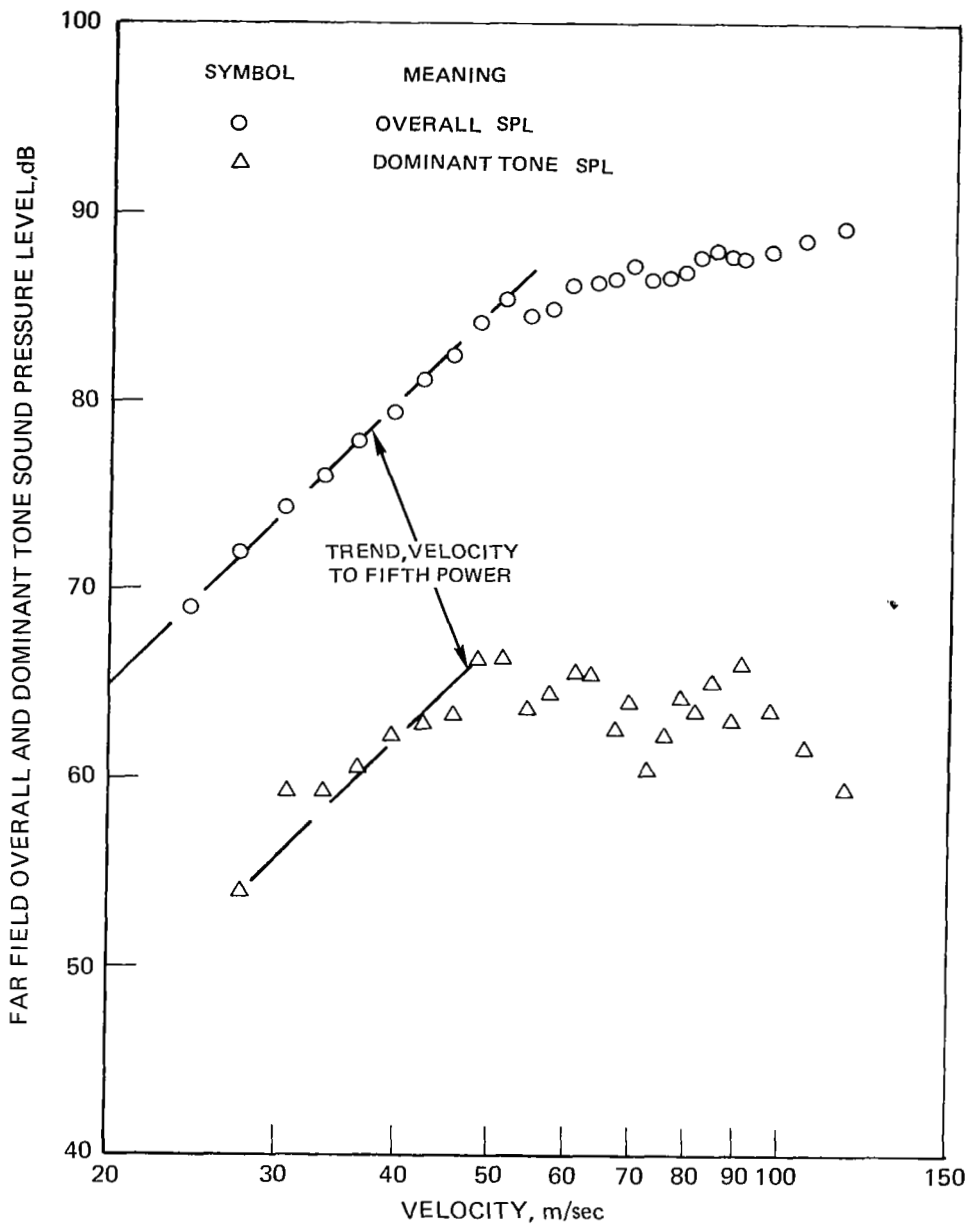

FIGURE 33 – VARIATION OF OVERALL SOUND PRESSURE LEVEL, AND DOMINANT TONE SOUND PRESSURE LEVEL, WITH VELOCITY FOR 2:1 TAPERED CHORD AIRFOIL, AT – 4 ^{o} ANGLE OF ATTACK.

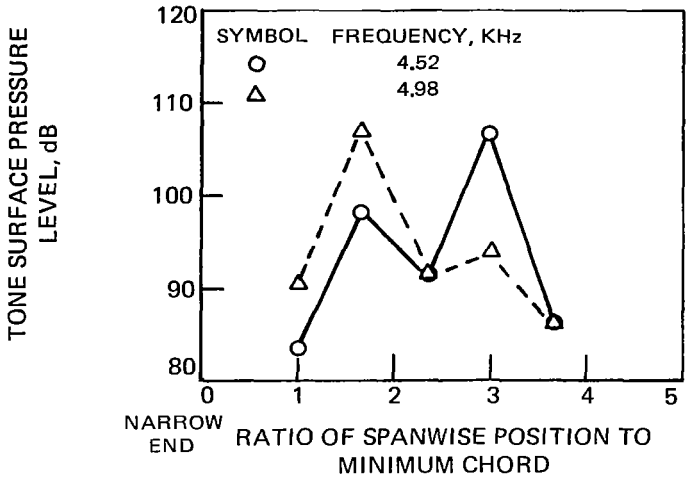

(a) VARIATION OF TONE SURFACE PRESSURE LEVELS WITH SPANWISE POSITION

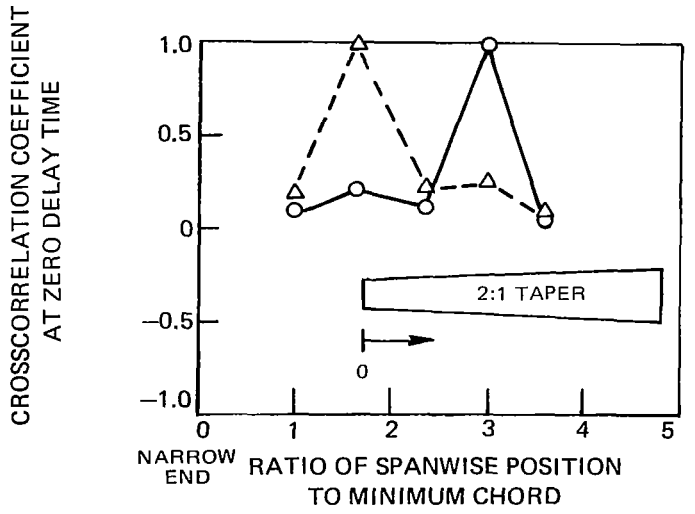

(b) VARIATION OF CROSSCORRELATION COEFFICIENT WITH SPANWISE POSITION

FIGURE 34 – TONE SURFACE PRESSURE LEVEL AND CROSSCORRELATION COEFFICIENT FOR 2:1 TAPERED CHORD AIRFOIL, ANGLE OF ATTACK = -4^{o}, VELOCITY = 48 m/sec.

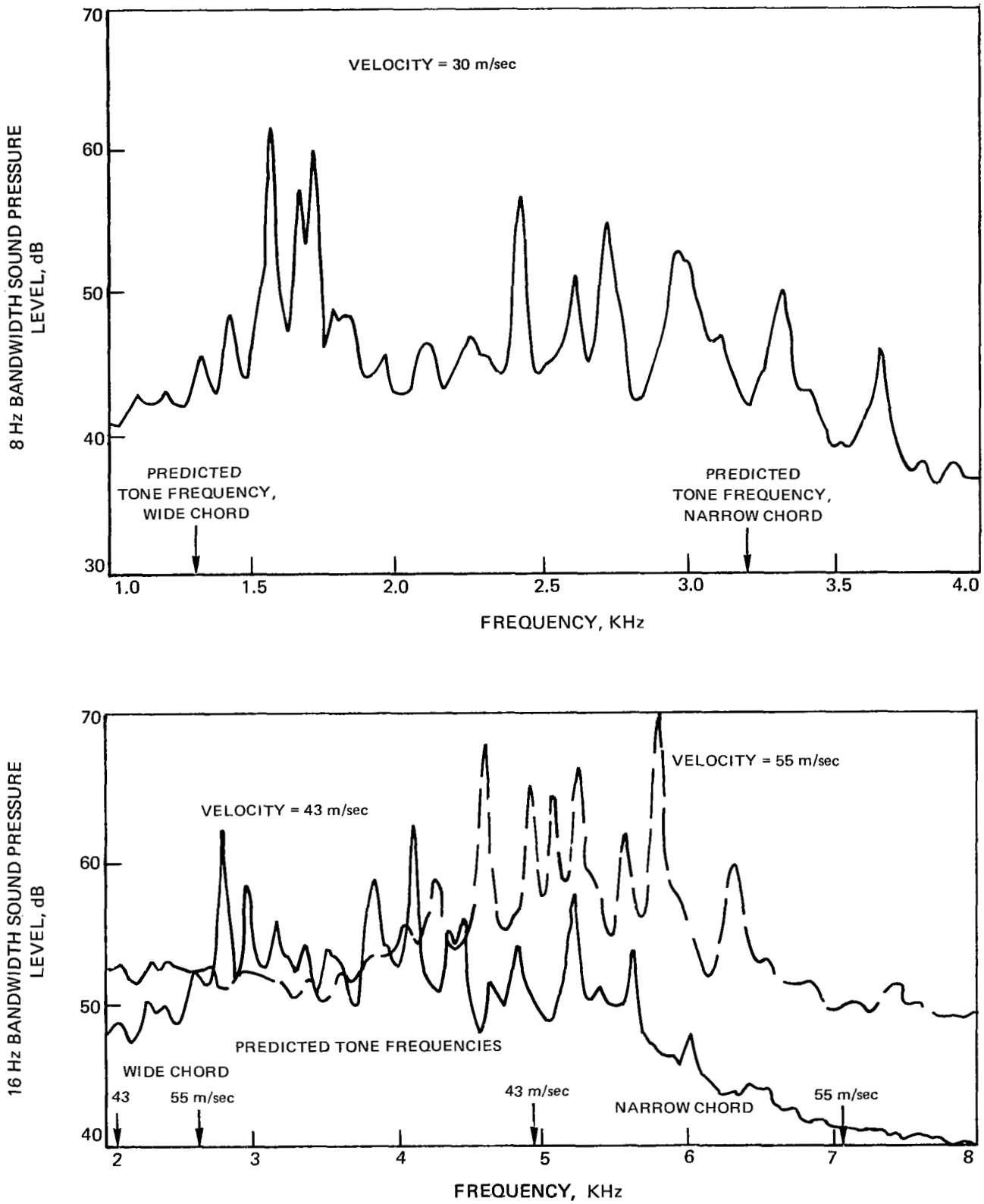

FIGURE 35 – NARROW BAND SPECTRA DIRECTLY ABOVE 4:1 TAPERED CHORD AIRFOIL AT 0° ANGLE OF ATTACK AND 30, 43, AND 55 m/sec VELOCITIES.

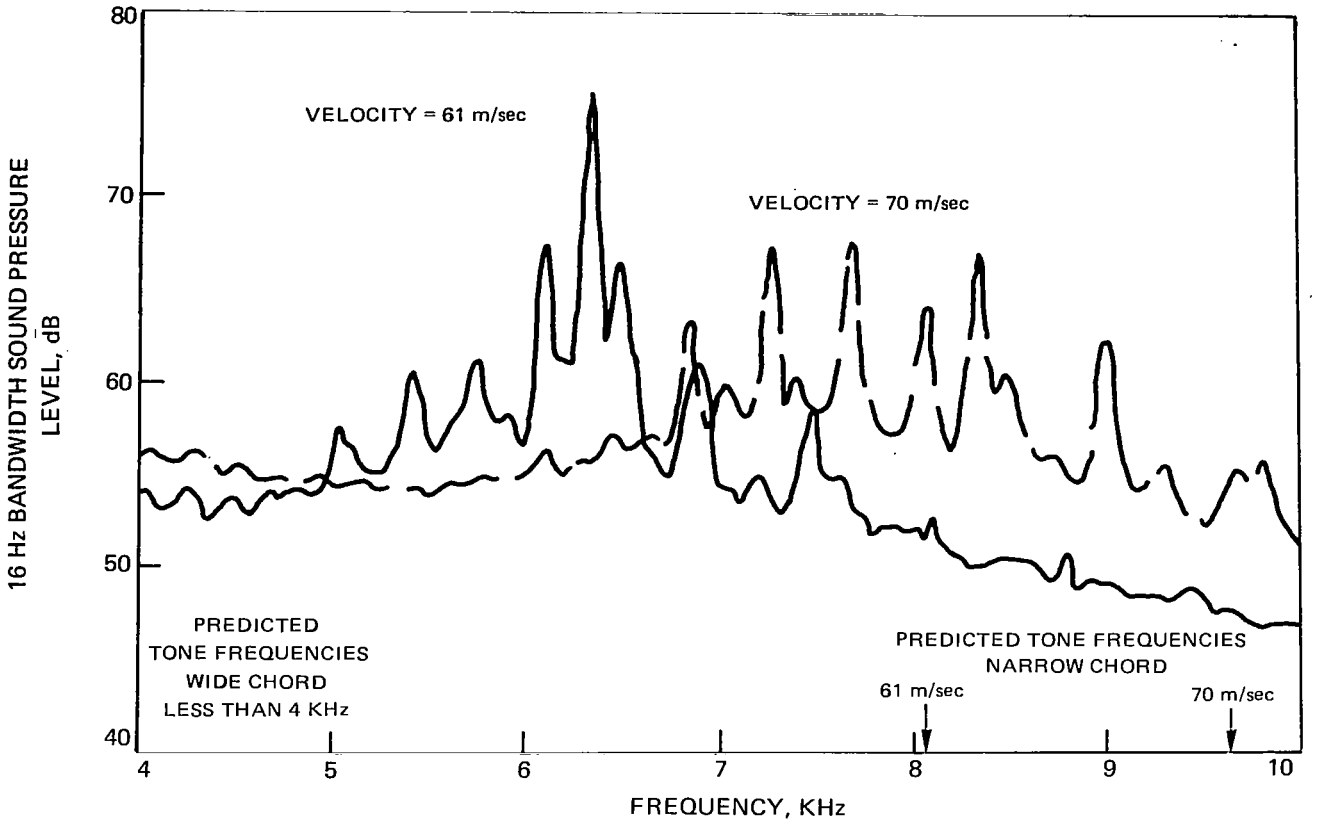

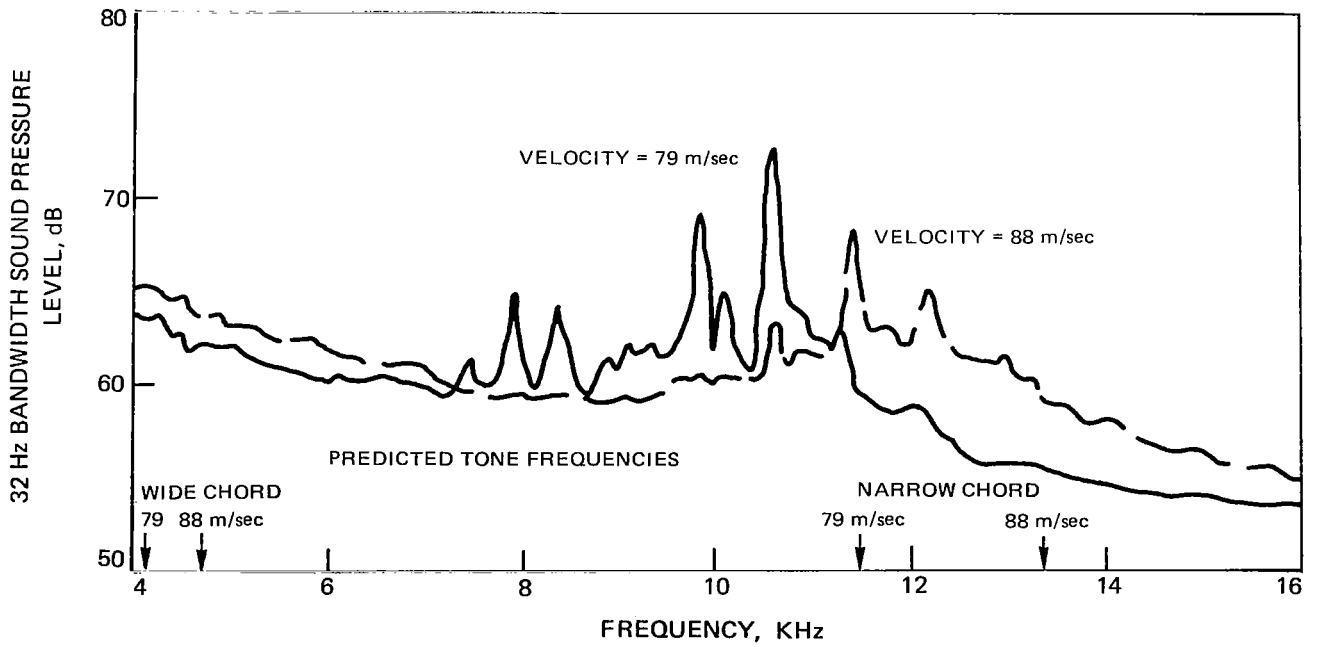

FIGURE 36– NARROWBAND SPECTRA DIRECTLY ABOVE 4:1 TAPERED CHORD AIRFOIL AT 0° ANGLE OF ATTACK AND 61, 70, 79, AND 88 m/sec VELOCITIES.

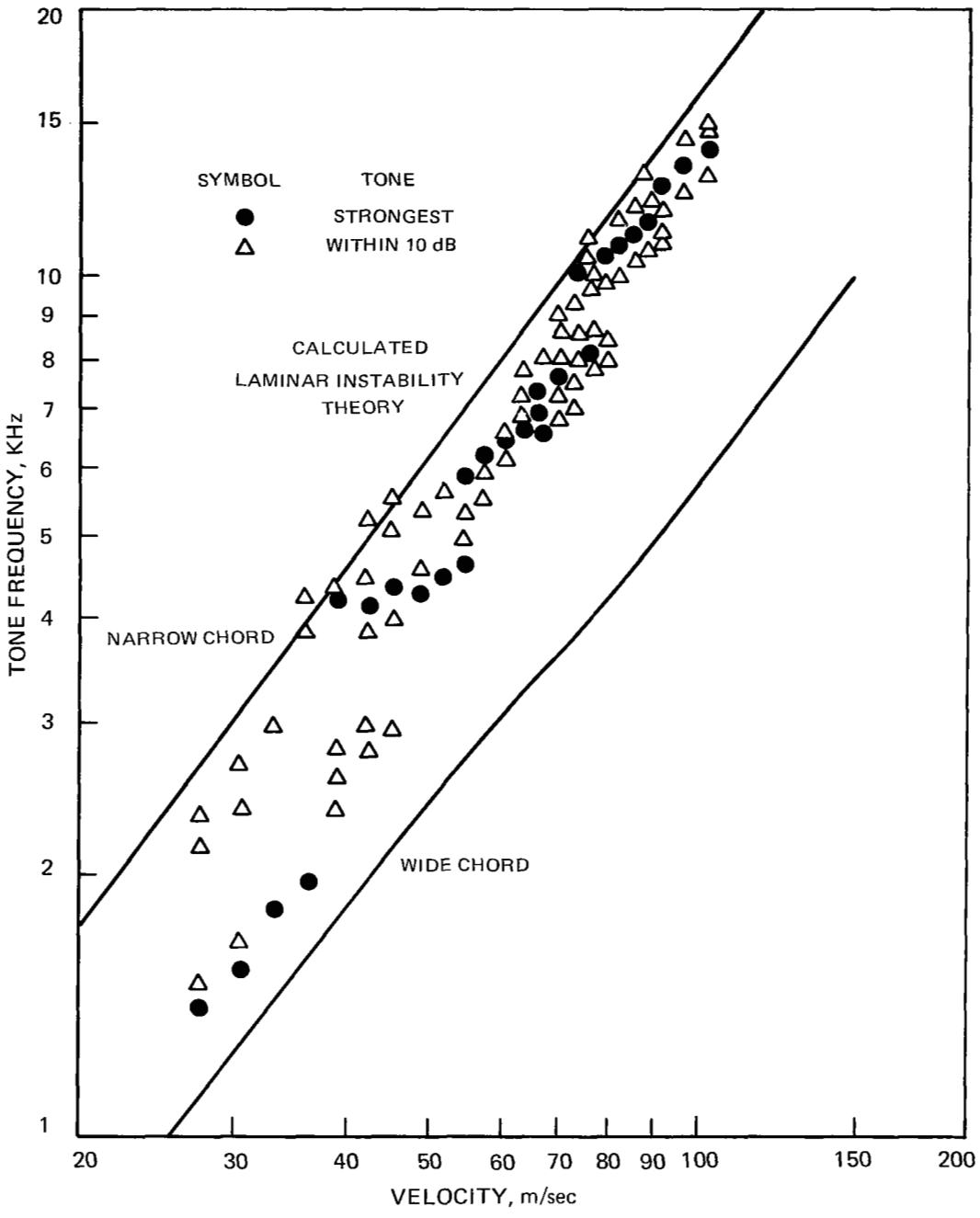

FIGURE 37 – VARIATION OF FAR–FIELD TONE FREQUENCY WITH VELOCITY FOR 4:1 TAPERED CHORD AIRFOIL AT 0° ANGLE OF ATTACK.

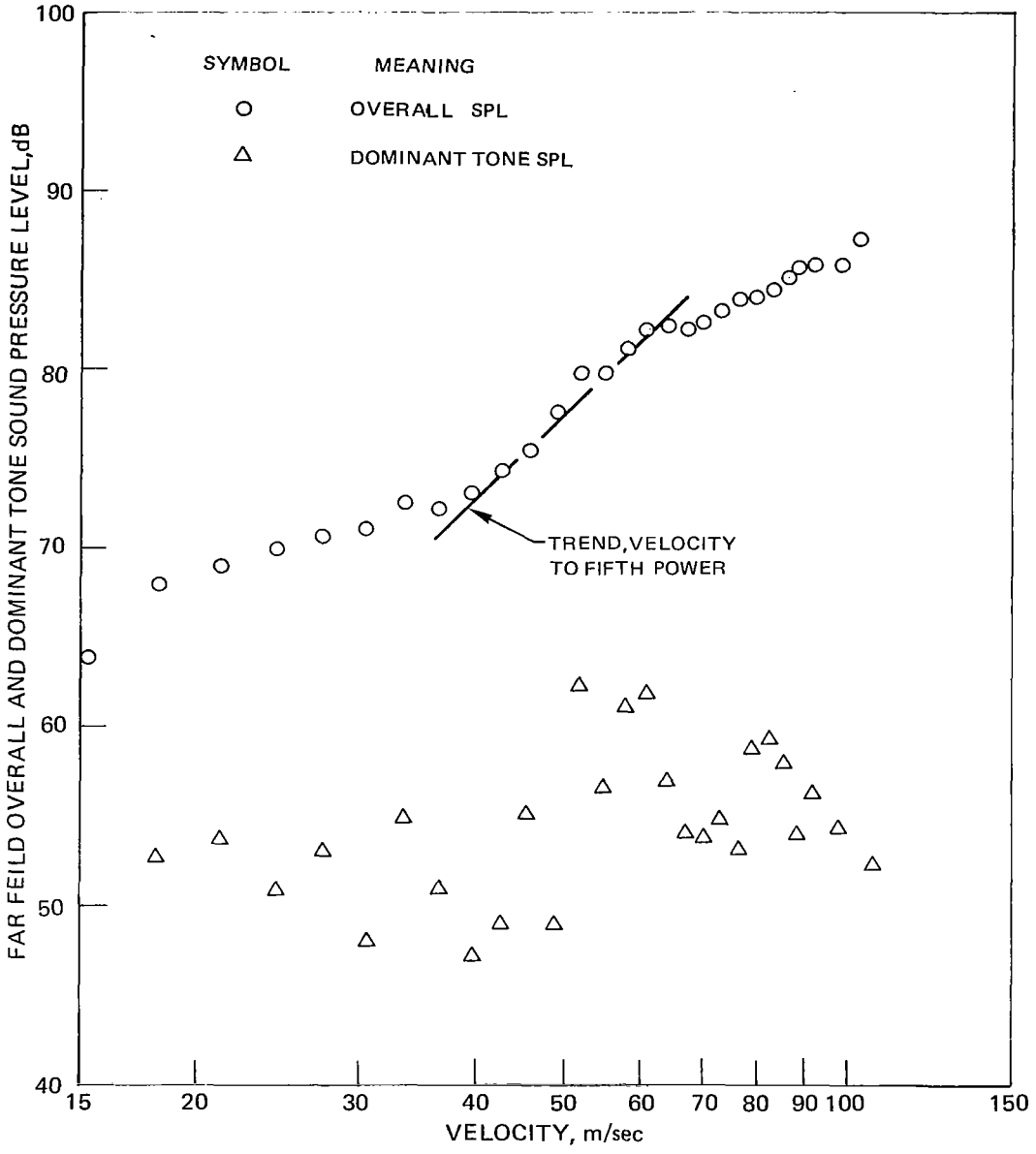

FIGURE 38 – VARIATION OF OVERALL SOUND PRESSURE LEVEL, AND DOMINANT TONE SOUND PRESSURE LEVEL, WITH VELOCITY FOR 4:1 TAPERED CHORD AIRFOIL, AT 0 ^{o} ANGLE OF ATTACK.

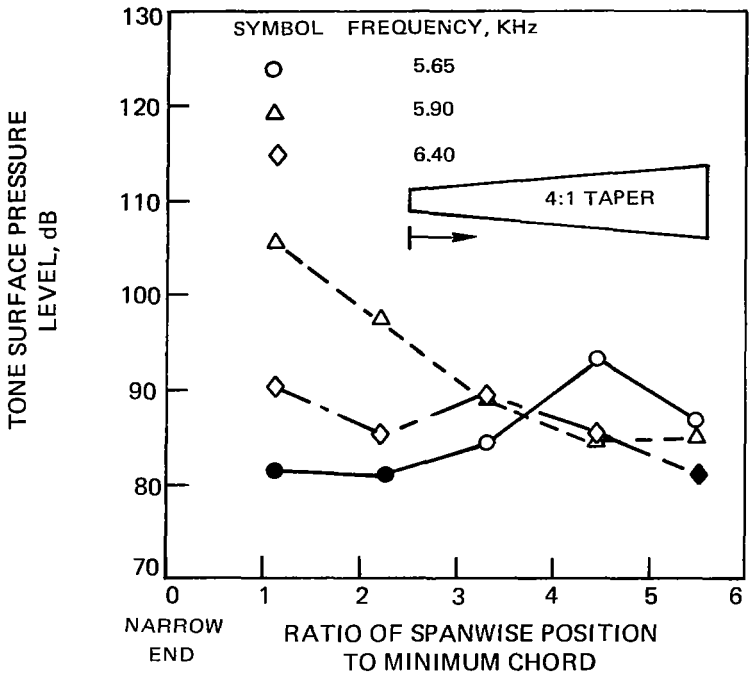

(a) VARIATION OF TONE SURFACE PRESSURE LEVELS WITH SPANWISE POSITION, SOLID SYMBOLS INDICATE BROADBAND LEVEL

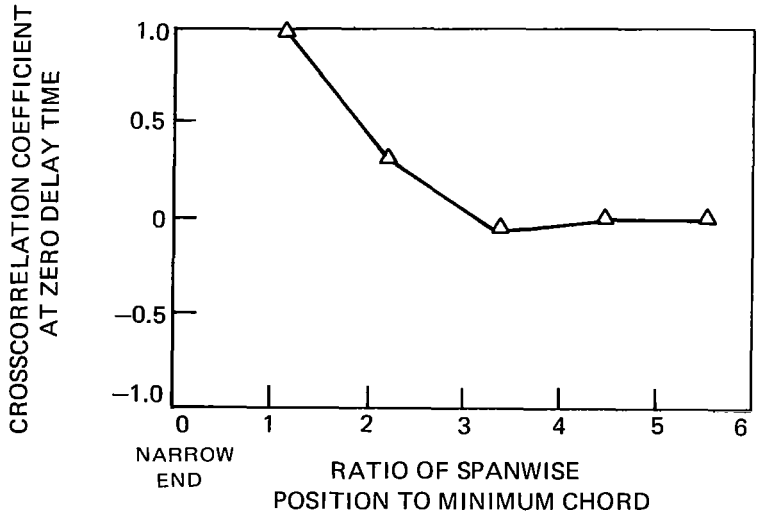

(b) VARIATION OF CROSSCORRELATION COEFFICIENT WITH SPANWISE POSITION

FIGURE 39 – TONE SURFACE PRESSURE LEVEL AND CROSSCORRELATION COEFFICIENT FOR 4:1 TAPERED CHORD AIRFOIL AT + 2° ANGLE OF ATTACK = 51.8 m/sec; VELOCITY = 51.8 m/sec.

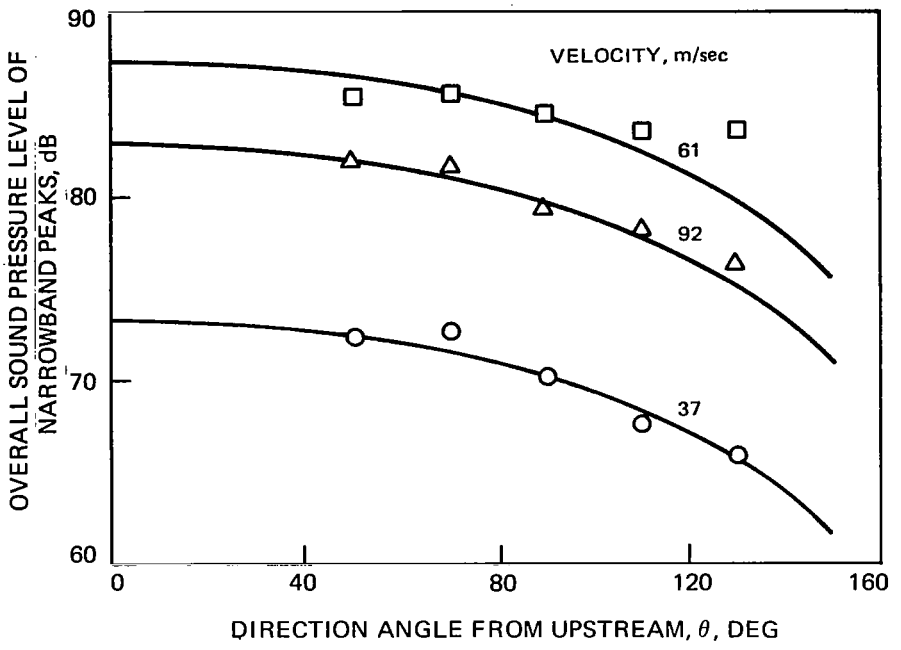

(a) CONSTANT CHORD AIRFOIL AT -4^{o} ANGLE OF ATTACK

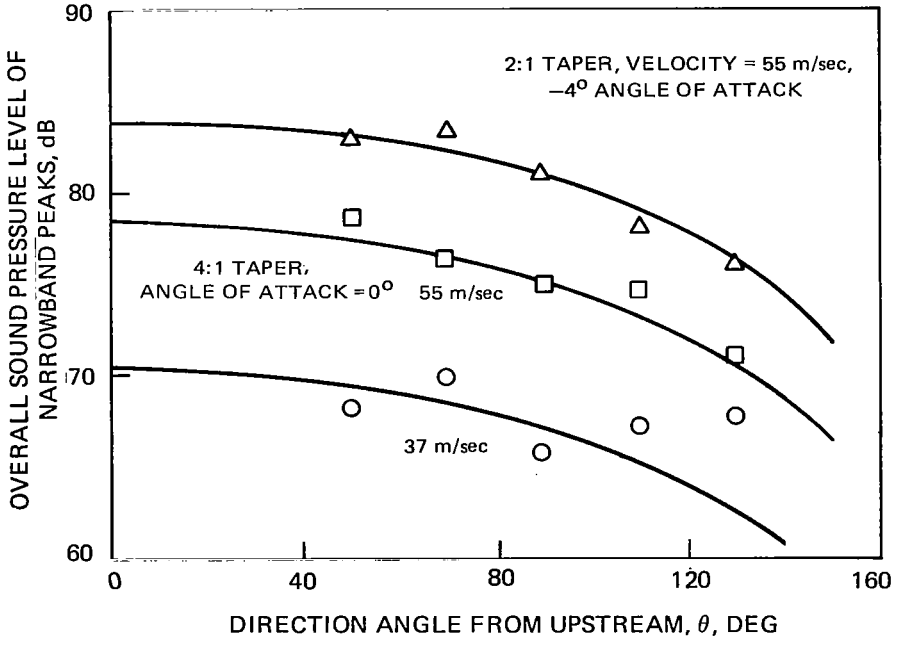

(b) 2:1 AND 4:1 TAPERED CHORD AIRFOILS

FIGURE 40 – FAR FIELD DIRECTIVITY OF OVERALL SOUND PRESSURE LEVEL OF NARROWBAND PEAKS PRODUCED BY AIRFOILS. CURVES SHOW DIRECTIVITY OF TRAILING EDGE NOISE, $\cos^2(\theta/2)$

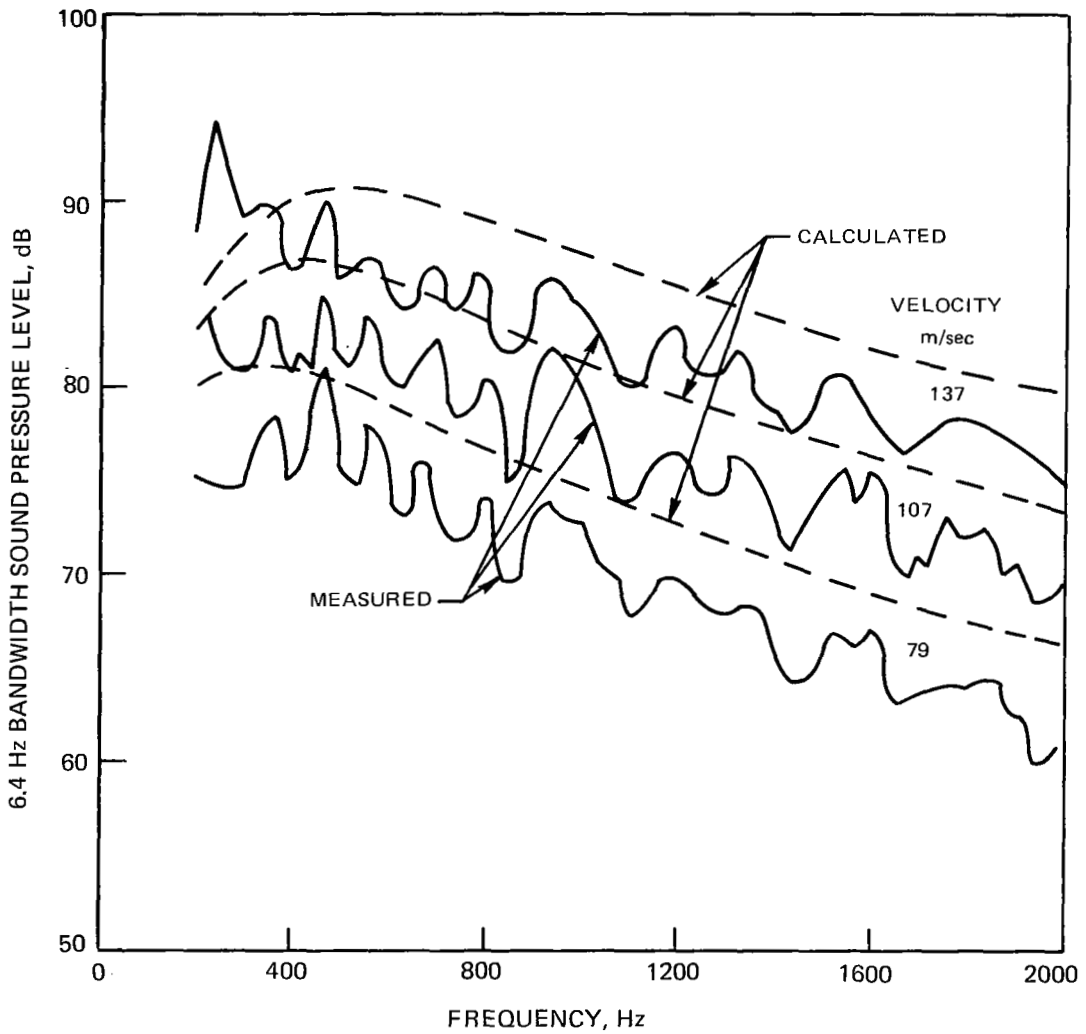

FIGURE 41 – COMPARISON OF MEASURED AND CALCULATED NARROWBAND SPECTRA DIRECTLY ABOVE CONSTANT CHORD AIRFOIL IN THE TURBULENT WAKE OF AN UPSTREAM AIRFOIL

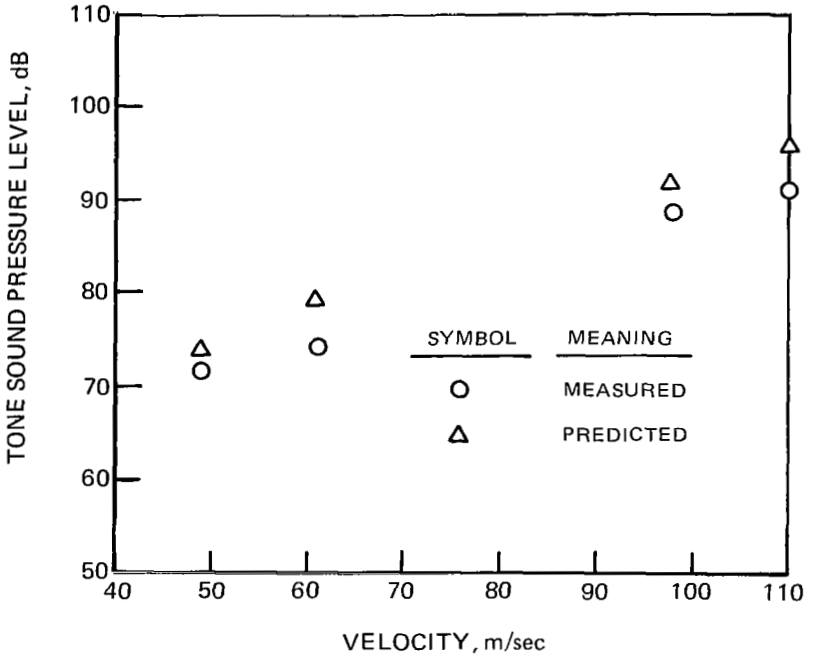

FIGURE 42 COMPARISON OF MEASURED AND PREDICTED FAR FIELD TONE SOUND PRESSURE LEVEL FOR THE 2:1 TAPERED CYLINDER, NO UPSTREAM TURBULENCE GENERATOR.

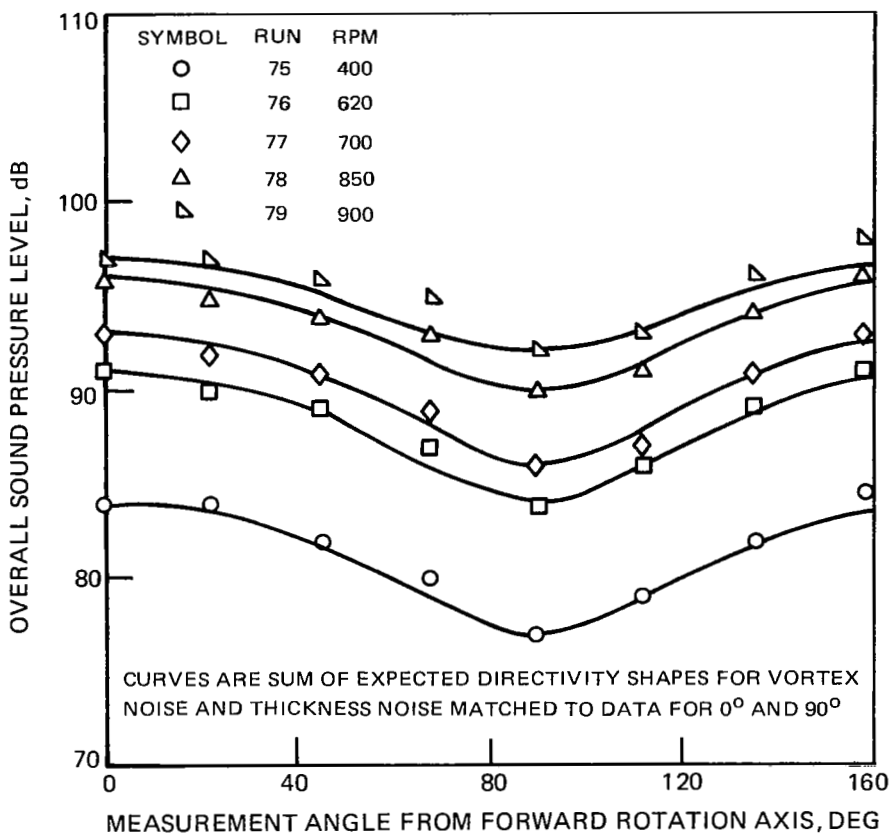

FIGURE 43 – DIRECTIVITY OF OVERALL SOUND PRESSURE LEVEL FOR CYLINDRICAL BLADES TESTED OUTDOORS

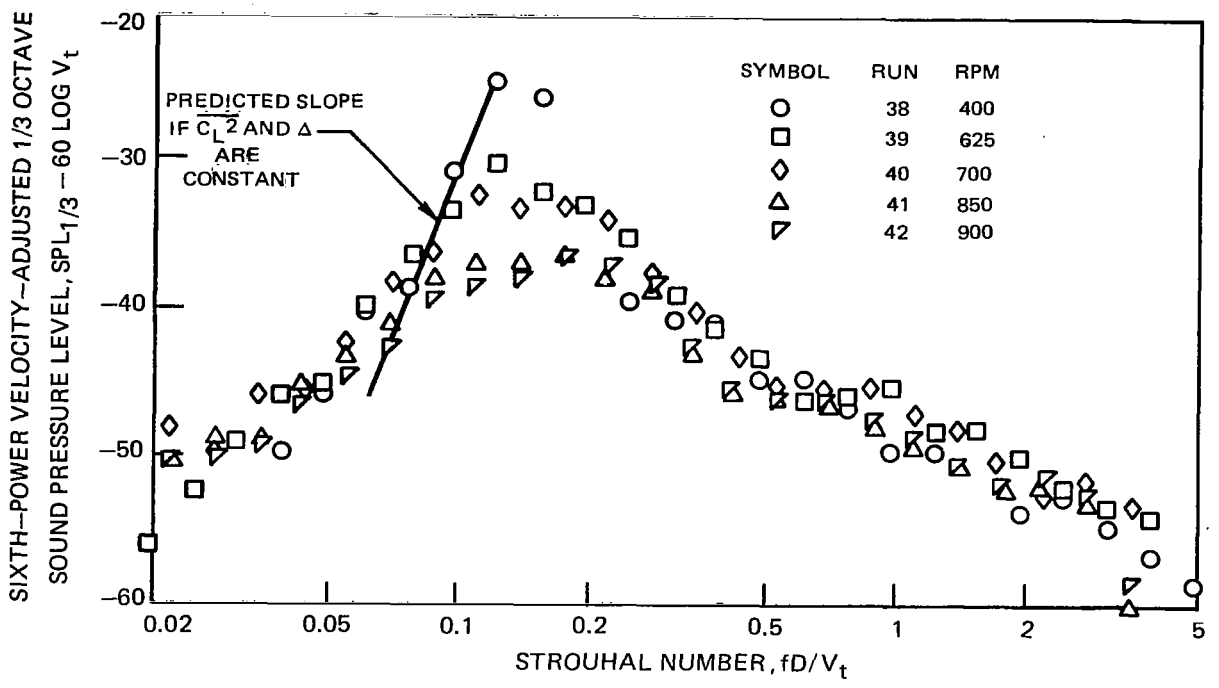

(a) SIXTH POWER VELOCITY ADJUSTMENT

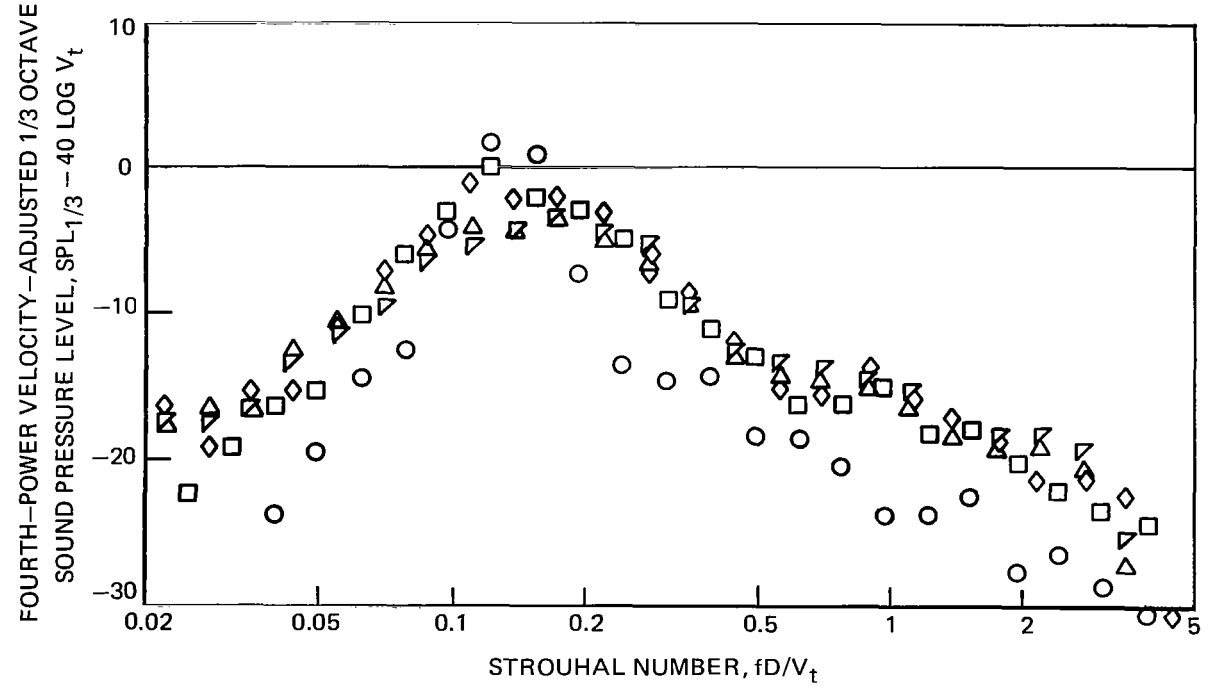

(b) FOURTH POWER VELOCITY ADJUSTMENT

FIGURE 44 – SCALING OF NOISE SPECTRA FOR ROTOR WITH CYLINDRICAL BLADES AT 6.1 m/sec AXIAL VELOCITY. MICROPHONE ON ROTATIONAL AXIS 2 ROTOR DIAMETERS UPSTREAM OF BLADES

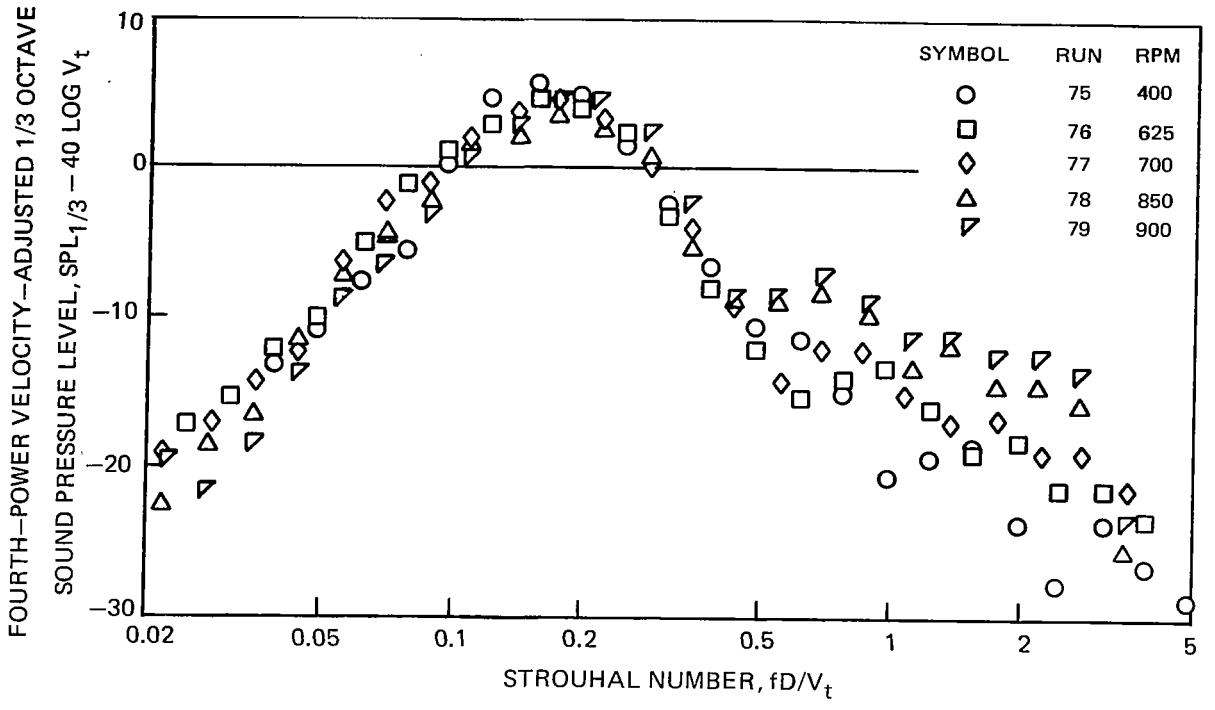

(a) OUTDOOR TESTS

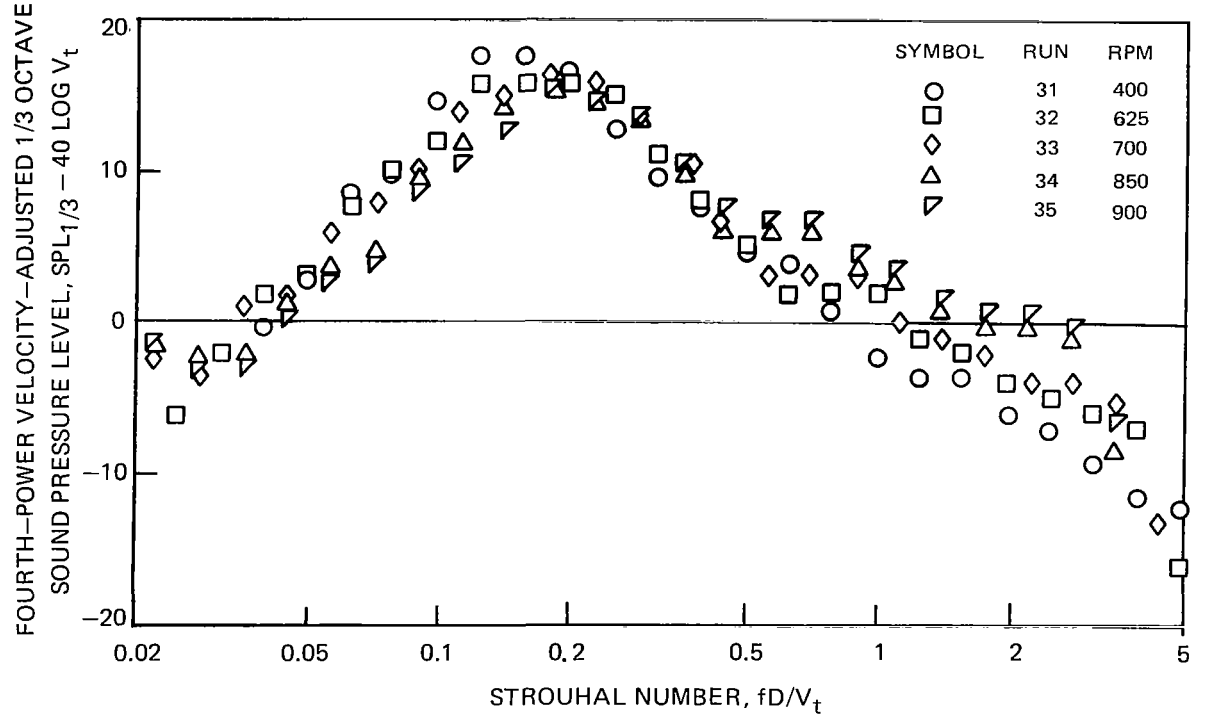

(b) WIND TUNNEL TESTS AT ZERO AXIAL VELOCITY

FIGURE 45 – SCALING OF NOISE SPECTRA WITH FOURTH POWER OF ROTATIONAL VELOCITY FOR ROTOR WITH CYLINDRICAL BLADES OPERATING WITHIN ITS SHED WAKE. MICROPHONE ON ROTATIONAL AXIS 2 ROTOR DIAMETERS UPSTREAM OF BLADES

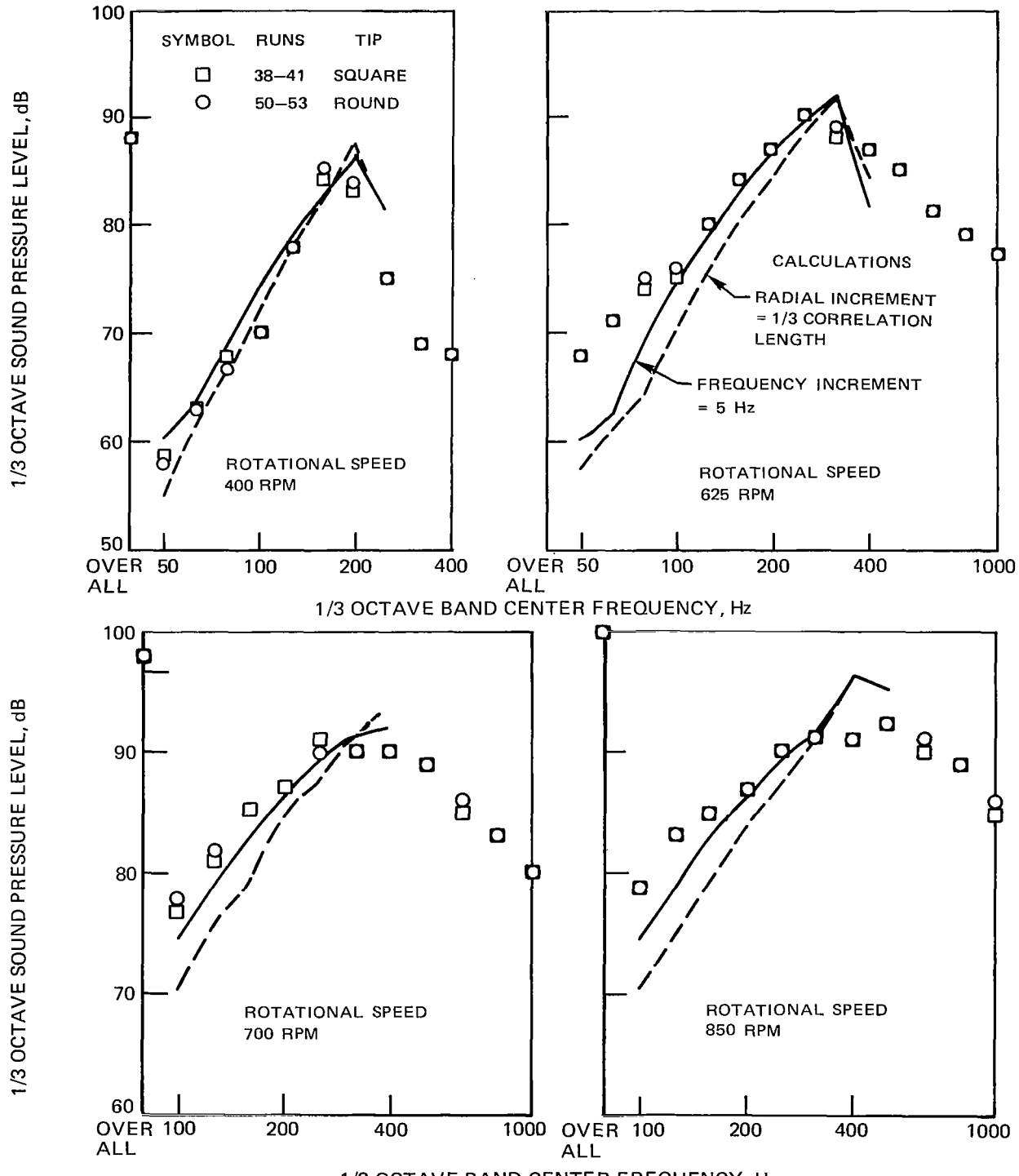

FIGURE 46 – COMPARISON OF MEASURED NOISE SPECTRA FOR ROTOR WITH CYLINDRICAL BLADES AND SHED WAKE BLOWN DOWNSTREAM, FOR TWO TIP SHAPES, WITH CALCULATIONS USING TWO DIFFERENT APPROXIMATIONS.

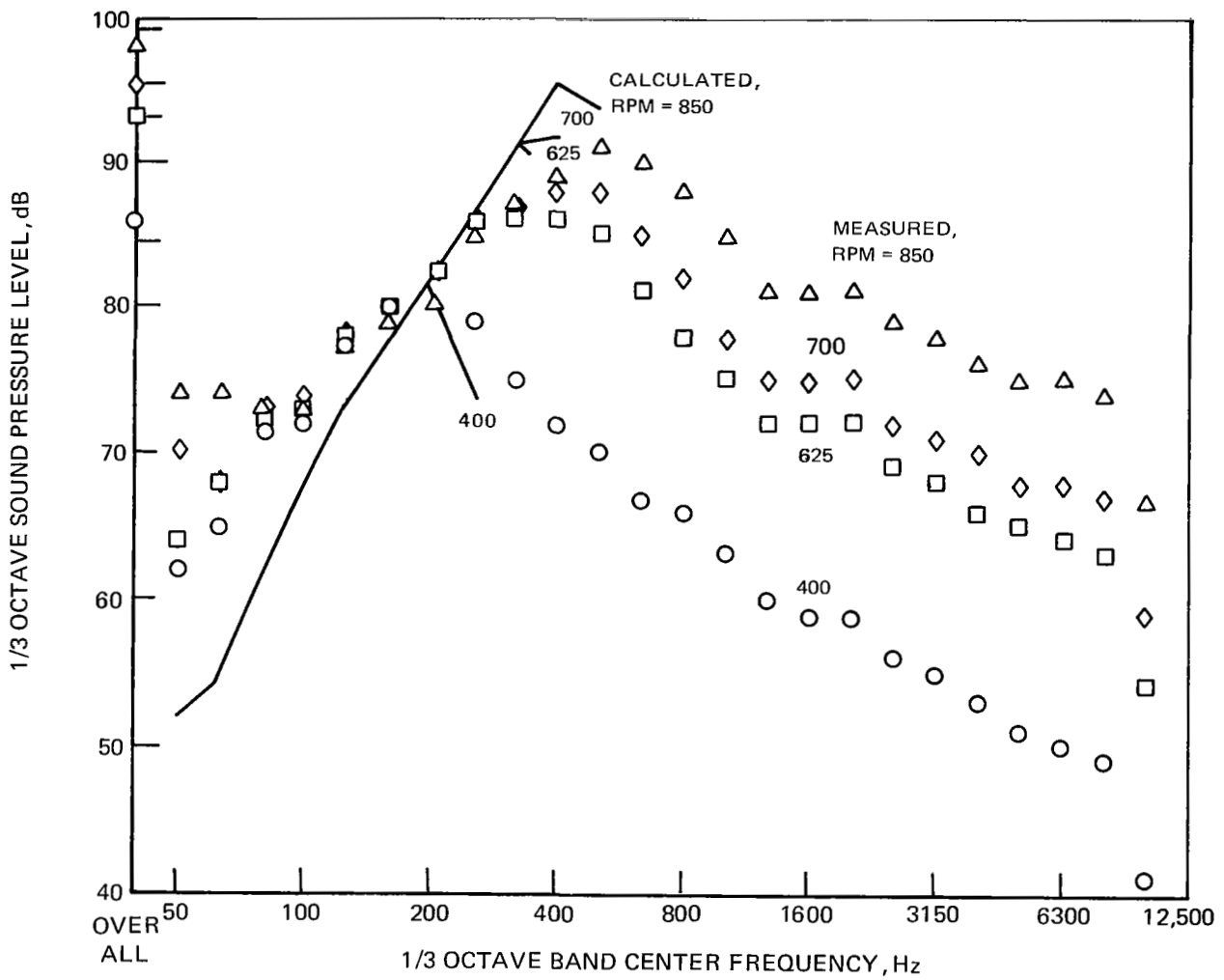

FIGURE 47 – COMPARISON OF CALCULATED AND MEASURED NOISE SPECTRA FOR ROTOR WITH CYLINDRICAL BLADES OPERATING WITHIN ITS SHED WAKE. MICROPHONE ON ROTATIONAL AXIS 2 ROTOR DIAMETERS UPSTREAM OF BLADES IN WIND TUNNEL.

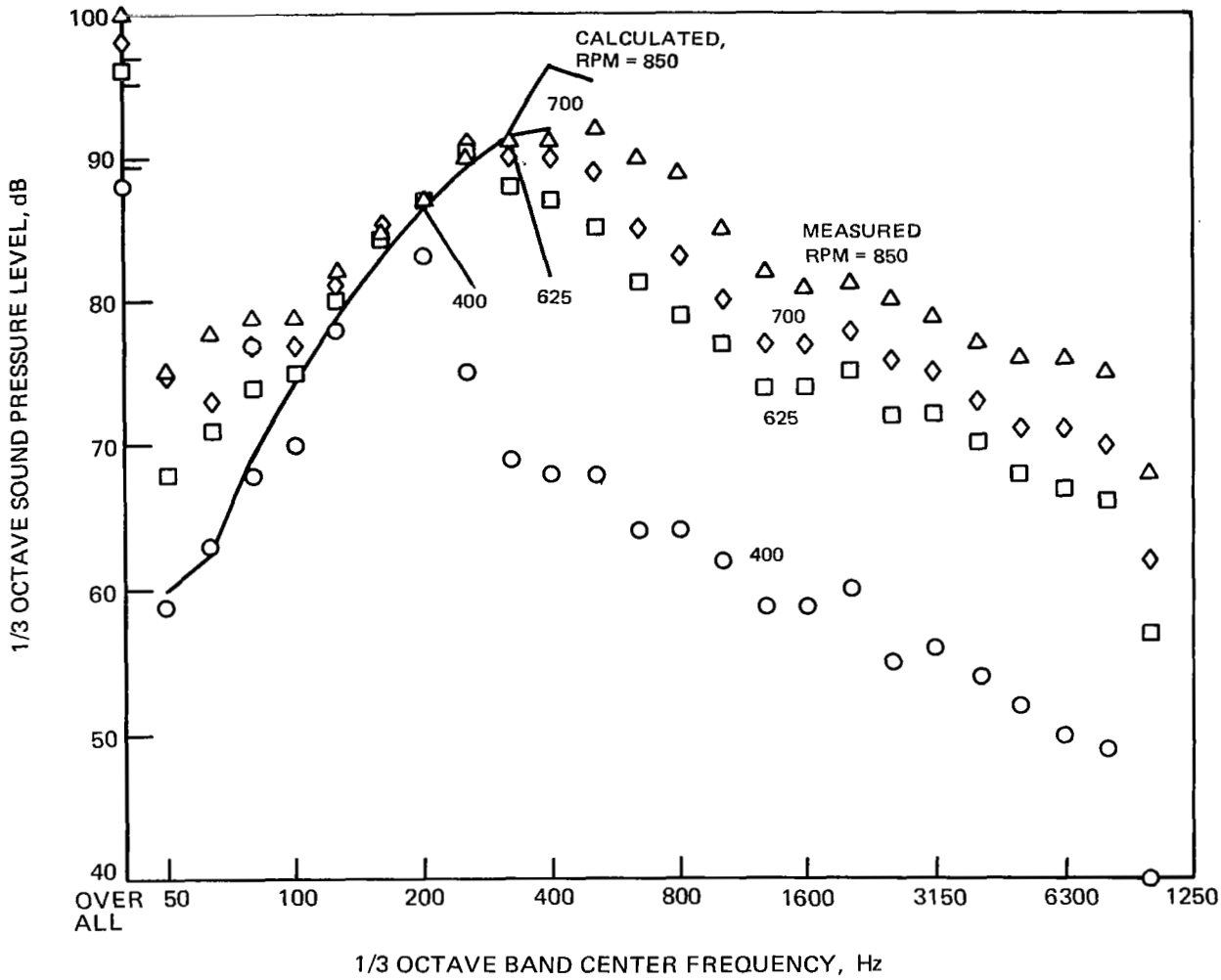

FIGURE 48 – COMPARISON OF CALCULATED AND MEASURED NOISE SPECTRA FOR ROTOR WITH CYLINDRICAL BLADES AND SHED WAKE BLOWN DOWNSTREAM. MICROPHONE ON ROTATIONAL AXIS 2 ROTOR DIAMETERS UPSTREAM OF BLADES.

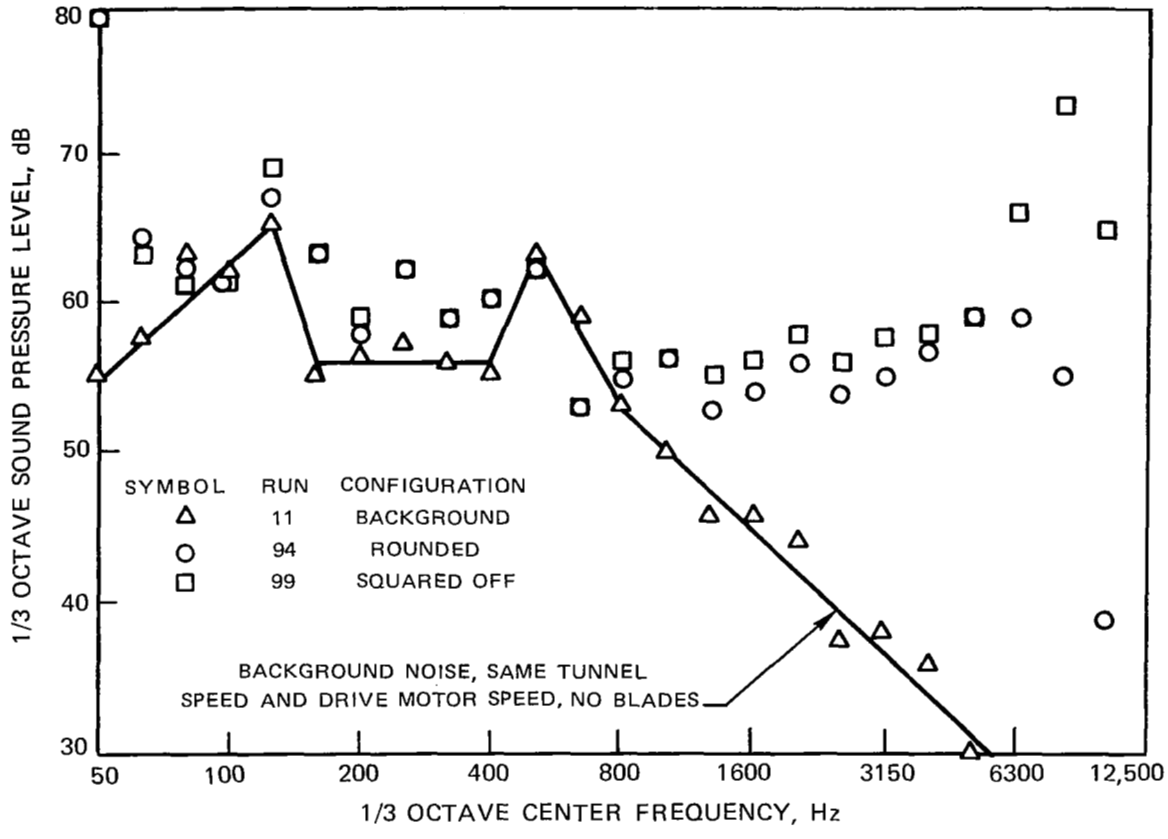

(a) 700 RPM ROTATIONAL SPEED

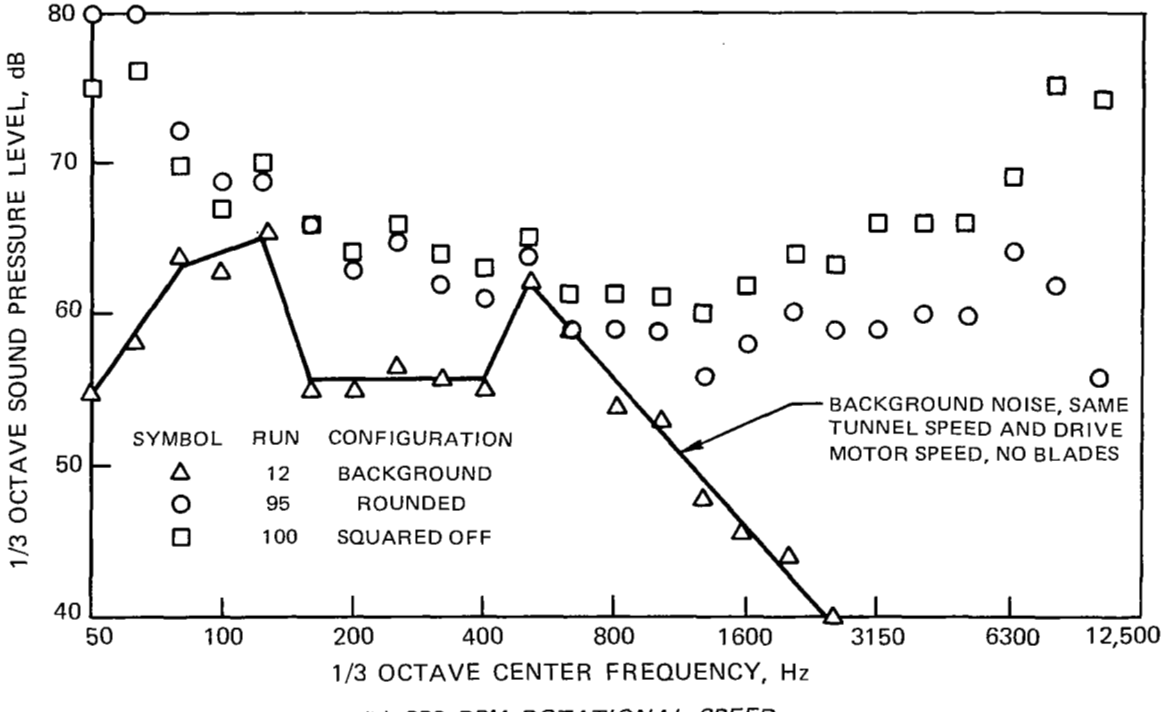

(b) 850 RPM ROTATIONAL SPEED

FIGURE 49- EFFECT OF BLADE TIP SHAPE ON SPECTRA MEASURED ON ROTATIONAL AXIS FOR ROTOR WITH HELICALLY TWISTED AIRFOIL BLADES AND SHED WAKES BLOWN DOWNSTREAM

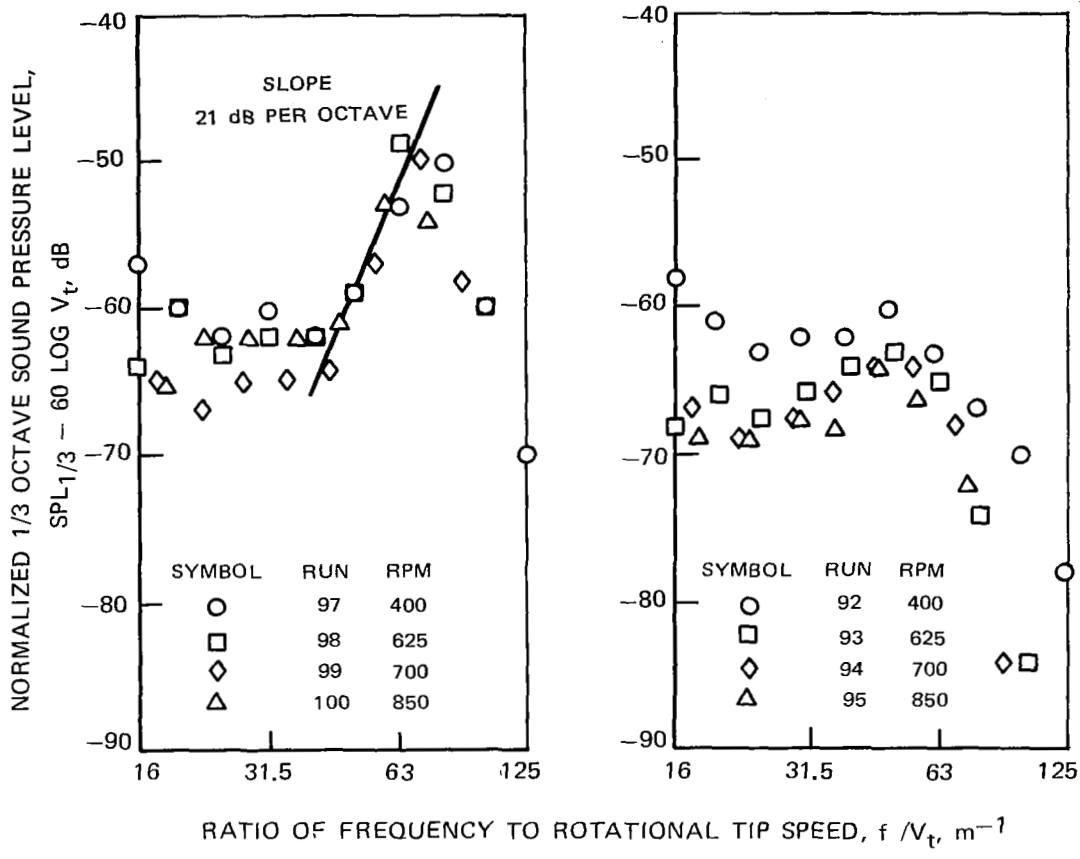

(a) SQUARED OFF BLADE TIP (b) ROUNDED BLADE TIP

ALL DATA FOR MICROPHONE 5

FIGURE 50 – NORMALIZED HIGH–FREQUENCY PEAK OF SPECTRA MEASURED ON ROTATIONAL AXIS FOR ROTOR WITH HELICALLY TWISTED AIRFOIL BLADES AND SHED WAKES BLOWN DOWNSTREAM

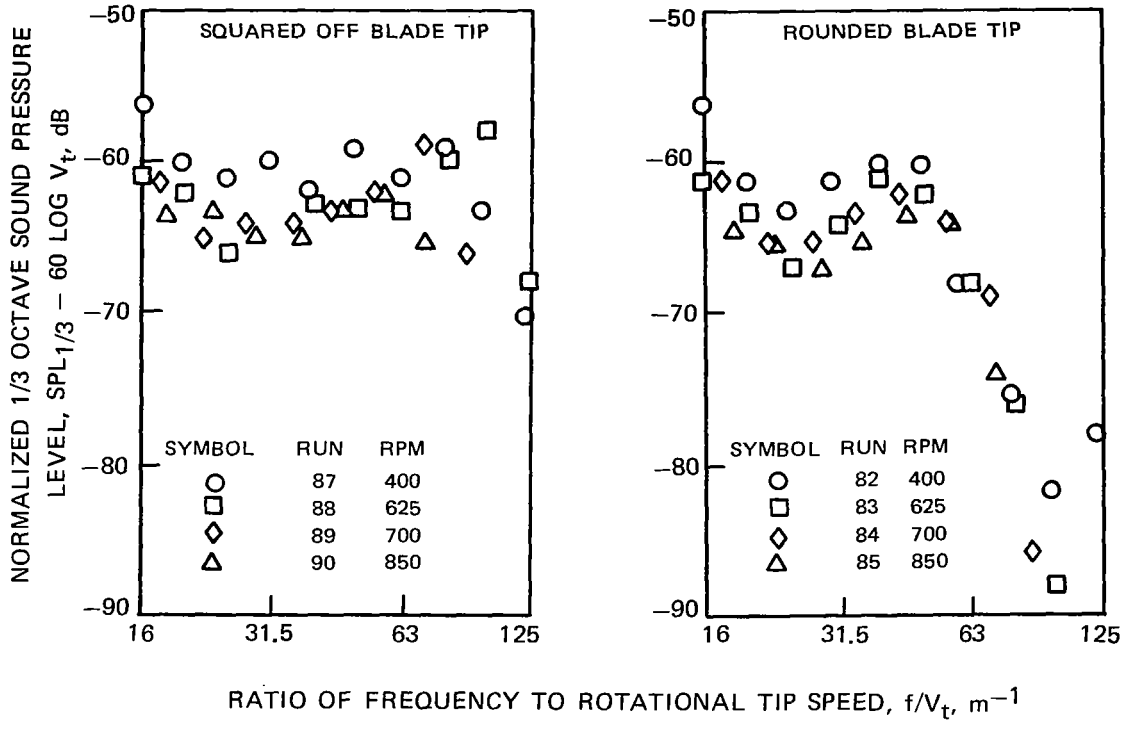

(a) WIND TUNNEL AT ZERO VELOCITY, MICROPHONE 5

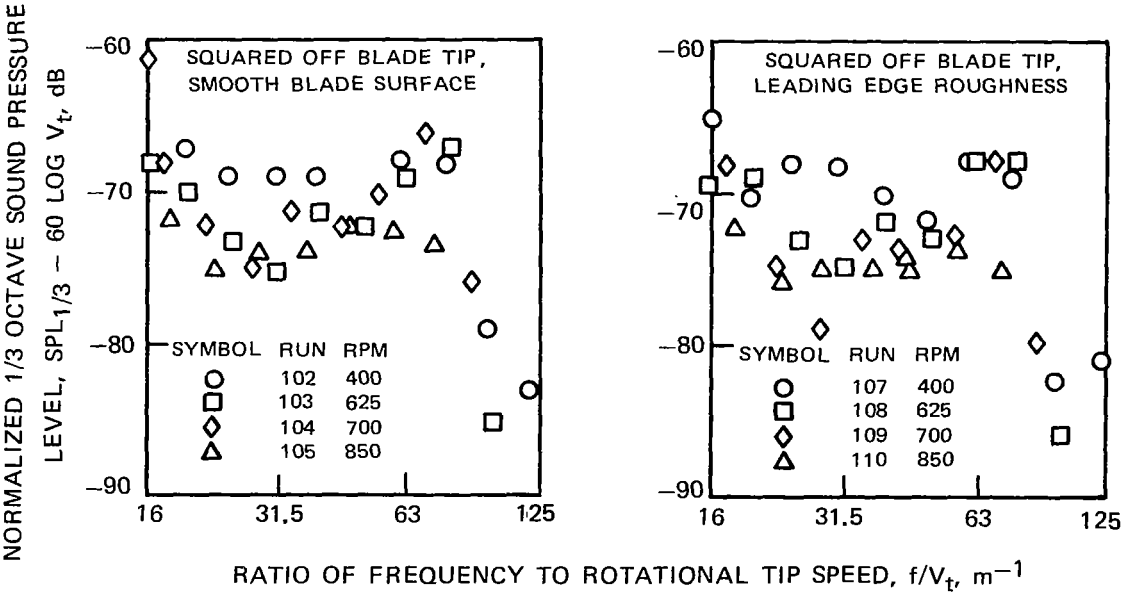

(b) OUTDOOR TEST STAND, MICROPHONE 10

FIGURE 51– NORMALIZED HIGH–FREQUENCY PEAK OF SPECTRA MEASURED ON ROTATIONAL AXIS FOR ROTOR WITH AIRFOIL BLADES AT ZERO AXIAL VELOCITY.

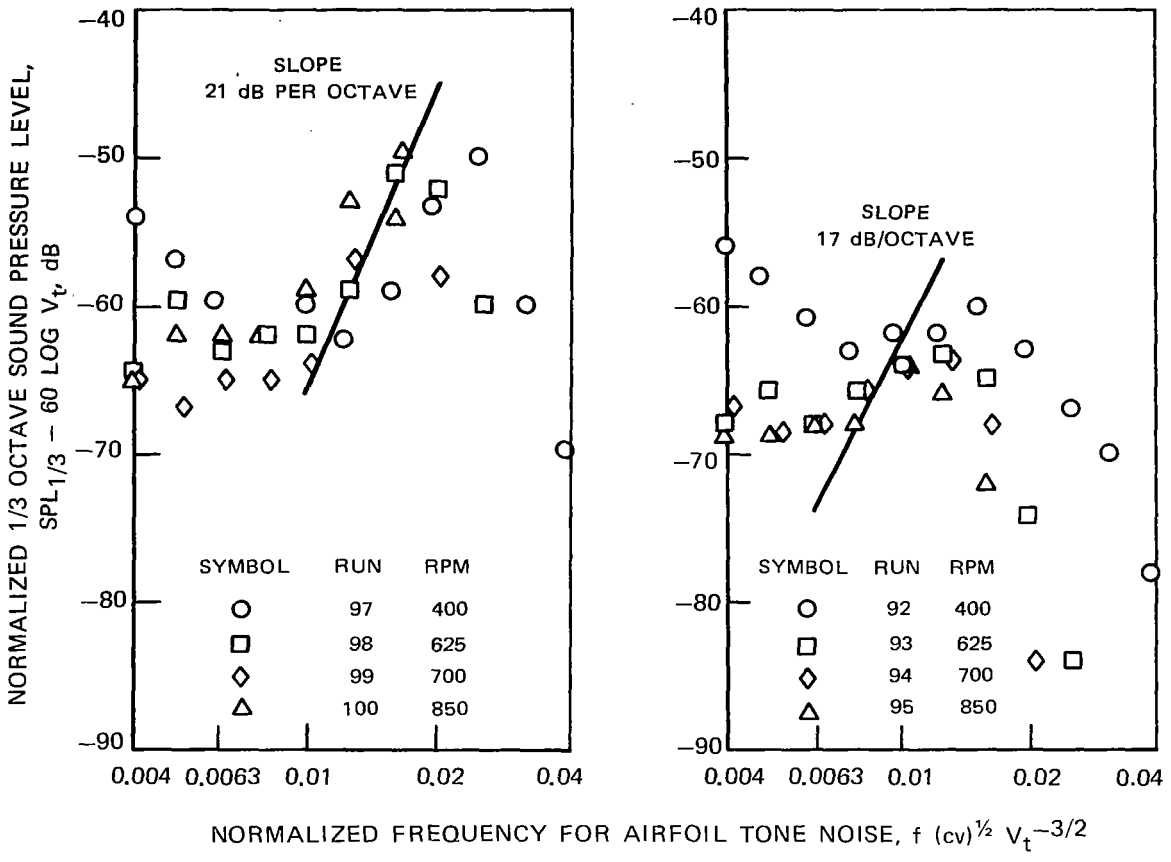

(a) SQUARED–OFF BLADE TIP

(b) ROUNDED BLADE TIP

FIGURE 52– HIGH–FREQUENCY PEAK OF SPECTRA MEASURED ON ROTATIONAL AXIS, NORMALIZED ACCORDING TO AIRFOIL TONE THEORY, FOR ROTOR WITH HELICALLY TWISTED BLADES AND SHED WAKES BLOWN DOWNSTREAM.

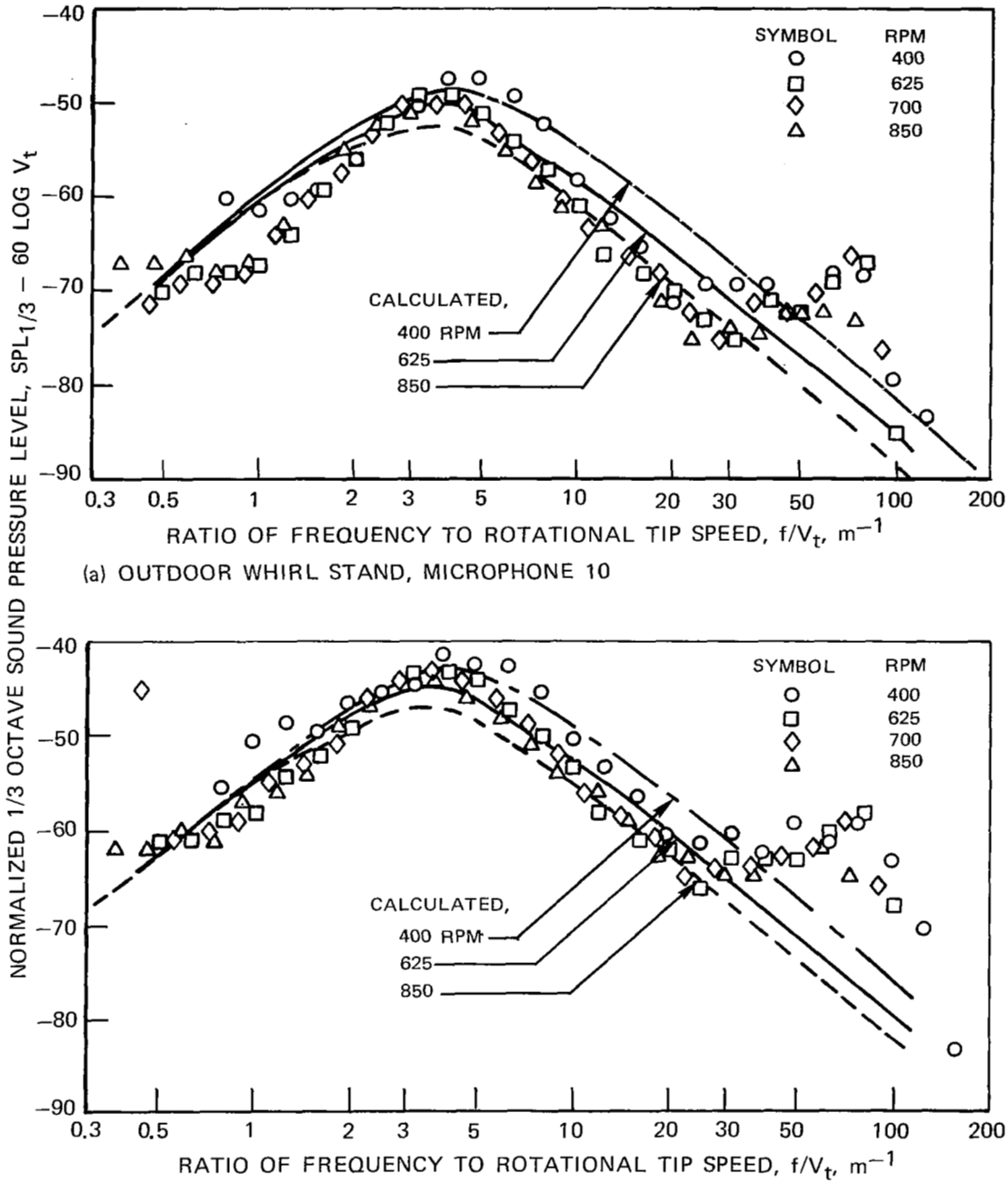

FIGURE 53 – COMPARISON OF CALCULATED AND MEASURED SCALED NOISE SPECTRA ON ROTATIONAL BLADES AT ZERO AXIAL VELOCITY

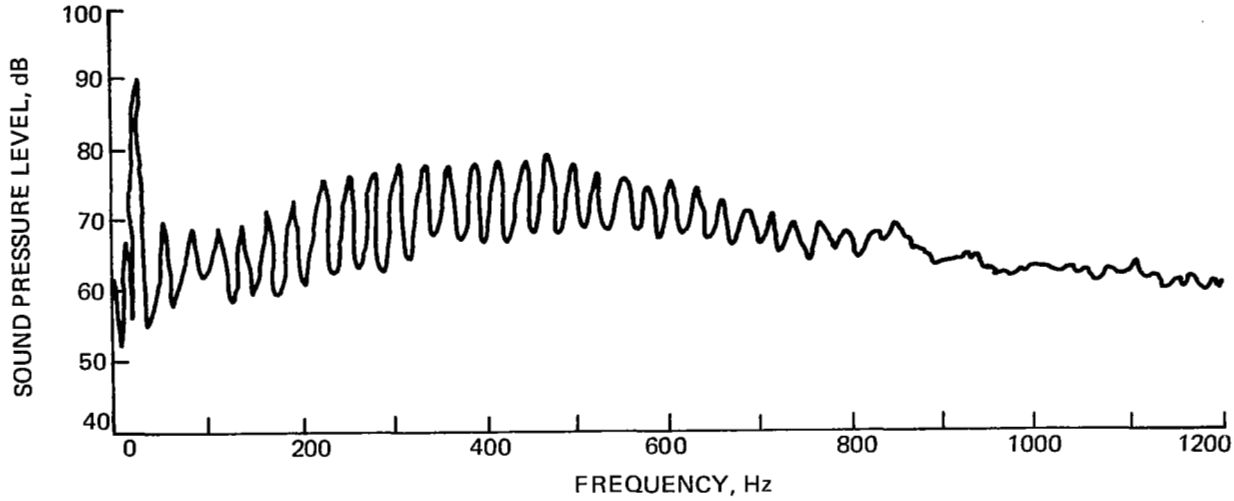

(a) SPECTRUM MEASURED AT 10 Hz BANDWIDTH

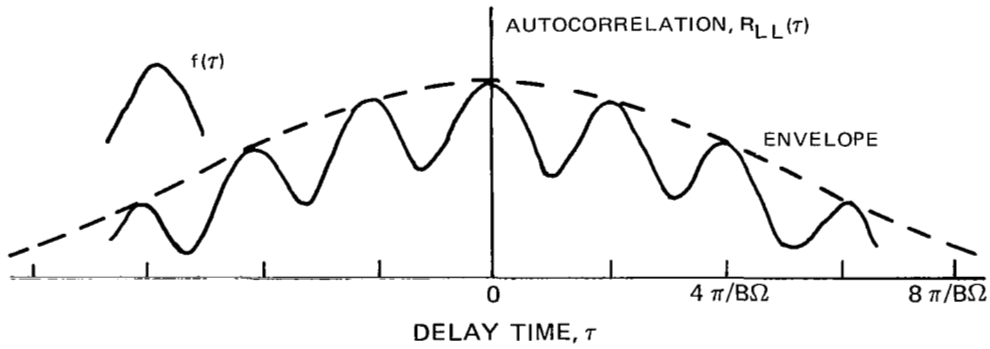

(b) ANALYTICAL MODEL OF AUTOCORRELATION FUNCTION

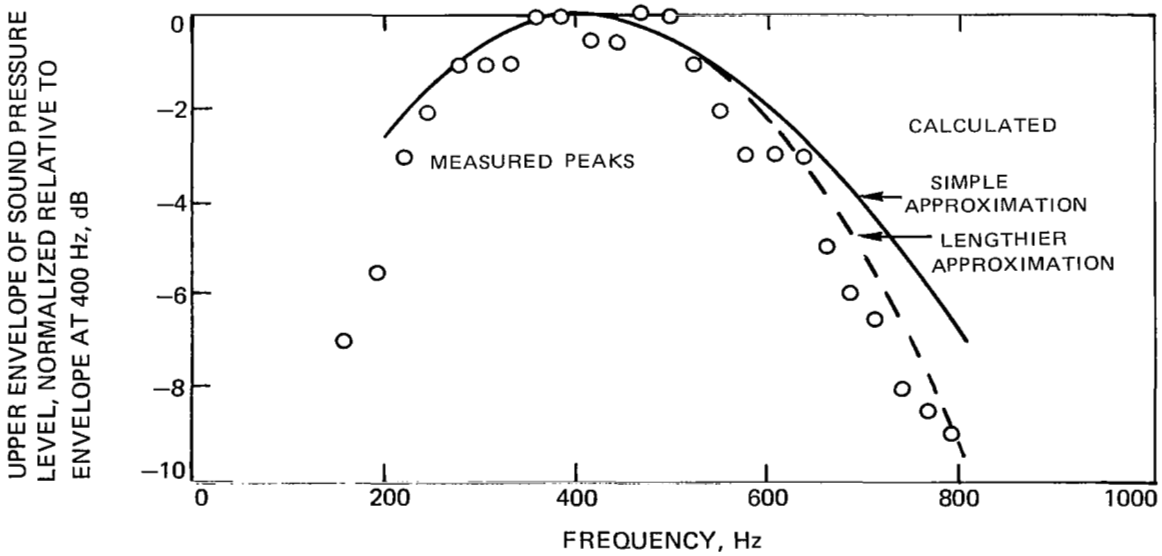

(c) COMPARISON OF CALCULATED AND MEASURED SPECTRUM ENVELOPES

FIGURE 54 – TONES PRODUCED BY AIRFOIL BLADES OPERATING WITHIN THEIR SHED WAKES. MICROPHONE ON ROTATIONAL AXIS 2 ROTOR DIAMETERS UPSTREAM OF BLADES IN WIND TUNNEL

NASA-Langley, 1976